Antireflection and Self-cleaning Structures for Solar Cells Using Laser Interference Nanolithography

Le Zhao

This is a digitised version of a dissertation submitted to the University of Bedfordshire.

It is available to view only.

This item is subject to copyright.

Antireflection and Self-cleaning Structures for Solar Cells Using Laser Interference Nanolithography

by

Le Zhao

Submitted to the Institute of Research in Applicable

Computing in partial fulfilment of the requirements for the

degree of

Doctor of Philosophy

at the

University of Bedfordshire

September 2015

Abstract

This research comprehensively reviews the properties of regular micro and nano structures fabricated by laser interference lithography and reports on their applications in the antireflection and self-cleaning surface. The research systematically investigates the laser interference lithography technology taking into account its advantages and abilities to realize various potential applications. Multiple-beam interference lithography systems are constructed. Laser interference interaction with silicon wafer is analysed and the optical and hydrophobic properties are obtained via measurements.

In order to fabricate the extremely low reflection and very large contact angle for solar cells, fabrication methods of antireflection and self-cleaning are surveyed and their advantages and disadvantages compared.

The research investigates the effect of heat transfer and the radiation of laser interference plasma on silicon wafer surfaces and proposes equations of heat flow and radiation effects of laser plasma of interfering patterns in a four-beam laser interference distribution. Following the irradiation, the silicon wafer surface is covered with a periodic array of micrometer and nanometer-sized structures, which have the shape of grating, cone and hole.

The research also investigates the effect of different laser parameters on the optical and hydrophobic properties of the structured silicon wafer surface. The results of periodic hexagonally-distributed hole structures fabricated by three-beam laser interference reveals excellent design guidelines for obtaining an extremely low solar-weighted reflection, (SWR, 1.86%) and

relatively large contact angle (140°) which can provide a strong self-cleaning capability on the solar cell surface.

In addition, the research creates a novel dual structure with antireflection and superhydrophobic properties fabricated by three-beam laser interference lithography. The fabrication method is three-beam laser interference combined with focused laser processing interacting on the silicon wafer surface. This kind of structure has a very low SWR (3.6 %) and extremely large contact angle which is more than 150° in the wavelength range from 380 nm to 780 nm.

The research shows that the laser interference lithography technology can be employed and further developed to fabricate micro and nano structures of strong antireflection and self-cleaning functions for applications in solar cells.

Acknowledgements

Without the support of family, friends, and co-workers, I would never have reached this point. Today, I want to thank everyone who has helped me along the way. I would first like to thank my supervisors, Professor Zuobin Wang and Professor Yong Yue. They are both outstanding advisors and have helped me overcome lots of difficult problems. Since joining the group, they taught me how to be a good researcher having kindness, self-confidence, good faith and responsibility. It will be invaluable in my professional life.

True appreciation is given to the International Research Centre for Nano Handling and Manufacturing of China (CNM) for providing me with an opportunity to carry out the experimental work. There are many members of CNM group that I wish to thank. Professor Zuobin Wang is wonderful supervisor and quick with any advice or help I needed when I joined the group. Mr Jinjin Zhang, Mr Liang Cao, Miss Miao Yu, Miss Wenjun Li and Dr. Li Li and all the members for helping me continue my study and show me the right way to do pretty much everything.

I really appreciate Professor Dayou Li and Professor Carsten Maple at IRAC for providing guideline of my research and everything to live in the UK.

Lastly, I would like to thank my family and friends, Mr Qiliang Wang, Ms He Xu, and Miss Qingling Meng for being so loving and supportive. My friends always helped me through hard times and helped me relax when needed. Without them, I would not have achieved my study goals.

Table of Contents

Abstract I

Acknowledgements III

Table of Contents IV

List of Figures VIII

List of Tables XV

Nomenclature XVI

Chapter 1 Introduction 1

1.1 Research Background 1

1.2 Aim and Objectives of the Research 4

1.3 Achievements 4

1.4 Implementation and Support 6

1.5 Structure of This Thesis 7

Chapter 2 Literature Survey on the Fabricated Antireflection and Self-cleaning Surfaces 9

2.1 Solar Cells 9

2.1.1 Background of Solar Cells 9

2.1.2 Working Principles of Solar Cells 10

2.2 Current Fabrication Methods of Antireflection 12

2.2.1 The Chemical Etching Method 12

2.2.2 The Antireflection Film Method 14

2.2.3 The Lithography Technologies Methods 15

2.3 Overview of the Fabrication Methods of Self-cleaning 20

2.3.1 Phase Separation and Self-assembly Method 20

2.3.2 Hydrothermal Method 21

2.3.3 Chemical Deposition and Electrodeposition Method 21

2.3.4 Lithography and Laser Etching Method 21

2.4 Micro and Nano Structures for Antireflection and Self-cleaning 22

2.5 Laser Interference Method to Produce Micro and Nano Scale Structures for Antireflection and Self-cleaning 22

2.6 Summary 25

Chapter 3 Methodologies for the Research 27

3.1 Laser Interference 27

3.1.1 Theory of Laser Interference 27

3.1.2 System Requirements of Laser Interference 29

3.1.3 Characteristics of Laser Interference 31

3.2 Theory of Antireflection 33

3.3 Theory of Self-cleaning 36

3.4 Summary 38

Chapter 4 Fabrication and Measurement 40

4.1 Fabrication Process by Laser Interference Lithography 40

4.2 Systems and Patterns of Multiple-Beam Laser Interference 46

4.2.1 Two-beam Laser Interference 46

4.2.2 Multiple-beam Laser Interference 50

4.2.2.1 Three-beam Laser Interference 50

4.2.2.2 Four-beam Laser Interference 53

4.3 Fabrication of Interference Patterns 55

4.4 Measurements System 58

Chapter 5 Laser Interference Interaction with Silicon Wafers *61*

5.1 Introduction 61

5.2 Theoretical Analysis 63

5.2.1 Laser Interaction with Silicon Wafers 63

5.3 Silicon Wafer Modification by Two-beam Laser Interference[55] 67

5.3.1 Experimental Details 68

5.3.2 Morphological Features with Different Fluences of Single and Multiple Laser Pulses [58] 69

5.3.3 Evolution of Grating Structures Formed by Laser Interference 72

5.4 Effect of Pulse Repetition Rate on Silicon Wafer Modification by Four-beam Laser Interference[59] 74

5.4.1 Experiment 75

5.4.2 Results and Discussions 77

5.5 Effects of Laser Fluences on Silicon Modification by Four-beam Laser Interference 81

5.5.1 Experiment 81

5.5.2 Results and Discussions 82

5.6 Summary 94

Chapter 6 One Step Fabrication of Triadic Hierarchical Silicon Architectures with Excellent Antireflection and Self-cleaning Properties 96

6.1 Introduction of Direct Laser Interference 98

6.2 Overview of Focused Laser Pulse Interaction with Silicon 100

6.3 Experimental Procedures 102

6.4 Results and Discussions 103

6.5 Optical and Hydrophobic Properties Measurements 108

6.5.1 Optical Measurements 110

6.5.2 Hydrophobic Properties Measurements 110

6.6 Summary 111

Chapter 7 Superhydrophobic Micro and Nano Dual Structures Fabricated by Direct Laser Interference Lithography 114

7.1 Experimental Procedures 114

7.2 Results and Discussions 115

Chapter 8 Antireflection Silicon Structures with Hydrophobic Property Fabricated by Three-beam Laser Interference 118

8.1. Introduction 118

8.2. Highlights 120

8.3. Experiment 120

8.4. Results and Discussions 121

8.5 Conclusions 126

Chapter 9 Conclusions and Recommender for Future Work 127

9.1 Conclusions 127

9.2 Future Work 128

References 131

Appendix A 137

Publications Originated from This Work 137

Appendix B 138

The Data of Figure 5.25 138

The Data of Figure 5.25 139

The Data of Figure 8.4 (b) 140

Appendix C **141**

Matlab Scripts **141**

List of Figures

Figure 1.1 (a) a solar cells array module and (b) solar cells array modules on the roof. 2

Figure 1.2 (a) a droplet takes up the particles loosely covering the leaf while rolling off and (b) a SEM image of the micro and nano structures of the lotus leaf...3

Figure 2.1 The physical phenomena of materials when solar energy is irradiating, (a) is the general object and (b) is the solar cell. 11

Figure 2.2 The principle of photovoltaic effect with more details [9]. 11

Figure 2.3 SEM images of chemically textured silicon surface [11]. 13

Figure 2.4 SEM images of silicon nanowires obtained after 45 min etching. (a) is top view and the inset shows the cross-sectional view of Si wires, and (b) is magnified tilted view with angle of tilt 12° [14]. 13

Figure 2.5 Fabrication procedure for creating hierarchical structures on the silicon surface, (a) is fabrication of pyramidal structures on silicon surface with KOH etching, (b) is electroless deposition of a thin discontinuous layer of Ag nanoparticles on the pyramidal structures in HF/AgNO3 solution and (c) is generation of hierarchical structures with Ag-assisted etching and then removal of Ag nanoparticles in nitric acid [15]. 14

Figure 2.6 Schematic diagram of a typical focused laser processing technology. 17

Figure 2.7 SEM image of the micro grating structures [40]. 22

Figure 2.8 SEM images of nanopillars fabricated from a polystyrene bead patterned silicon surface [20]. 22

Figure 2.9 SEM images of silicon nanoholes produced in p-Si (100) wafer, (a) is Top-view SEM image, (b) and (c) are top-view SEM images of ordered silicon nanoholes with large depths, and (d) is cross-sectional view of silicon nanoholes [45]. 23

Figure 2.10 SEM image of cross-sectional view of Si nanocones [46]. 24

Figure 2.11 Measured reflectance spectra of surfaces: (a) unstructured monocrystalline wafer, (b) wet etching specimen, (c) periodic black silicon fabricated by four-beam LIL in SF6. 24

Figure 2.12 Topographies of structures (a) Period of 6.7 μm; (b) Period of 14.2 μm; (c) Reflectance spectra of the two micro cone structures with exposures of 20s, 30s and 40s......24

Figure 2.13 Structural depths of samples as a function of the number of laser pulses. 25

Figure 3.1 Interference of two coherent laser beams[47]. 28

Figure 3.2 Schematic diagram of two-beam. 29

Figure 3.3 Schematic diagram of four-beam. 29

Figure 3.4 Scheme of a multi-beam laser interference lithography system [49]. 30

Figure 3.5 Schematic diagram of controllable period of two-beam laser interference from

micrometre to nanometre for grating structures, (a) the incident angle is 10°, (b) the incident angle is 40°, (c) the incident angle is 70° and (d) the incident angle is 85°................................32

Figure 3.6 Schematic diagram of controllable period of three-beam laser interference from micrometre to nanometre for dot structures, (a) the incident angle is 20°, (b) the incident angle is 40°, (c) the incident angle is 60° and (d) the incident angle is 80°................................32

Figure 3.7 Matlab simulation of various interference patterning. 33

Figure 3.8 The principles of the antireflection structures absorbing the sunlight. (a) is the planar surface and (b) textured surface [51]. 1 is the flux of incident photons, 2 and 3 are the flux of reflected photons and 4 and 5 are the flux of absorbed photons.................................34

Figure 3.9 Sketch of an antireflection film...35

Figure 3.10 A liquid drop showing the quantities in Young equation. 36

Figure 3.11 Models for the wetting behaviour of a water droplet on the solid surface; (a) is the Young model, (b) is the Wenzel model and (c) is the Cassie–Baxter model..............................37

Figure 4.1 State diagram of the fabrication process. 40

Figure 4.2 Flow diagram of the simulation code. Two screenshots of the interference simulation tool are displayed. The first one is the introduction of main parameters and the second is simulation pattern of corresponding intensity distribution. 42

Figure 4.3 Implementation of the optical design for energy control..43

Figure 4.4 Typical flow charts of indirect and direct processes. 44

Figure 4.5 Scanning Electron Microscopy (SEM) of the FEI Quanta™ 250 in our lab.................45

Figure 4.6 Atomic Force Microscope System of CSPM5500 in our lab. 45

Figure 4.7 Optical microscopy used in this research. 46

Figure 4.8 Schematic diagram of two-beam laser interference lithography.............................48

Figure 4.9 System of two-beam laser interference lithography. 48

Figure 4.10 Multi-beam interference simulations, (a) is 2D intensity distribution for two-beam interference and (b) is 3D intensity distribution for two-beam interference ($\lambda = 1064\,nm, \theta = 30°$). 49

Figure 4.11 The schematic diagram of tow-beam and double exposure laser interference process. 49

Figure 4.12 A simulation of the resulting pattern of the double exposure process..................49

Figure 4.13 The schematic diagram of three-beam laser interference lithography..................50

Figure 4.14 The system setup of three-beam laser interference lithography 51

Figure 4.15 (a) is 2D intensity distribution with hexagonal geometries for three-beam interference and (b) is 3D intensity distribution with hexagonal geometries for three-beam interference. 52

Figure 4.16 (a) is 2D intensity distribution with dual-periodic gratings for three-beam interference and (b) is 3D intensity distribution with dual-periodic gratings for three-beam interference. 53

Figure 4.17 Four-beam laser interference diagram. 54

Figure 4.18 System of four-beam laser interference lithography. 54

Figure 4.19 (a) is 2D intensity distribution for four-beam interference and (b) is 3D intensity distribution for four-beam interference ($\lambda = 1064\,nm, \theta = 30^{\circ}$). 55

Figure 4.20 The grating pattern generated by two-beam interference on the silicon wafer surface and its cross section 56

Figure 4.21 The hexagonal array pattern generated by three-beam interference on the silicon wafer surface and its cross section. 56

Figure 4.22 The square array pattern generated by four-beam interference on the silicon wafer surface and its cross section. 57

Figure 4.23 AFM images of tow-beam and double exposure laser interference pattern, (a) is 2D image and (b) is 3D image 57

Figure 4.24 SEM image of dual-periodic gratings fabricated by three-bean laser interference on silicon wafer surface. 58

Figure 4.25 Principle of antireflection measurement 59

Figure 4.26 Real system for reflection measurement. 59

Figure 4.27 System for contact angle (CA) measurement 60

Figure 5.1 Dynamics of laser interaction with materials [70]. 64

Figure 5.2 A SEM photograph of a hole drilled by femtosecond-pulse laser ablation. 66

Figure 5.3 Holes drilled by a nanosecond-pulse, (a) 80ps and (b) 3.3ns [66]. 67

Figure 5.4 Principle of two-beam laser interference lithography. 69

Figure 5.5 (a) AFM image of the result from a single laser pulse with the fluence of 786mJ/cm^2; (b) Cross-section analysis. 70

Figure 5.6 (a) AFM image of the result from a single laser pulse with the fluence of 821mJ/cm^2; (b) and (c) Cross-section analysis. 71

Figure 5.7 (a) AFM image of the result from a single laser pulse with the fluence of 1280mJ/cm^2; (b) Cross-section analysis (hole diameter: 16529nm; depth: >75nm). 72

Figure 5.8 AFM image of the result from 10 laser pulses with the fluence of 1280mJ/cm^2. 72

Figure 5.9 Optical microscopy images of the results from a single laser pulse with the fluence of 710mJ/cm^2; (a) Whole pattern spot, (b) Centre of the irradiated area, (c) and (d) Border regions of the irradiated area. 73

Figure 5.10 (a), (c) and (e) AFM images of the result from a single laser pulse with the fluence

of 710 mJ/cm^2; (b) Cross-section analysis (period: 8479nm; feature size: 1868nm; height: 82.30nm); (d) Cross-section analysis (period: 8144nm; feature size: 2012nm; height: 251nm); (f) Cross-section analysis (period: 8086nm; feature size: 1343nm; height: 374nm). 74

Figure 5.11 Principle of four-beam laser interference lithography. 76

Figure 5.12 The schematic diagram of four-beam laser interference system. 76

Figure 5.13 Optical images of damage centre of the irradiated area fabricated by four-beam laser interference technology; (a) The pulse repetition rate of 1 Hz and 10 laser pulses; (b) The pulse repetition rate of 5 Hz and 10 laser pulses and (c) The pulse repetition rate of 10 Hz and 10 laser pulses. 78

Figure 5.14 SEM images of damage centre of the irradiated area; (a)-(b) The pulse repetition rate of 1 Hz and 10 laser pulses; (c)-(d) The pulse repetition rate of 5 Hz and 10 laser pulses and (e)-(f) The pulse repetition rate of 10 Hz and 10 laser pulses; the scale bar of (a) is 20 µm, the scale bar of (a) is 20 µm, the scale bar of (a) is 20 µm, the scale bar of (a) is 20 µm, the scale bars of (e) and (e) are 10 µm, the scale bars of (b), (d) and (f) are 2 µm.......................... 80

Figure 5.15 A sectional plot of the four-beam laser interference intensity distribution. 85

Figure 5.16 SEM images of the flower-like silicon structures fabricated by four-beam laser interference lithography. (a) the single laser fluence of 354 mJ/cm^2, (b) the single laser fluence of 495 mJ/cm^2 and (c) the single laser fluence of 637 mJ/cm^2. 87

Figure 5.17 Diameter sizes of holes with error bars to the average size obtained from different laser fluences. 88

Figure 5.18 (a) SEM image (0°) and (b) SEM image (45°) of the pattern centres of the structures fabricated on the silicon wafer surface by four-beam laser interference lithography with 30 laser pulses. 89

Figure 5.19 (a) SEM image (0°) and (b) SEM image (45°) of the pattern centers of the structures fabricated on the silicon wafer surface by four-beam laser interference lithography with 100 laser pulses. 89

Figure 5.20 (a) SEM image (0°) and (b) SEM image (45°) of the pattern centres of the structures fabricated on the silicon wafer surface by four-beam laser interference lithography with 300 laser pulses. 89

Figure 5.21 (a) The computer simulation of intensity distribution of four-beam laser interference, the incident angle was 5.5°, the azimuthal angles were 0°, 90°, 180° and 270°, and the polarization angles were 0°, 90°, 0° and 90°, and (b) The schematic profile of a single positive peak dot intensity distribution after the effect of four-beam interference with the laser pulses of 30, 100 and 300. 91

Figure 5.22 (a) The computer simulation of intensity distribution of four-beam laser interference, the incident angle was 5.5°, the azimuthal angles were 0°, 90°, 180° and 270°, and the polarizers were 0°, 90°, 0° and 90°, and (b) The schematic profile of a single negative peak dot intensity distribution after the effect of four-beam interference with the laser pulses

of 30, 100 and 300. 91

Figure 5.23 Theoretical and experimental results for the comparison of their radius sizes with laser pulses. 92

Figure 5.24 SEM images of flower-like silicon structures fabricated by four-beam laser interference lithography with the single laser fluences of 354 mJ/cm^2, the pulse repetition rate of 10 Hz, the laser wavelength of 1064 nm and the pulse duration of 7-9 ns. (a) is the one single laser pulse, (b) is the laser pulses of 2, (c) is the laser pulses of 3, (d) is the laser pulses of 4, (e) is the laser pulses of 10, (f) is the laser pulses of 12, (g) is the laser pulses of 30, (h) is the laser pulses of 50 and (i) is the laser pulses of 200. 93

Figure 5.25 The reflectance of the four-beam laser interference patterned silicon surface (blue curve), the monocrystalline silicon solar cell surface (black curve) and polished silicon surface (red curve). 94

Figure 6.1. Scheme of fabrication process of hierarchical structures [79]. 97

Figure 6.2 Schematic of the integrated fabrications for the hierarchical pillar-like surfaces on the silicon substrates [80]. 98

Figure 6.3 The fabrication scheme of gecko foot-like arrays [80] 98

Figure 6.4 SEM image of damage in silicon generated with Ti: sapphire laser pulses in air [63]. 100

Figure 6.5 SEM images of typical surface morphologies for femtosecond-laser microstructured silicon at two magnifications. Both micrographs are taken at a 45° angle [82]. 101

Figure 6.6 shows SEM microphotographs of whisker-like columns formed on silicon irradiated at 1.7 J/cm^2 with 500 laser pulses. (a) is a 10° view, (b) is a 45° view and (c) is a magnified view of (b) [83]. 102

Figure 6.7 The computer simulation of three-beam laser interference. 103

Figure 6.8 (a) SEM images (0°) and (b) SEM image (45°) of the pattern centres of the structures fabricated on the silicon wafer surface by three-beam laser interference lithography with 30 laser pulses. 104

Figure 6.9 (a) SEM images (0°) and (b) SEM image (45°) of the pattern centres of the structures fabricated on the silicon wafer surface by three-beam laser interference lithography with 50 laser pulses. 104

Figure 6.10 (a) SEM images (0°) and (b) SEM image (45°) of the pattern centres of the structures fabricated on the silicon wafer surface by three-beam laser interference lithography with 200 laser pulses. 105

Figure 6.11 (a) SEM images (0°) and (b) SEM image (45°) of the pattern centres of the structures fabricated on the silicon wafer surface by three-beam laser interference lithography with300 laser pulses. 105

Figure 6.12 (a) SEM images (0°) and (b) SEM image (45°) of the pattern centres of the

structures fabricated on the silicon wafer surface by three-beam laser interference lithography with 600 laser pulses. 105

Figure 6.13 SEM image of some randomly nano dot structures evenly distributed on the conical structures with hexagonally-distributed holes using three-beam laser interference with 300 pulses. 106

Figure 6.14 Cross Section of SEM image of some randomly nano dot structures evenly distributed on the conical structures with hexagonally-distributed holes using three-beam laser interference with 600 pulses. 106

Figure 6.15 Cross Section of SEM image of some randomly nano dot structures evenly distributed on the conical structures with hexagonally-distributed holes using three-beam laser interference, (a) is 30 pulses, (b) is 30 pulses, (c) is 50 pulses, (d) is 200 pulses, (e) is 300 pulses, (d) is 600 pulses. 108

Figure 6.16 The reflectance of the samples irradiated by three-beam laser interference with laser pulses of 30, 50, 200, 300 and 600 in the visible spectrum range from 380 to 780. 110

Figure 6.17 The numbers of laser pulses as a function of calculated SWRs. 112

Figure 6.18 The numbers of laser pulses as a function of calculated SWRs. 112

Figure 6.19(a) Video screenshots of hydrophobic measurement process from (a) to (d). 113

Figuer 7.1 2D and 3D plots of four-beam laser interference simulation results. 115

Figure 7.2. (a) SEM image (low magnification) of the micro and nano dual structures fabricated by four-beam laser interference. (b) Close-up image of micro pine trees at high magnification. 116

Figure 7.3 SEM microstructures and contact angle measurement of the silicon samples: (a) T_e =20s, CA=125.8°; (b) T_e =30s, CA=145°; (c) T_e =60s, CA=153.2°. 117

Figure 8.1 Simulation of intensity distributions of multi-beam interference with incidence angles of 5.5°, (a) three-beam laser interference and (b) four-beam laser interference......... 121

Figure 8.2 (a)-(d) are SEM images of silicon structures fabricated by three-beam laser interference with a laser influence of 637 mJcm^{-2}. (a) laser exposures of 30, (b) laser exposures of 100, (c) laser exposures of 300, and (d) laser exposures of 600. (e)-(h) are SEM images of silicon structures fabricated by four-beam laser interference with a laser influence of 637 mJcm^{-2}. (a) laser exposures of 30, (b) laser exposures of 100, (c) laser exposures of 300, and (d) laser exposures of 600. 123

Figure 8.3 Reflectance measurements of structures fabricated by three-beam (black curves) and four-beam (red curves) laser interference with the same laser influence of 637 mJcm^{-2} and the laser exposures of 10 (a), 30 (b), 100 (c), 300 (d) and 600 (e). 123

Figure 8.4 The morphology (a) and reflectance (b) of regular hexagonally-distributed patterns fabricated by three-beam laser interference with different laser exposures of 30, 50, 300 and

600. 124

Figure 8.5 (a) is the cross section SEM images of different laser pulses and the scale bar is 10 µm. (b) is the laser pulses and the estimated average heights of the hexagonally-distributed silicon patterns as a function of calculated SWRs. 125

Figure 8.6 The contact angles of hexagonally-distributed silicon patterns as a function of the number of pulses. (a)-(e) are water droplets with a contact angle for hexagonally-distributed patterns fabricated by three-beam laser interference with the laser pulses of 30, 50, 100, 300 and 600, respectively... 126

List of Tables

Table 2.1 Advantages and Disadvantages of the Fabrication Methods of Antireflection..........18

Table 4.1 Specifications of the laser source selected for the fabrication process......................42

Table 4.2 Matlab simulation of beam configuration parameters of grating structure. 49

Table 4.3 Matlab simulation of beam configuration parameters of hexagonal patterning by three-beam laser interference....52

Table 4.4 Matlab simulation of beam configuration parameters of dual-periodic gratings by three-beam laser interference....52

Table 4.5 Matlab simulation of beam configuration parameters of square dots patterning by four-beam laser interference....54

Table 4.6 Beam configuration parameters of grating structure. 55

Table 4.7 Beam configuration parameters of grating structure. 56

Table 4.8 Beam configuration parameters of square array pattern....57

Table 4.9 Main specifications of spectrometer and electrochemical workstation. 60

Table 5.1 Beam configuration parameters for the selected interference pattern.....................69

Table 5.2 Beam configuration parameters for the selected interference patten 77

Table 5.3 Beam configuration parameters for the selected interference pattern.....................82

Table 6.1 Beam configuration parameters for the selected interference pattern...................103

Table 7.1 Beam configuration parameters for the selected interference pattern................... 115

Table 7.2 Different fluences versus the contact angles on the result substrate. 116

Nomenclature

Ai	Amplitude
λ	Wavelength
θ	Beam incident angle
$\vec{P}_i$	Polarization vector
$\vec{n}_i$	Propagation vector
$\vec{r}_i$	Position vector
ϕ_i	Phase constant
I_0	Intensity of the two beams
ω	Frequency
λ_0	Vacuum wavelength
P	Grating period
n_{air}	Air refractive index
n	Substrate material refractive index
θ_i	Polar angle of incidence light
ϕ	Azimuthal angle of incidence light
$P_{\max}$	Maximum period
$n_{AR\text{-}film}$	Refractive index of the media of the antireflection coating
n_{eff}	Effective refractive index
W_n	Width of structures
$\gamma_{S/V}$	Interfacial tension between the solid and air
$\gamma_{S/L}$	Interfacial tension between the solid and liquid
$\gamma_{L/V}$	Interfacial tension between the liquid and air

R_f	Roughness factor
ψ_L	Solid surface area fractions of the solid and air
ψ_A	Air surface area fractions of the solid and air
T_e	Temperature of the electron gas
T_i	Temperature of the lattice
C_e	Heat capacity
C_i	Heat capacity
K	Thermal conductivity
γ	Coupling constant
τ_L	Laser pulse duration
α	Material absorption coefficient
σ	Coefficient of surface tension
τ_l	Life time of the molten state
ρ	Density of the molten silicon
f_0	Laser fluence
C_v	Specific heat capacity
L_m	Specific heat of melting
T_m	Melting temperature
D	Thermal diffusivity
$t_{(\alpha)}$	Temperature of the substrate
τ_s	Pulse duration
SWR	Solar-weighted reflectance
N_{photon}	Photon number

Declaration

I declare that this thesis is my own unaided work. It is being submitted for the degree of Doctor of Philosophy at the University of Bedfordshire.

It has not been submitted before for any degree or examination in any other university.

Name of candidate: Le Zhao signature:

Date: 24 September 2015

Chapter 1
Introduction

1.1 Research Background

As a sustainable and environmentally friendly energy source, solar energy is a potential solution to solve the global warming and fossil fuel exhaust problems, and solar energy is an alternative renewable clean energy source in high demand for the coming decades [1]. Among various clean energy sources, such as hydroelectricity, biomass, wind and geothermal energy, solar energy is the most abundant natural energy resource in the world. While the energy from sunlight irradiated the earth in one hour can make our annual global energy consumption, usable solar energy is very little. Solar cells can directly generate the electric power from sunlight and alone hold great promise to provide enough renewable clean energy and accommodate the ever-increasing energy demands of mankind [1]. Figure 1.1 shows a solar cells array module and solar cells array modules on the roof in order to provide electricity to the house.

As a result of this demand, solar cells still suffer from low efficiency and high cost [2]. Silicon is the dominative material of commercial solar cells. However, the efficiency of silicon solar cells has almost saturated at 25.6% in monocrystalline silicon solar cells and 19.8% in multi-crystal silicon solar cells [3]. Recently, the efficiency of GaAs solar cells is higher than silicon and GaAs solar cells also have been as a potential alternative for Si solar cells. The highest efficiency of GaAs-based solar cells has been reported as 37.9% [3]. Therefore, it is valuable to achieve high efficient solar cells. Minimization of reflection of surface is considered as one of the most important factors for enhancing the efficiency of solar cells [4, 5]. Due to the large refractive index discontinuity at air-silicon interfaces, strong reflection above 30% causes the additional loss of light energy. To resolve this problem, one kind of antireflection layer is widely used in a variety of optical lenses, flat panel displays and solar cells [6]. It is a common method of trapping sunlight and reducing optical reflection at the surface of solar cells to improve

the conversion efficiency. It has become indispensable for solar cells.

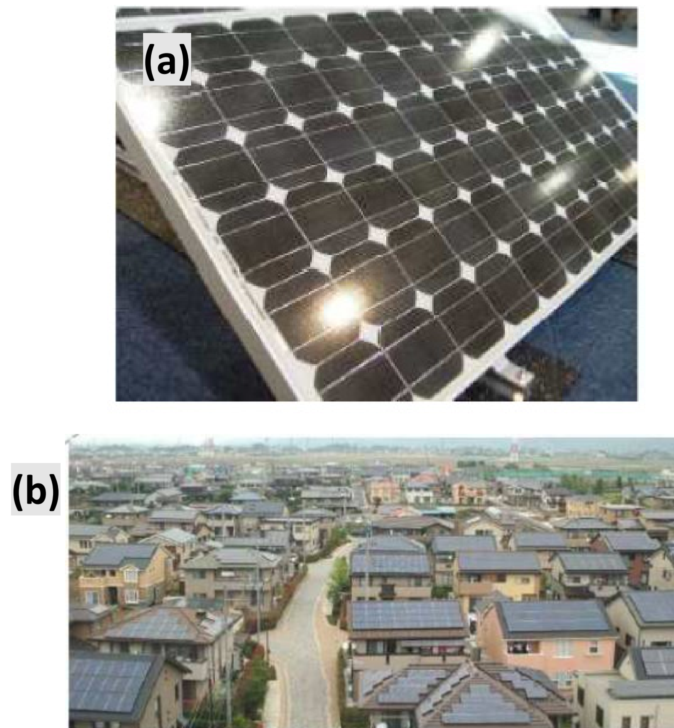

Figure 1.1 (a) a solar cells array module and (b) solar cells array modules on the roof.

In recent years, a lot of research has been focused on the high absorption of solar cells in order to achieve higher conversion efficiency. However, solar cells often work under harsh environmental conditions and it is one of the problems of low conversion efficiency of solar cells that dust accumulation can cause incident energy loss. Cleaning surface becomes an essential need to keep their stable conversion efficiency of solar cells in harsh environments. The "lotus-leaf self-cleaning", known as "lotus effect", is a valid strategy to clean the surface itself. Figure 1.2 shows a droplet which takes up the particles loosely covering the leaf while rolling off, and a scanning electron microscope (SEM) image of the micro and nano structures of the lotus leaf. The dirt or mud can be taken up and removed from the leaf surface by water droplets. A clean path becomes visible, where the dirt is removed. The ability of lotus plant, repel dirt, has inspired the laser interference patterning technology for self-cleaning applications that enables such an innovation in the area. Self-cleaning provides an effective way for life-time maintenance of the efficiency of solar cells used in a natural environment.

Thus, Biological surfaces in nature usually present excellent properties, such as the self-cleaning of the lotus leaf, and the antireflection of moth eyes. By studying the biological surfaces in living marvellous designs, scientists are using the newfound fantastic surface structures as inspiration to solve complex challenges and the biological products can save time and money. Great efforts have been undertaken to develop many kind of solar cells with different materials or different surface structures achieving excellent antireflection and self-cleaning properties in the past decades. Therefore, for the tremendous value of solar energy, solar cells deserve well-designed micro and nano surface structures to implement both functions of antireflection and self-cleaning according to the biological surfaces in nature. The traditional fabrication methods cannot fabricate the structures with the functions of antireflection and self-cleaning, and have the disadvantages of more pollution, random structures, expensive systems, difficult control and low efficiency. The novelty and contributions of this research are listed below.

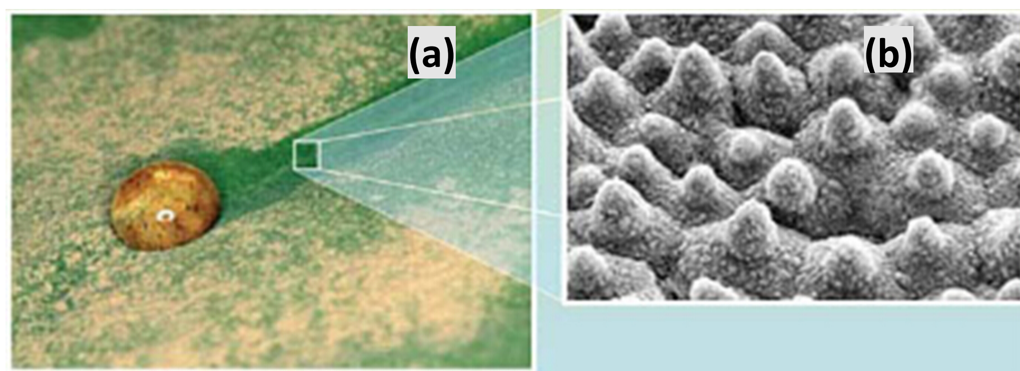

Figure 1.2 (a) a droplet takes up the particles loosely covering the leaf while rolling off and (b) a SEM image of the micro and nano structures of the lotus leaf.

- ☐ Solving the problems of traditional fabrication methods using laser interference lithography method with its significant advantages.
- ☐ Obtaining the surface structures with the functions of antireflection and self-cleaning, simultaneously.
- ☐ One step fabrication of triadic hierarchical silicon structures with excellent

antireflection and self-cleaning properties which are the same as the desired biological surface.

- Fabrication of a structure containing regular hexagonally-distributed holes with extremely low reflection and relatively large contact angle, using the three-beam laser interference lithography

Therefore, in order to improve the fabrication ability and implement both functions of antireflection and self-cleaning on the silicon surface, the laser interference lithography method is developed. This research investigates a number of strategies and technologies to achieve this goal.

1.2 Aim and Objectives of the Research

The main aim of this research is to investigate and develop a novel effective method for producing various patterns of micro and nano structures with antireflection and self-cleaning functions on silicon surfaces.

Specific objectives of this research are to:

- Conduct a survey of design and fabrication of antireflection and self-cleaning surfaces for solar cells;
- Analyse the relationship between micro and nano structures and antireflection and self-cleaning structures;
- Study and further develop the laser interference lithography (LIL) technology for the fabrication of various patterns of micro and nano structures;
- Fabricate various patterns of micro and nano structures and conduct experiments on these patterns in terms of effective solar energy collection.

1.3 Achievements

With respect to laser interference lithography interactions with silicon, the work contributes to the effects of heat transfer and plasma on silicon wafer surface process

and deduces the equations of heat flow and radiation effects of laser plasma of interfering patterns in a four-beam laser interference distribution. By changing laser parameters, different micro and nano morphologies of silicon wafer surface, such as gratings, holes and dots, have been obtained. According to the effects of heat transfer and plasma on silicon wafer, different micro and nano structures with undesired various structures have been studied and explained, such as the one grating changing to two gratings and silicon flowers. According to the resulting structures, the structure changes with different parameters can be obtained and properly selected for the fabrication of well-defined surface structures in the laser interference lithography process for various applications. For the antireflection and self-cleaning, some periodic structures with an extremely low solar-weighted reflection (SWR) and relatively large contact angle have been obtained by laser interference lithography in many experiments.

The achievements will be used in the fabrication of antireflection and self-cleaning surfaces of solar cells. Details of contribution of the work are given in later chapters. In Chapter 5, Laser Interference Interaction with Silicon Wafers, published in "Silicon Wafer Modification by Laser Interference", "Effect of Pulse Repetition Rate on Silicon Wafer Modification by Four-Beam Laser Interference", and "Effects of Laser Fluences on Silicon Modification by Four-beam Laser Interference", has been discussed for the effect of heat transfer and plasma on silicon wafer using laser interference lithography with equations for the effect of heat and plasma distribution. In Chapter 6, a novel triadic hierarchical structure on silicon wafer surfaces with antireflection and hydrophobic properties, presented in "One Step Fabrication of Triadic Hierarchical Silicon architectures with excellent Antireflection and Self-cleaning Properties". This triadic hierarchical structure fabricated by three-beam laser interference and one step fabrication. This kind of triadic hierarchical structures consists of a random array of conical micro structures, a regular hexagonally-distributed holes with the maximum periods of 1.4 μm located on the conical micro structures and some random nano dot structure evenly distributed on the conical structures with hexagonally-distributed holes. Excellent antireflection and hydrophobic properties have been obtained with an extremely low SWR (3.4%) and

relatively large contact angle (147°) providing a strong self-cleaning capability on the solar cell surface. In Chapter 7, Superhydrophobic Micro and Nano Dual Structures Fabricated by Direct Laser Interference Lithography, presents a method for the fabrication of highly-ordered superhydrophobic micro and nano dual structures on silicon by direct laser interference lithography (LIL). The superhydrophobic surface with the contact angle of 153.2° is achieved after the exposure of 60 seconds. In Chapter 8, "Antireflection Silicon Structures with Hydrophobic Property Fabricated by Three-beam Laser Interference", demonstrates antireflective structures on silicon wafer surfaces with hydrophobic properties fabricated by three-beam laser interference. Compared with existing technologies, the array of hexagonally-distributed hole structures fabricated by three-beam laser interference reveals a design guideline to achieve a considerably low solar-weighted reflectance (SWR) (1.86%) in the wavelength range of 300 nm to 780 nm and relatively large contact angle (140°) providing a strong self-cleaning capability on the solar cell surface.

1.4 Implementation and Support

This work has been carried out at the Joint Research Centre for Computer-controlled Nanomanufacturing (JR3CN), University of Bedfordshire (UoB) and Changchun University of Science and Technology (CUST).

It has been funded by different institutions, and supported by National Key Basic Research Program of China (973 Program No.2012CB326406), Special Development Program of Central Financial Support to Local Universities (No.2011-183), EU FP7 (LaserNaMi No.247644; ECNANOMAN No.269219), International Science and Technology Cooperation Program of China (No.2012DFA11070), National Natural Science Foundation Program of China (No.60940035 and No.61176002), Doctoral Program of Higher Education of China (No.20112216110002), Jilin Provincial Science and Technology Program (No.20100703, No.201024, No.201115157, No.20090401, No.20110704 and No.20100703), Guangdong Science and Technology Program

(No.2009B091300006 and No.2011B010700101), Science and Technology Program of Changchun City (No.09GH07 and No.11KP04), and Program of Changchun University of Science and Technology (No.129666 and No.XJJLG201101).

1.5 Structure of This Thesis

This thesis is divided in 9 Chapters. Chapter 1 introduces the current work of antireflection and self-cleaning of solar cells and presents the main objectives and achievements of this thesis. Chapter 2 summarizes the main fabrication methods of antireflection and self-cleaning surfaces and gives the advantages of laser interference technology. In this review, the background of solar cells is first briefly introduced. It then focuses on the fabrication methods of antireflection and self-cleaning surfaces and compares the advantages and drawbacks of these methods. In addition, the main micro and nano structures of antireflection and self-cleaning surfaces are shown. Chapter 3 introduces in detail the theories of laser interference, antireflection and self-cleaning. Chapter 4 details the fabrication and characterization of multiple-beam laser interference lithography employed in this thesis and shows the measurement systems for reflection measurement and contact angle measurement, used in this thesis. Chapter 5 discusses the multiple-beam laser interference lithography interaction with silicon wafer. Two-beam, three-beam and four-beam laser interference is used to pattern single crystal silicon wafers for the fabrication of various structures, and the numbers of laser pulses, different laser pulse repetition rates, different laser influence and incident angles are applied to the process in the air. The effects of the heat transfer and the radiation effects of laser interference plasma on silicon wafer surfaces are investigated. The equations of heat flow and radiation effects of laser plasma of interfering patterns in a four-beam laser interference distribution are proposed to describe their laser radiation impacts on silicon wafer surfaces. Chapter 6 provides a novel triadic micro and nano structures having a lower reflection (SWR of 3.4%) and larger contact angle on the silicon wafer surface. Chapter 7 presents highly-ordered superhydrophobic micro and nano dual structures on silicon fabricated by four-beam

direct laser interference lithography. The superhydrophobic surface with the CA of 153.2° is achieved after the exposure of 600 laser pulses. Chapter 8 demonstrates antireflective structures on silicon wafer surfaces with hydrophobic property fabricated by three-beam laser interference. A three-beam laser interference system is set up to generate periodic micro and nano hole structures with hexagonal distributions. Furthermore, compared with the existing technologies, the array of hexagonally-distributed hole structures fabricated by three-beam laser interference reveals a design guideline to achieve a considerably low solar-weighted reflectance (SWR) in the wavelength range of 300 nm to 780 nm. The last Chapter of this thesis, Chapter 9, summarizes conclusions of the work and comments on future research. Past successes and current progress indicate that different micro and nano patterns fabricated by laser interference lithography have numerous potential future applications.

Chapter 2

Literature Survey on the Fabricated Antireflection and Self-cleaning Surfaces

In the last decades there have been various chemical and physical technologies that can be used to modify or pattern materials for fabricating different surfaces with the functions of antireflection and self-cleaning properties for solar cells. In the first section of this Chapter, a brief introduction presents background and working principles of solar cells. The second and third parts provide the main fabrication methods of antireflection and self-cleaning technologies, and also discuss their main advantages, drawbacks and achievements. Then, the micro and nano structures for antireflection and self-cleaning, such as silicon grating, nanowires (NWs), nanopillars, nanocones (NCs) and nanoholes (NHs), are introduced and exampled. At the end of the Chapter the main fabrication methods of antireflection and self-cleaning for the laser interference lithography technology are summarised.

2.1 Solar Cells

2.1.1 Background of Solar Cells

In 1839, Edmond et al. found that "two different brass plates immersed in a liquid could produce current when it was illuminated by sunlight". In 1870s, Willoughby Smith et al. discovered "a PV effect in selenium". By 1954, Chapin et al. [7] had invented that the monocrystalline silicon solar cell had 6% efficiency. Up to now, researchers have obtained the silicon solar cell efficiency up to as high as 20%. Moreover, the monocrystalline silicon, the dominative material of commercial solar cells, possesses a mature production and the processing technology well developed in the modern semiconductor industry. However, this kind of material costs very much for its expensive purification procedure and occupies the main cost in production of solar cells [8]. The polycrystalline silicon cells became increasingly popular during the 1990s. By

2007, the polycrystalline cells modules have been sold to about 45% in the solar cells market. Typical efficiencies of polycrystalline cells are around 14%, which is lower than monocrystalline silicon. In the recent research of solar cells, researchers pay more attention on the enhancement of light-trap efficiency in thin-film solar cells. There are three thin-film technologies, Cadmium telluride (CdTe), copper indium gallium selenide (CIGS) and amorphous silicon (a-Si), often used for outdoor applications. The efficiency of GaAs thin film technology in the lab reached 28% and the laboratory efficiency of CIGS technology reached 20.4% [9].

During the 1980s and 1990s, solar cells began to be generally used to provide electrical power on the roofs of urban and suburban homes, office buildings, and so on. Today, solar cell used to provided electrical power energy has become mostly important sources of energy in the world, and the solar cell electrical power is one of the best ways to generate electrical power [8].

2.1.2 Working Principles of Solar Cells

All of solar cells working principles are generally and essentially based on the photovoltaic effect. The photovoltaic effect is that the formation junction of two different materials in response to visible or other radiation that generates a potential difference. Figure 2.1 shows the generation of physical phenomena of materials when solar energy is irradiating.

The basic processes of the photovoltaic effect when photons hit the semiconductor materials are [8]:

- ☐ Due to the absorption of photons in the materials, the charge carriers are generated and a junction is formed.
- ☐ The photo-generated charge carriers in the junction are subsequently separated.
- ☐ The photo-generated charge carriers at the terminals of the junction are collected.

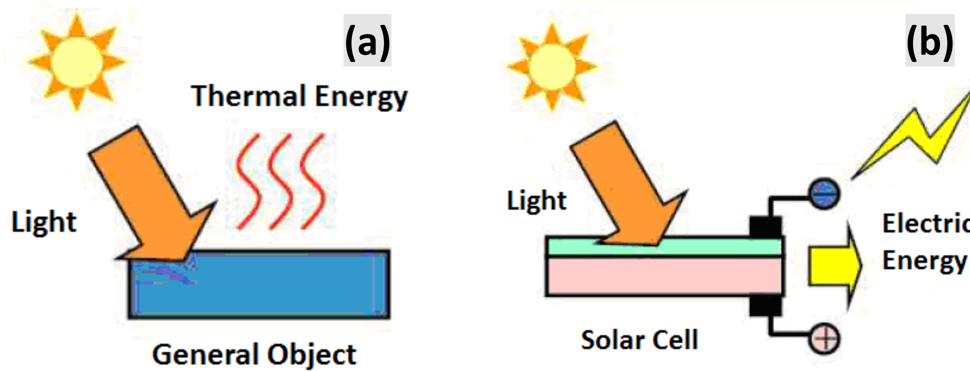

Figure 2.1 The physical phenomena of materials when solar energy is irradiating, (a) is the general object and (b) is the solar cell.

A solar cell structure generally consists of an absorbing layer. When the photons from sunlight hit the semiconductor, they can be absorbed to result the electron-hole pairs. The electrons flow into the N region and the holes flow into the P region. The P region is positive and the N region is negative. The layer between the N and P regions would generate an electromotive force that is the photovoltaic effect. P-N junctions as known are especially and mostly important for solar cells. The carriers which have opposite charge in the electric field are drifted from each other in the opposite directions reaching the electrodes on the solar cell. Figure 2.2 shows the principle of photovoltaic effect.

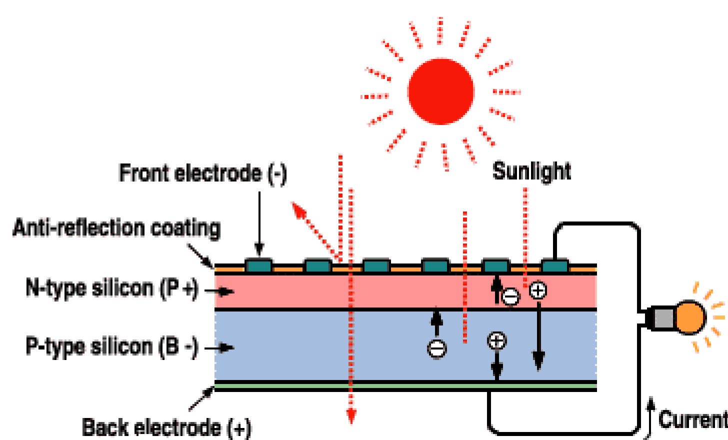

Figure 2.2 The principle of photovoltaic effect with more details [9].

2.2 Current Fabrication Methods of Antireflection

High optical loss of solar cell surfaces is a serious obstacle to improve the conversion efficiency of the solar cells. There are two important ways to reduce the optical loss of the solar cell surfaces. One is the use of antireflection films for solar cell surfaces and the other is the use of antireflection structures having the light trapping function on the solar cell surfaces. A number of approaches for the fabrication of antireflection layer have been proposed by worldwide scientists, for example, the chemical etching method, the antireflection film method and some lithography technologies.

2.2.1 The Chemical Etching Method

Monocrystalline silicon surface texturing is mainly obtained by chemical etching in the mass production. It conventionally uses the alkaline solution to produce random pyramid textures on crystalline silicon [10, 11]. Mostly, the random pyramids have dimensions of the range of several microns, and the light can be reflected from one pyramid surface to another pyramid surface in the microns pyramid structure. Therefore, the light having more chance can be absorbed by this kind micro pyramid structure. Figure 2.3 shows SEM images of a chemically textured silicon surface. Sparber et al. [10]reported that "the solutions of potassium hydroxide (KOH), isopropyl alcohol (IPA), sodium carbonate (Na_2CO_3) and sodium hydrogen carbonate ($NaHCO_3$) were used on the surface of silicon to produce textures". They achieved "weighted reflectance values as low as 12.5% and 16.5% respectively with the two solutions"**[**10**].** The methods are simple, but they can only produce randomly distributed structures on the silicon wafer surfaces due to the issues associated with controlling the etching rate and uniformity, and the reaction process can cause pollution.

Precious metal particles assisted etching, such as silver, gold and platinum, is one of the chemical etaching method [12, 13]. Srivastava et al. [14] reported that "large area silicon nanowires were realized by silver induced wet chemical etching of p-silicon (1 0 0) substrates in aqueous HF and $AgNO_3$ solution at room temperature". The value of reflection is less than 2% in the wavelength range of 300–600 nm. Figure 2.4 shows the

SEM images of VA-SiNWA obtained after 45 min etching [14]. Such method can realize the very low reference on the silicon surface, but the fabricated system of nanowires is very complex, the environmental requirements are relatively high, and it results in higher production costs.

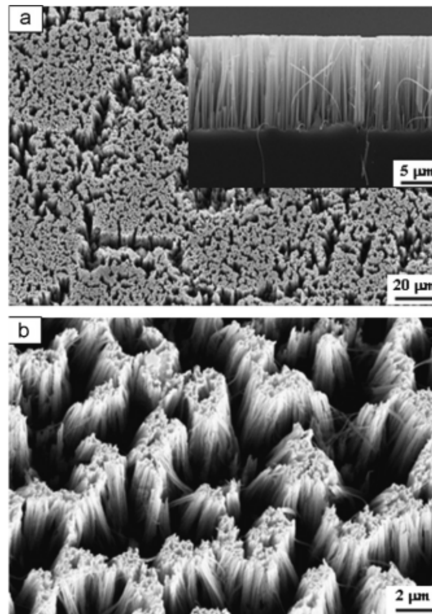

Figure 2.3 SEM images of chemically textured silicon surface [11].

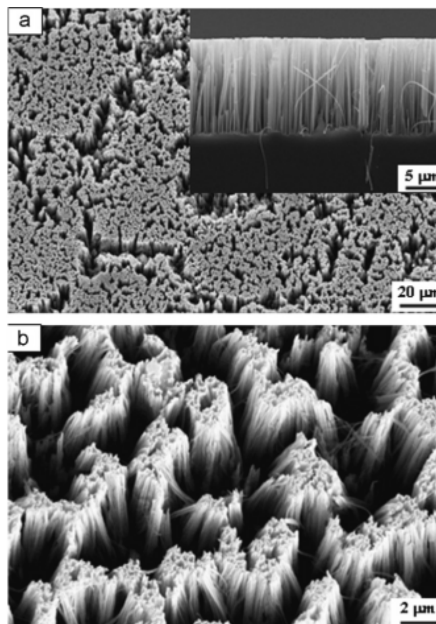

Figure 2.4 SEM images of silicon nanowires obtained after 45 min etching. (a) is top view and the inset shows the cross-sectional view of Si wires, and (b) is magnified tilted view with angle of tilt 12° [14].

Another method is that alkaline etching method is combined with the precious metals particles assisted etching method. Qi et al. [15] reported that "by employing the KOH etching and silver catalytic etching, pyramidal hierarchical structures were generated on the crystalline silicon wafer". This structured silicon wafer exhibits excellent antireflection property in broadband wavelength range and this structured silicon surface also shows superhydrophobic behaviour. Figure 2.5 shows the fabrication procedure for creating hierarchical structures on the silicon surface [15]. It has good antireflection and superhydrophobic character, but also has the both disadvantages of alkaline etching method and the precious metal particles assisted etching method.

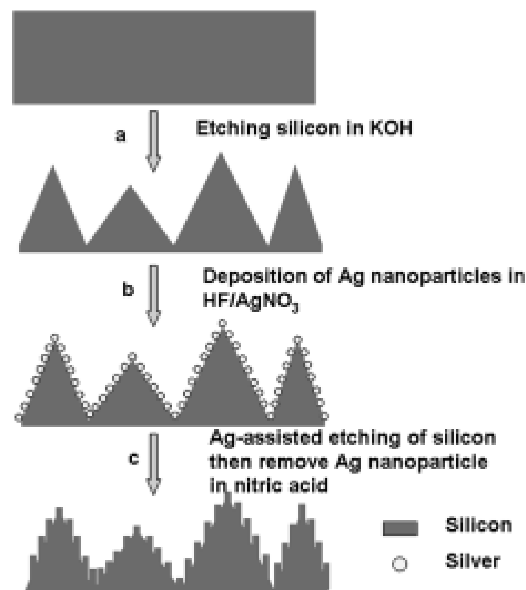

Figure 2.5 Fabrication procedure for creating hierarchical structures on the silicon surface, (a) is fabrication of pyramidal structures on silicon surface with KOH etching, (b) is electroless deposition of a thin discontinuous layer of Ag nanoparticles on the pyramidal structures in HF/AgNO3 solution and (c) is generation of hierarchical structures with Ag-assisted etching and then removal of Ag nanoparticles in nitric acid [15].

2.2.2 The Antireflection Film Method

Antireflection coating (ARC) is a type of optical coating used in a variety of optical lenses, flat panel displays and solar cells to reduce reflection [6]. Such ARC generally used transparent quarter wavelength layers of SiOx , TiOx , or SixNy having intermediate or gradient refractive indices [16]. ARC can be formed of single or multiple layer film deposition using various processes such as plasma enhanced chemical vapour

deposition, sputtering processes, wet coating, sol-gel methods and so on. Silicon nitride (SiNx) is one of the useful ARC for solar cells. Plasma enhanced chemical vapour deposition (PECVD) is being increasingly used for the fabrication of transparent dielectric optical films and coatings. SiNx films formed by PECVD technology is another method. The method provides excellent surfaces texturing for good antireflection properties. However, the PECVD system is fairly expensive[17]. Furthermore, these coatings have several problems such as thermal mismatch, adhesiveness and stability, which affect the working life, conversion efficiency, and so on [14].

2.2.3 The Lithography Technologies Methods

There are a number of lithography technologies developed for fabrication of nano structures such as electron beam lithography (EBL), ion beam lithography (IBL), scanning probe lithography (SPL), nano imprint lithography (NIL) and nano sphere lithography (NSL) [18]. These technologies can periodically micro and nano structures in fabricate high resolution. For each technology, a predefined geometry can be transferred to the target material aligned to the previous one at the same time and formed regular high resolution structures.

Electron beam lithography (EBL) and Ion beam lithography (IBL) have been developed to the powerful technologies for results with higher resolution below 50nm. They are always used for the fabrication of marks in order to produce the larger area micro and nano structures. Chen et al. reported the method for the fabrication of nano-structured Si moulds by e-beam lithography and chemical wet etching. In addition, the structures showed a significant reduction of reflectance (<6%) over the entire wavelength range at normal incidence [19].

Scanning probe lithography (SPL) has used a scanning tunnelling microscope or atomic force microscope to apply chemicals to a surface or manually modify the martial surface. The advantages of the SPL are its high resolution pattern, simplicity and low cost.

However, the main drawback of the EBL, IBL and SPL is that they are time consuming as the result of their serial point-by-point writing modality. Thus, these technologies are extremely slow and not suitable for mass production.

Nano imprint lithography (NIL) offers a low-cost way to mass production of nano-surface structures, but it has the disadvantages that the technology can only be used in a clean surface, and the template design shape is fixed. Han et al. reported that "a nanometer scale dot-pattern array was formed on the surface of GaInP/Ga(In)As/Ge solar cells by nano-imprint lithography" [19]. At the wavelength of 550 nm, GaAs cells with patterns show 6.21% of reflectance [19].

Nano sphere lithography (NSL) applies "planar ordered arrays of nanometer-sized metal or silica spheres as lithography masks to fabricate nanoparticle arrays" [20]. Zhang et al reported that "highly-ordered silicon inverted nanocone arrays are fabricated by integration of nanosphere lithography with reactive ion etching (RIE) method" [21]. The reflectance intensity of Si inverted nanocone arrays is less than 7% over broad range of 400 to 1,000 nm [21].

Focused laser processing was widely used for the texturization of silicon surfaces for the fabrication of solar cells, and the black silicon with superior absorption property was demonstrated [22]. Figure 2.6 shows the schematic diagram of a typical focused laser processing technology. The amount of material removed by a single laser pulse depends on the material modification threshold and the laser fluence. Laser processing with multiple laser pulses on silicon wafer was studied to understand surface modification process of silicon wafer by cumulative laser fluence [1]. A useful application by laser processing on silicon wafer is black silicon with its superior absorption property for solar cells [23, 24]. Focused laser processing technologies can produce regular micro structures, but they are all time consuming approaches which are not suitable for low-cost mass production due to the laser scanning speed limit.

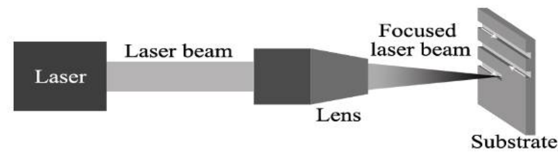

Figure 2.6 Schematic diagram of a typical focused laser processing technology.

An alternative approach is **laser interference lithography technology**, which is "concerned with the use of interference patterns generated from two or several coherent beams of laser radiation for the modification of materials" [25, 26]. The interference patterns can be arrays or matrices of laser beam lines or dots. Laser interference lithography has the following advantages compared with other micro and nanolithography technologies [27]:

- Very high throughput (1 pattern/pulse within 10ns): a pattern has especially produced by high power pulsed lasers, such as excimers and Nd: YAG lasers, on the sample surface. High power pulsed lasers have very high throughput that only a single pulse in the rage of nano-seconds produces a pattern.
- Low cost: compared with other high resolution lithography technology, such as EBL and FIB, the implementation of laser interference technology is low-cost.
- Programme controlled re-configurable patterns: with different periods, feature sizes and pattern shapes can be reconfigured in the optical setup.
- Surface contamination-free: there are no moulds or masks in contact with the sample when the process is working. If the working process is in the vacuum environment, it is just the interaction between the light and the material inducing the surface modifications.
- Creation of structures on large areas: a pattern size of up to hundreds of millimetres in diameter is obtained

- ☐ Long working distance: flexible coherence lengths and modification the energy thresholds of materials.
- ☐ Direct and indirect technology: interference lithography is used to modify a variety of materials such as metals, ceramics or polymers.

Thus, laser interference lithography is used in recent years as a maskless low-cost and high throughput technology to produce periodic and quasi-periodic structures for a number of applications such as gratings, sensors, antireflection and self-cleaning materials. However, like the approaches developed by IBM, MIT and others, this technology has been developed for a multi-step process that "includes recording an interference pattern on photoresist followed by a series of process to transfer the pattern into the underlying layer. Every step should be performed carefully since an error in any step could lead to the failure of final results. In this point of view and the industrial needs to lower the fabrication cost, fewer steps are desired" [28].

From the literature review in brief of laser interference lithography, it has been demonstrated that laser interference lithography has a number of advantages compared to other technologies and in additional shows clearly in the bullet points. Table 2.1 shows the advantages and disadvantages of the fabrication methods of antireflection.

Table 2.1 Advantages and Disadvantages of the Fabrication Methods of Antireflection

<table>
<tr><th colspan="2">Methods</th><th>Advantages</th><th>Disadvantage</th></tr>
<tr><td rowspan="2">Chemical etching method</td><td>Alkaline etching method</td><td>Simple</td><td>Random pyramid, more pollution</td></tr>
<tr><td>Precious metal particles assisted etching</td><td>Low reference, large area</td><td>Very complex system, high environmental requirements, and higher production costs</td></tr>
</table>

	Alkaline etching method combined with the precious metal particles assisted etching method	Good antireflection and superhydrophobic character.	Having disadvantages of alkaline etching method and the precious metal particles assisted etching method.
The antireflection film method	Silicon nitride film	Excellent surface texturing and good antireflection properties.	Expensive system, the problems of thermal mismatch, adhesiveness, stability, etc.
The lithography technologies method	Electron beam lithograph	High resolution micro and nano structures, Flexible pattern	They are always used for High cost, low efficiency
	Ion beam lithography	High resolution micro and nano structures, Flexible pattern	High cost, low efficiency
	Scanning probe lithography	High resolution micro and nano structures, Flexible pattern	Limited materials, low efficiency
	Nano imprint lithography	High resolution micro and nano structures, Mass production	Template dependent
	Focused laser processing	Large area	Laser scanning speed limit low efficiency
	Laser interference	Easy control, low	Multiple processes

	lithography	cost, high efficiency	

2.3 Overview of the Fabrication Methods of Self-cleaning

The lotus leaf has the self-cleaning function which can pick up the dirty and dust particles by water droplets due to a complex micro and nano scale architecture of the surface and the waxy crystal [1]. “A water repellent surface exhibits certain remarkable wetting properties originating from very high contact angles (>150°) and very small values of contact angle hysteresis (less than 58°) , and the droplets roll down these surfaces at a speed faster than that of a solid sphere rolling under gravity” [29]. They can fully bounce after impacting the surface whereas the time of contact of an impacting droplet with the surface is independent of its velocity [30]. This natural super-hydrophobic phenomenon provides a guideline to produce artificial super-hydrophobic surface structure. In recent years, the chemical and physical methods have been used for the fabrication of superhydrophobic surfaces. There are many methods to fabricate self-cleaning structures.

2.3.1 Phase Separation and Self-assembly Method

Erbil et al. [31] reported “a method for forming a superhydrophobic coating using polypropylene (a simple polymer) and a suitable selection of solvents and temperature to control the surface roughness. The resulting gel-like porous coating had a water contact angle of 160°”. However, this method cannot be easily controlled and the structure obtained is random. Yabu et al. [32] described “a simple preparation of super-hydrophobic and lipophobic surfaces by self-assembly”. They obtained an orderly pincushion-like structure and showed that the superhydrophobic behaviour was achieved with the maximum contact angle of 170°. However, the phase separation or self-assembly method can only be used for small surface areas, and the super-hydrophobic surface can easily be destroyed with high temperature.

2.3.2 Hydrothermal Method

This method has made the nanoparticles orderly growth or rearrangement on the substrate surface. Wu et al. [33] demonstrated the growth of ZnO crystalline with a microstructure surface fabricated by wet chemical method. The result of contact angle of the structure was larger than 150°. Hosono et al. [34] showed the contact angle of 178°. They used similar method to obtained a growing the shape of needle-like structures on the substrate of borosilicate glass. However, this method cannot produce the surface structure in a controlled manner.

2.3.3 Chemical Deposition and Electrodeposition Method

The third is "Chemical deposition and electrodeposition method" [1]. Liu et al. [35] fabricated a superhydrophobic ZnO thin film using the Au-catalyzed chemical vapour deposition method. The obtained water contact angle was 164.3° and superhydrophilic one < 5°. Wang et al. [36] described that “highly stable gold micro and nanostructures with various morphologies were fabricated using a galvanic exchange reaction”. They obtained “superhydrophobic surface (contact angle 165°) similar to the lotus leaf” [36]. However, the equipment is expensive, and the condition of using the equipment is strict.

2.3.4 Lithography and Laser Etching Method

The use of lithography and laser-etching method also obtained regular super-hydrophobic surface structures except antireflection structures [37]. Öner et al. [38] showed that the wettability properties of silicon surfaces prepared by photo-lithography. They found that when the distance of two rods was smaller than 32um, the contact angle was greater than 160°. The disadvantage of this method is that it can only produce small areas of the surfaces with a complicated fabrication process.

Apart from the above methods, there are some other methods producing super-hydrophobic surface structures, such as Electrospinning, Sol-gel and Carbon

nano-tubes methods [1]. The methods are either complicated or uncontrollable.

2.4 Micro and Nano Structures for Antireflection and Self-cleaning

Among different extensively investigated micro and nanoscale structures for antireflection and self-cleaning, different micro and nano structures, such as silicon grating, nanowires (NWs), nanopillars, nanocones (NCs) and nanoholes (NHs) [39], have been regarded as substantially promising targets due to their special properties optical properties and hydrophobic effects. These structures have been shown in Figures 2.7-2.10. These nano structures have very low reflectivity.

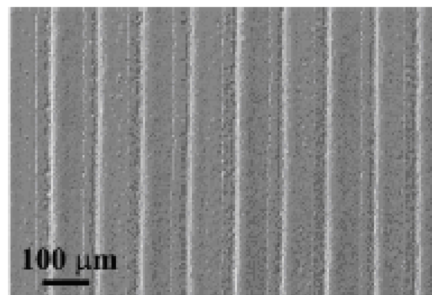

Figure 2.7 SEM image of the micro grating structures [40].

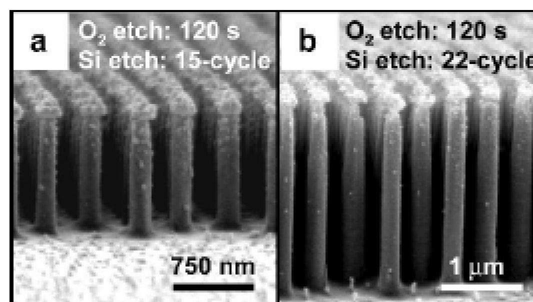

Figure 2.8 SEM images of nanopillars fabricated from a polystyrene bead patterned silicon surface [20].

2.5 Laser Interference Method to Produce Micro and Nano Scale Structures for Antireflection and Self-cleaning

Laser interference lithography is a potential technology that can produce regular micro and nano structured patterns on silicon wafers for solar cells. Up to now, many efforts in our team have been devoted to study or fabricate useful micro and nano structures for different applications using LIL. Zhang et al. fabricated periodic antireflection

structures with the average reflectance of 3.5% on silicon using four-beam laser interference lithography, as shown in Figure 2.11 [41]. Wang et al. proposed both antireflection and superhydrophobicity structures fabricated by direct laser interference nanomanufacturing and the contact angle and reflectance were 156.3^{o} and 5.9-15.4%, as shown in Figures 2.12 and 2.13 [42]. The antireflection and self-cleaning functions were due to the formation of an array of micro cone and hole structures on silicon wafer surfaces. In addition, there are some good results from other teams for researching laser interference lithography. Zhang et al reported Laser interference photolithography for fabricating periodic patterns in large area and they theoretically analyzed the patterns of multiple-beam laser interference lithography [43]. Xie at al fabricated a nanostructures using laser interference lithography [44].

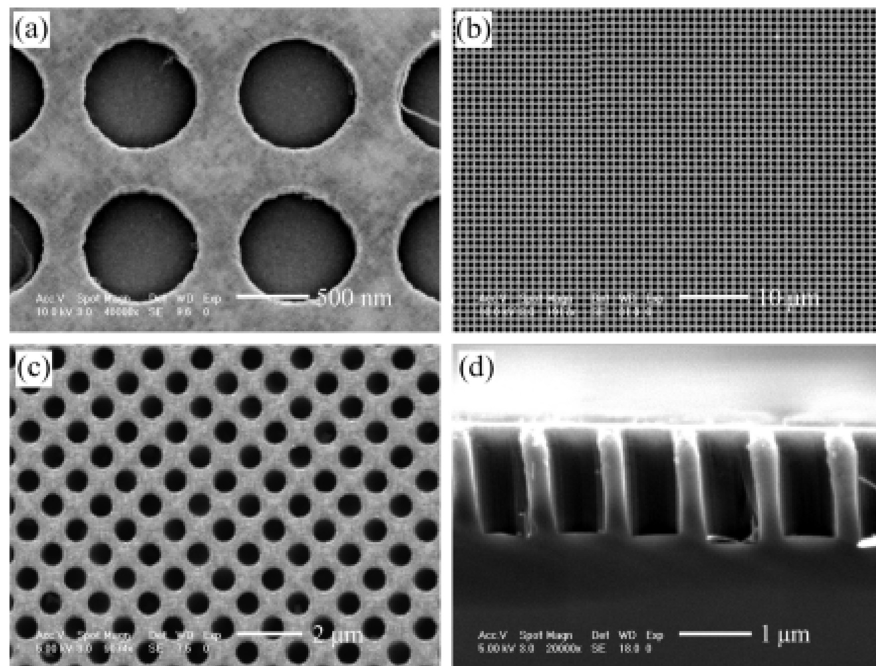

Figure 2.9 SEM images of silicon nanoholes produced in p-Si (100) wafer, (a) is Top-view SEM image, (b) and (c) are top-view SEM images of ordered silicon nanoholes with large depths, and (d) is cross-sectional view of silicon nanoholes [45].

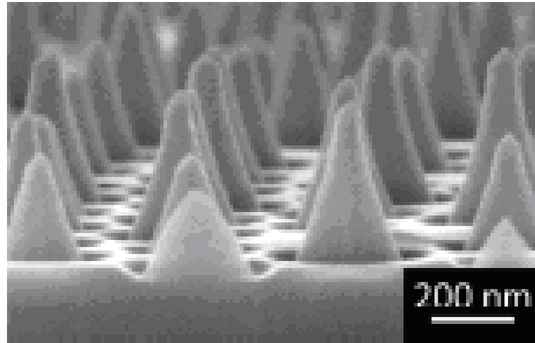

Figure 2.10 SEM image of cross-sectional view of Si nanocones [46].

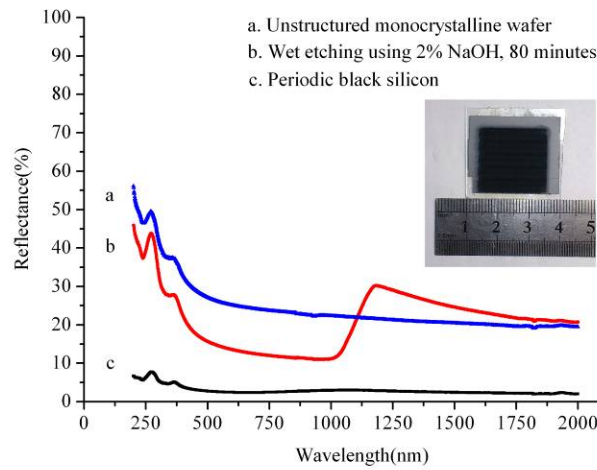

Figure 2.11 Measured reflectance spectra of surfaces: (a) unstructured monocrystalline wafer, (b) wet etching specimen, (c) periodic black silicon fabricated by four-beam LIL in SF6.

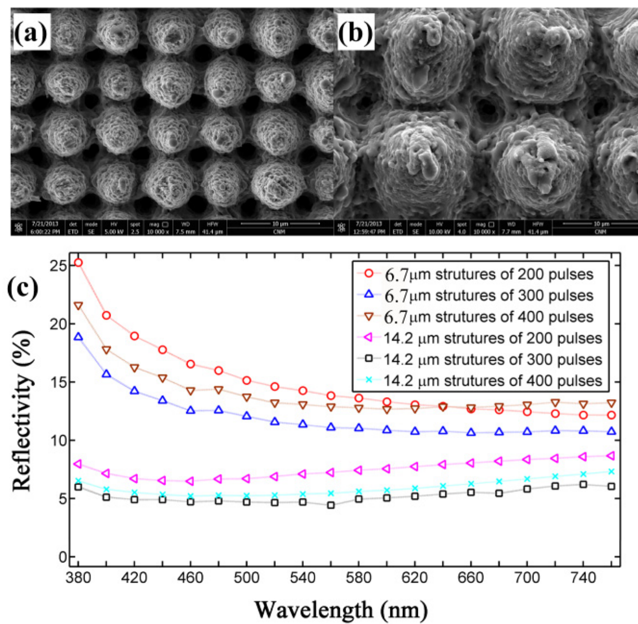

Figure 2.12 Topographies of structures (a) Period of 6.7 μm; (b) Period of 14.2 μm; (c) Reflectance spectra of the two micro cone structures with exposures of 20s, 30s and 40s.

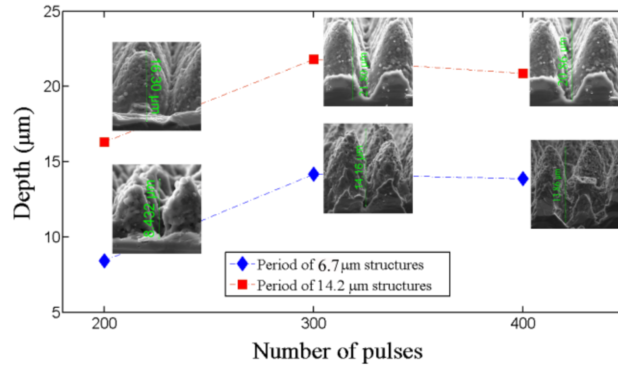

Figure 2.13 Structural depths of samples as a function of the number of laser pulses.

2.6 Summary

In this chapter, the background and working principles of solar cells and a number of the fabrication methods of antireflection and self-cleaning for solar cells have been reviewed. Moreover, the micro and nano structures have also been discussed. The advantages and disadvantages of the methods and structures have been compared and exposed. It can be seen that the laser interference lithography has a great significance for the fabrication of antireflection and self-cleaning of solar cells surface. According to these and different applications, the fabrication method will be employed and further developed in this thesis and novel work is outlined as follows.

- Silicon surfaces, the main material of fabricated solar cells, can be directly and indirectly modified by laser interference.

  In this thesis, the sample substrate is monocrystalline silicon because silicon is the domain material of solar cells production. However, the highest conversion efficiency of solar cells in the current research is always about 25.6% and has not been improved for a considerable period of time. The reflection loss of the incident light on the solar cells is one of the reasons of low conversion efficiency. Thus, this thesis aims to improve conversion efficiency of the solar cell.
- Laser interference patterns are used to create well-defined surface structures.

  Laser interference lithography can generate various patterns and be applied to direct writing or indirect writing technology on substrate compared to traditional

fabrication methods for solar cells surface.

- Grating, square and hexagon structures and so on are made by multi-beam laser interference.

  Various structures can be obtained using laser interference lithography in order to analyse the relationship between micro and nano structures and antireflection and self-cleaning structures.

- Effects of heat transfer and plasma structure features are obtained from different laser interference parameters.

  It is to understand that the relationships of laser interference parameters and laser interference pattern and eventually to analyse the relationship between micro and nano structures and antireflection and self-cleaning structures.

- The fabrication of the laser interference patterns can lead to excellent functions of antireflections and self-cleaning properties.

  The contributions of this thesis are the resulting periodic hexagonally-distributed hole structures with an extremely low SWR (1.86%) and relatively large contact angle (140°) providing a strong self-cleaning capability on the solar cell surface; one step fabrication of the hierarchical silicon structures has a large contact angle (147°) and relatively low SWR (3.4%) as shown in chapters 6 and 8.

Chapter 3
Methodologies for the Research

3.1 Laser Interference

3.1.1 Theory of Laser Interference

Laser interference lithography technology is concerned with the use of interference patterns generated from two or several coherent beams of laser radiation for the modification of materials [25, 26]. The interference pattern containing all information about the two interfering beams is created as shown in Figure 3.1. The consisting of dark and bright spots of the resulting pattern is due to their intensity and phase relation [47]. The coherence requirements must be met in order to make the interference lithography successful occurs.

- ☐ Use of a spatially coherent light source
- ☐ Non-orthogonal polarization states
- ☐ Spatial and temporal overlap of two light fields

In fact, there is the possibility of being observed with interference effect for any of single-frequency waves while they overlap. The ideal interference source is the light consisting of a very narrow spectrum of frequency. Therefore, laser has been appropriate to widely many kinds of applications based on interference principle.

Generally, a coherent light source generates a beam that is divided into two or more beams by beam splitting, which are utterly impacted to one point on a surface of sample being the target material or an intermediate layer, such as a photoresist. The beams interacted with each other generated the interference pattern. These interference patters have maximum and minimum intensity peaks resulting in a non homogeneous intensity distribution and forming arrays and matrices of lines or dots.

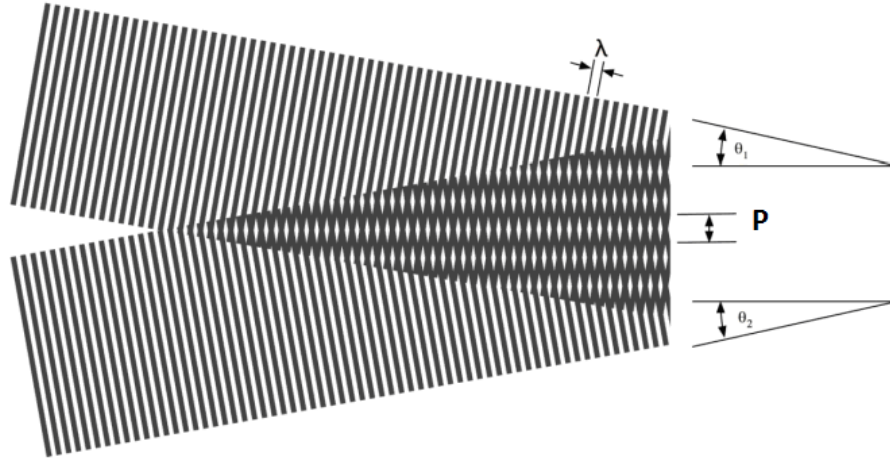

Figure 3.1 Interference of two coherent laser beams[47].

The schematic diagram of two-beam laser interference lithography are shown in Figure 3.2 and Figure 3.3 From the two figures, they can be seen that arrays or matrices of laser beam lines or dots can be formed by multi-beam laser interference. For two-beam laser interference, the pattern is an array of lines or grating. The intensity distribution of the interference pattern *I* can be expressed as [48]

$$I = 2I_0[1+\cos(2kx\sin\theta)] \tag{3.1}$$

where I_0 is the intensity of the two beams, $k = 2\pi/\lambda$ is the wave number, λ is the wavelength of the laser, and θ is the beam incident angle.

The period of the fringe pattern *P* can be calculated by

$$P = \frac{\lambda}{2\sin\theta} \tag{3.2}$$

The pattern period is a function of the wavelength (λ) and the incident angle of the beams (θ). It indicates that the period can be adjusted from nano to micro meters, which is flexible for many applications.

For the multi-beam interference, it can be described as the superposition of electric field vectors of three or more laser beams, and it can be written as

$$\vec{E} = \sum_{i=1}^{m} \vec{E}_i = \sum_{i=1}^{m} A_i\vec{P}_i\cos(k\vec{n}_i\cdot\vec{r}_i \pm 2\pi\omega t + \phi_i) \tag{3.3}$$

where A_i is the amplitude, $\vec{P}_i$ is the unit polarization vector, $k = 2\pi/\lambda$ is the wave

number, λ is the wavelength, $\vec{n}_i$ is the unit propagation vector, $\vec{r}_i$ is the position vector, ϕ_i is the phase constant, m is the number of the beam and ω is the frequency.

The intensity distribution of the interference pattern *I* can be expressed as

$$I = \sum_{i=1}^{m} |\vec{E}_i|^2 = \sum_{i=1}^{m}\sum_{t=1}^{m} |\vec{E}_i||\vec{E}_t| \cos < \vec{E}_i \cdot \vec{E}_t > \tag{3.4}$$

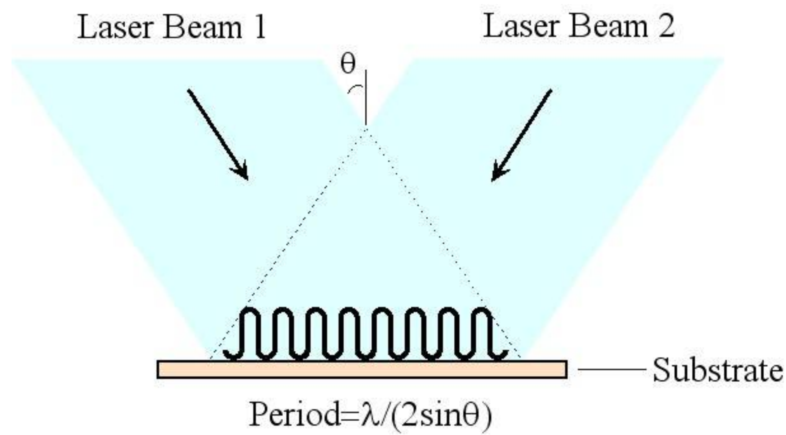

Figure 3.2 Schematic diagram of two-beam.

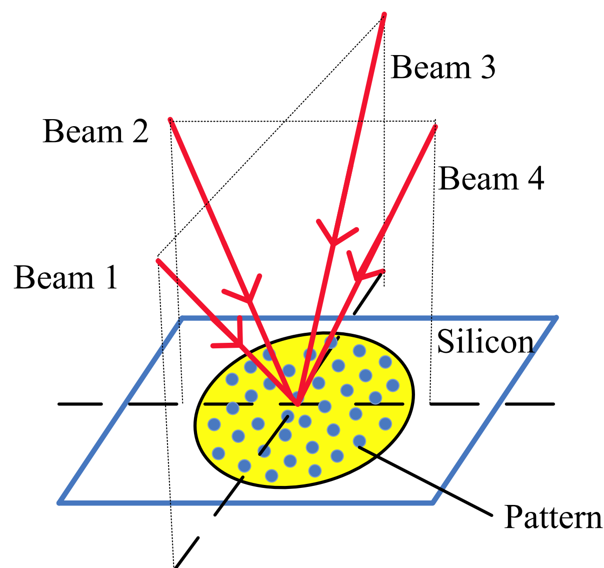

Figure 3.3 Schematic diagram of four-beam.

3.1.2 System Requirements of Laser Interference

The system of multi-beam laser interference can resolve the various users 'application requirements, such as:

- Substrates: Dimensions and thickness of substrate.
- Features: Feature size and geometry.
- Process materials: According to the type and thickness, direct writing or indirect writing can be chosen.
- Equipment: Easy installation, high efficiency of throughput and low cost of equipment.

There are nine parts in this system and each part has separated functions for different combinations of components for the user to choose. Figure 3.4 shows a scheme of a multi-beam laser interference lithography system, which consists laser radiation, beam shaping, beam splitting, phase control, interference control, polarization control, beam monitoring, sample positioning and system control [49].

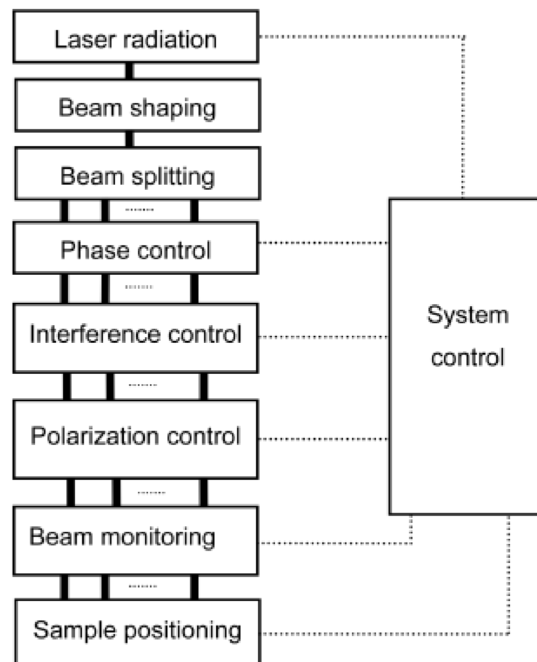

Figure 3.4 Scheme of a multi-beam laser interference lithography system [49].

The laser radiation can supply coherent light with the user required wavelength, power and coherence length. Beam shaping can transform the Gaussian beams into a flat-top distribution before interference to produce a uniform pattern. Beam splitting can be

needed to require several coherent beams for a laser interference lithography system. Phase control can control the phases of interfering beams, so that control the pattern orientation or pattern localization. Interference control can arrange of the coherent beams based on control of the beams parameters and optimization of optical path length to form the required interference patterns. Polarization control can arrange the polarization states of interfering beams to form the required interference patterns and is able to select the polarization states of interfering beams to produce required interference patterns. Beam monitoring can concern to the monitoring of a multi-beam interference lithography process, such as tuning of the interference pattern parameters and monitoring of the beam parameters. The interference pattern parameters contain period, feature size, size and pattern shape according to the samples application before processing. The monitoring of the beam parameters contain intensity, shape and polarization and can ensure the beams quality. Sample positioning can posit the samples, rotate the samples and repeat the processing sample.

3.1.3 Characteristics of Laser Interference

A brief summary can demonstrate that the laser interference lithography system has a number of advantages compared to other technologies.

- Controllable period: The period of multiple-beams laser interference depends on the wavelength and incident angles. Thus, an identical laser interference system enables to control the period from micrometre to nanometre theoretically by changing the incident angles. Figure 3.5 shows an example of two-beam interference generated grating structures control the period from micrometre to nanometre by changing the incident angles. Figure 3.6 shows the three-beam interference generated dot structures control the period. The period from micrometre to nanometre can be shown in the orders from (a) to (d) in Figures 3.5 and 3.6. With respect to other micro and nano fabrication technologies, such as chemical technologies and optical lithography, they are difficult to control the period as the researchers' desired. Additionally, EBL and FIB enable to adjust the

period flexibly but at the cost of proximity error.

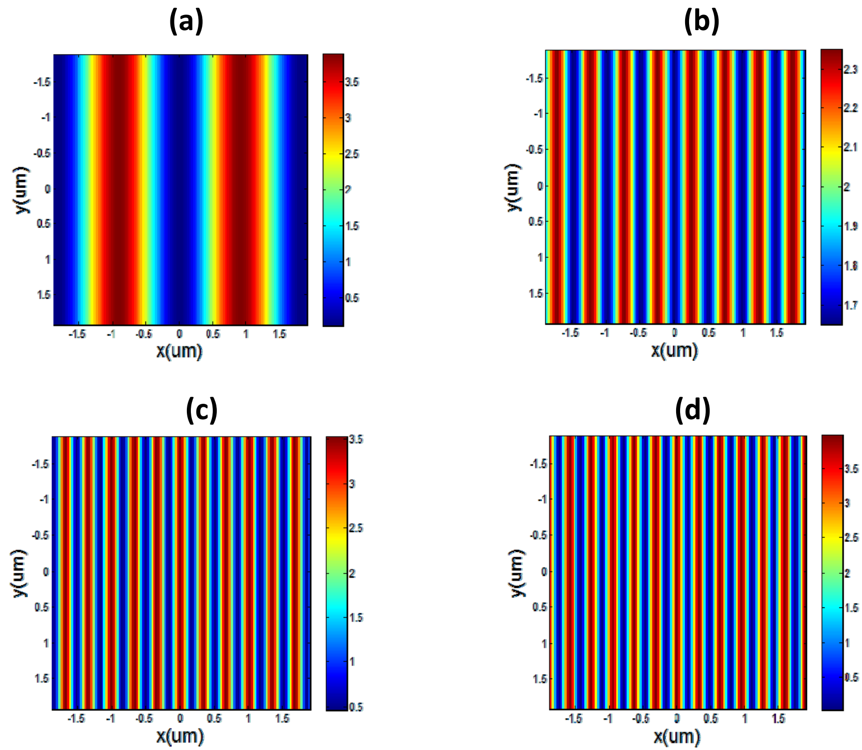

Figure 3.5 Schematic diagram of controllable period of two-beam laser interference from micrometre to nanometre for grating structures, (a) the incident angle is 10°, (b) the incident angle is 40°, (c) the incident angle is 70° and (d) the incident angle is 85°.

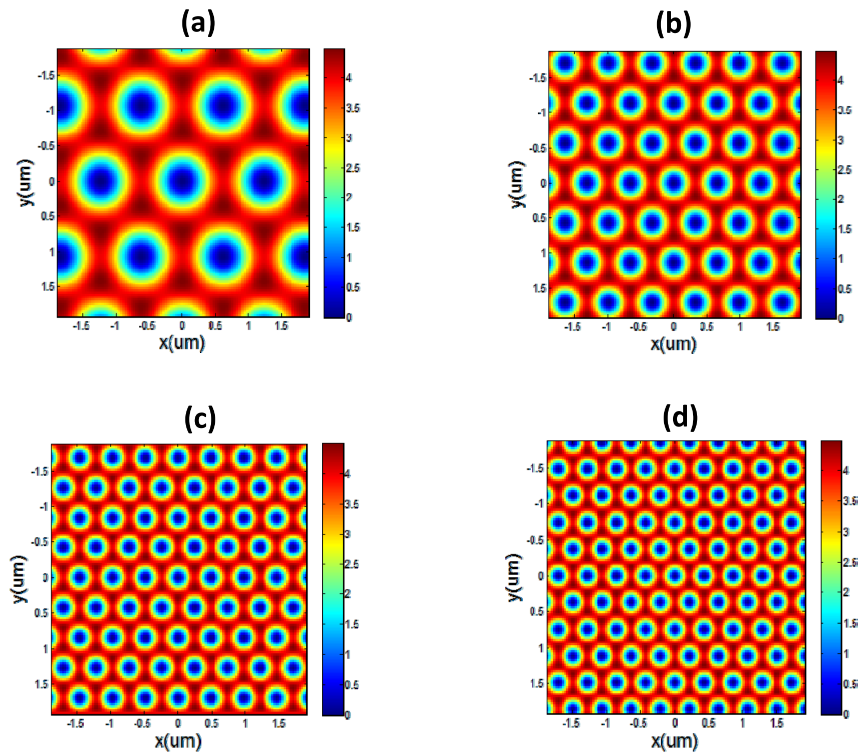

Figure 3.6 Schematic diagram of controllable period of three-beam laser interference from micrometre to nanometre for dot structures, (a) the incident angle is 20°, (b) the incident angle is 40°, (c) the incident angle is 60° and (d) the incident angle is 80°.

- Various patterns: For the interference patterning, various structures, which are square dot, grating, dual-periodic array, honeycomb array and flower-like have been produced by multiple-beams laser interference with different laser parameters which have a strong influence of the eventual pattern, such as incident angle, phase, wavelength, polarized angle, phase and number of interfering beams. The example of Figure 3.7 shows Matlab simulation of various interference patterning. For the flower-like interference patterning has been reported by Wang et al. [50]. These structures can apply to every where, such like antireflection, self-cleaning coats and various optical elements. Moreover, according to the bionic structures of lotus leaves, moth-eyes, butterfly colour and so on in the nature, a number of technologies have been excellently developed in the application area today.

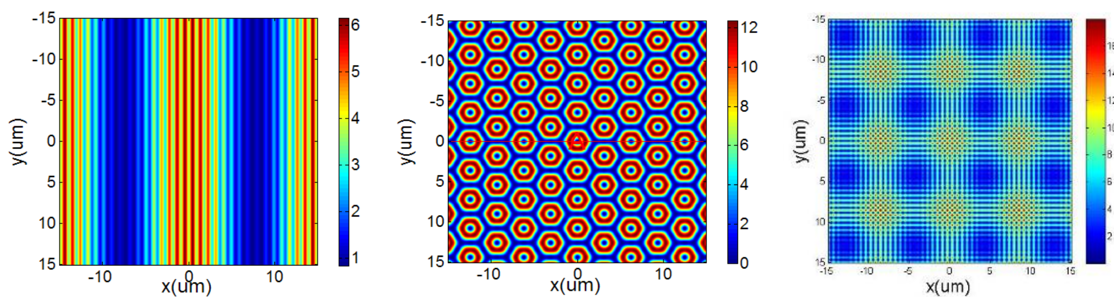

Figure 3.7 Matlab simulation of various interference patterning.

- Parallel fabrication: LIL simultaneously produces the periodic patterns on the beam area unlike EBL and FIB. Thus, the laser interference lithography technology has the capability of large-area fabrication and high efficiency.

3.2 Theory of Antireflection

Generation of electrical current in the solar cell is a result of interaction between the incident sunlight and semiconductor. There are the following three basic attributes in the necessary requirement of the operation of solar cells [9].

- “The absorption of light, generating either electron-hole pairs or excitons.
- The separation of charge carriers of opposite types.
- The separate extraction of those carriers to an external circuit”.

Sunlight is composed of photons with its energy corresponding to their wavelengths. The incident light on the solar cells surface can be separated into three parts: reflected photons, photons passing through the cell and absorbed photons. During the process of the generation of electrical current in the solar cells, the optical losses are the main reason for lowness of the photovoltaic conversion efficiency and it decreases solar cell performance. Optical losses mainly consist of the reflection of the part of incident light from the surface of solar cells. As a result, only smaller number of photons can generate electron–hole pairs. When the absorbed energy of photon is greater than the energy gap of the semiconductor, this semiconductor can contribute to the generation of electricity. Figure 3.8 shows the principles of the antireflection surface absorbing the sunlight [51]. Wherein, 1 is the flux of incident photons, 2 and 3 are the flux of reflected photons and 4 and 5 are the flux of absorbed photons.

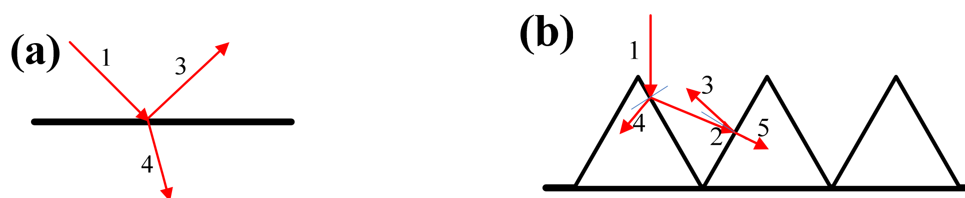

Figure 3.8 The principles of the antireflection structures absorbing the sunlight. (a) is the planar surface and (b) textured surface [51]. 1 is the flux of incident photons, 2 and 3 are the flux of reflected photons and 4 and 5 are the flux of absorbed photons.

From Figure 3.8 (a), when the flux of incident photons (1) reaches the flat surfaces, it only has one flux of absorbed photons into the material and other optic energy has been lost. To minimise the flux of reflected photons, surface texturing is accomplished, as shown in Figure 3.8 (b). Compared with the flat surfaces, the texturing surfaces have been increased the surface area because of the convex and concave structures. In this case it can increase the reflected photons path, and thus make the reflected photons to

bounce back to the surface again and obtain another light-trapping mechanism. Consequently, the probability of greater amount of incident light to be absorbed is increased through multiple internal reflections and refractions [52].

The antireflection structures have been defined to a short period, as shown in Equation (3.5) [1].

$$p < \frac{\lambda_0}{n_{air}\sin\theta_i\cos\phi + (n^2 - n_{air}^2\sin^2\phi)^{1/2}} \tag{3.5}$$

where P is the grating period, λ_0 is the vacuum wavelength, n_{air} is the air refractive index, n is the substrate material refractive index, θ_i is the polar angle of incidence light and ϕ is the azimuthal angle of incidence light.

The maximum period $P_{\max}$, when the incident light is perpendicular to the grating surface, allows only the propagation of the zero diffraction order as given by Equation (3.6)

$$p_{\max} = \frac{\lambda_0}{n} \tag{3.6}$$

It assumes that the light is incident normally on the top surface. According to the thin-film optics, as shown in Figure 3.9, the condition to achieve zero reflection is

$$n_{AR-film} = (n_1 n_2)^{1/2} \tag{3.7}$$

$$h = \lambda / 4n_{AR-film} \tag{3.8}$$

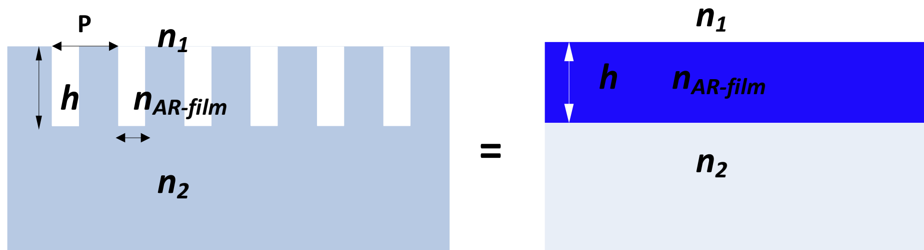

Figure 3.9 Sketch of an antireflection film.

where $n_{AR\text{-}film}$ is the refractive index of the media of the antireflection coating, h is the thickness of the coating, n_1 and n_2 are the refractive indices of the ambient and solid media ($n_1 \approx 1$ in air), respectively and λ is the wavelength.

The sub-wavelength structures are regarded as an anisotropic optical thin film having an effective refractive index as the period of structures is shorter than the wavelength of incident light. The effective refractive index (n_{eff}) can be expressed based on the effective medium theory.

$$n_{\mathrm{eff}} = (1-\sigma_n)^2 n_1 + \sigma_n^2 n_2 \tag{3.9}$$

$$\sigma_n = W_{\mathrm{n}} / P \tag{3.10}$$

where W_n is the width of structures and P is the period.

3.3 Theory of Self-cleaning

Superhydrophobic surfaces with a high static contact angle above 150° exhibit excellent repellence and self cleaning properties. The contact angle is formed by a liquid at the three phase contact line where the liquid, vapour and solid intersect. The drop shape is controlled by the three forces of interfacial tension shown in Figure 3.10. The contact angle is a quantitative measure of the wetting of a surface by a liquid.

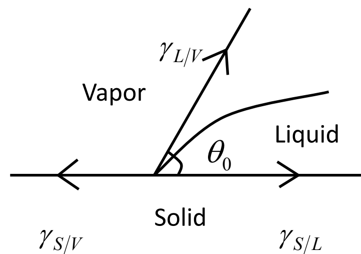

Figure 3.10 A liquid drop showing the quantities in Young equation.

There are three theoretical models for the wetting behaviour of a water droplet on the solid surface as shown in Figure 3.11. The Young model is valid in the case of a flat solid

surface. The Wenzel model is used in the case of a rough surface and the liquid is in the intimate contact with the solid. The Cassie–Baxter model works in the case of the liquid rests on the tops of the asperities [53].

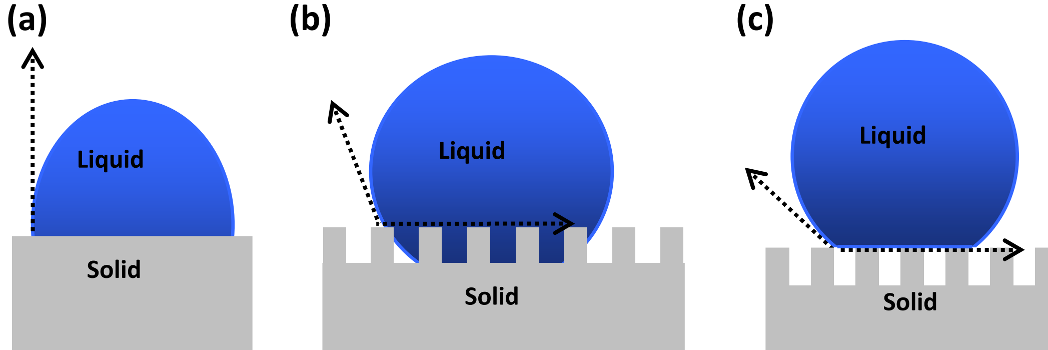

Figure 3.11 Models for the wetting behaviour of a water droplet on the solid surface; (a) is the Young model, (b) is the Wenzel model and (c) is the Cassie–Baxter model.

The Young model can be expressed as [53]

$$\cos\theta_0 = \frac{\gamma_{S/V} - \gamma_{S/L}}{\gamma_{L/V}} \tag{3.11}$$

where θ_0 is the contact angle, $\gamma_{S/V}$ is the interfacial tension between the solid and air, $\gamma_{S/L}$ is the interfacial tension between the solid and liquid, and $\gamma_{L/V}$ is the interfacial tension between the liquid and air.

The Wenzel model can be defined as [53]

$$\cos\theta = R_f \cos\theta_0 \tag{3.12}$$

where θ is the contact angle which corresponds to the stable equilibrium state, R_f is the roughness factor which is defined as the ratio of the solid-liquid area to its projection on a flat plane, and θ_0 is the contact angle of the Young model as defined for a perfect flat surface.

The Cassie–Baxter model can be written as [53]

$$\cos\theta = \psi_L \cos\theta_1 + \psi_A \cos\theta_2 \tag{3.13}$$

θ_1 and θ_2 are the contact angles of the flat solid and air surfaces, and ψ_L and ψ_A are the

solid and air surface area fractions of the solid and air. When the contact angle of the air film is 180° and $\psi_L + \psi_A = 1$, Equation (3.13) can be rewritten as

$$\cos\theta = \psi_L(\cos\theta_1 + 1) - 1 \tag{3.14}$$

It is known from Cassie-Baxter model that two criteria must be necessary to meet the condition of hydrophobicity: a contact line density criterion and asperity height criterion. The thickness of the air pocket has an effect on gathering the water droplet, and it is also related to the fraction that the solid area contacts the water drop [54].

3.4 Summary

In this chapter, the basic theory of laser inference lithography and principles of antireflection and self-cleaning have been introduced. Figure 3.12 shows a framework of the research methodology and the relationships between the chapters. They are revealed in views of the theoretical analyses of laser interference lithography, experimental simulations and the fabrication of antireflection and self-cleaning structures. This chapter has studied the principles of laser interference, antireflection and self-cleaning, being the basis of the fabrication of antireflection and self-cleaning structures on silicon wafer with regular micro and nano patterns. The structures are identified that can get better antireflection and self-cleaning properties and can be fabricated using laser intereference lithography. In Chapter 4, Matlab simulations of the micro and nano structures are conducted to attain the parameters for building the system of laser interference lithography. As discussed in the chapter, the advantages of laser interference lithography can be utilised to achieve various desired micro and nano structures. The parameters for building the system of laser interference can be obtained according to the simulations. Chapter 5 is to implement the classical theoretical analyses of laser interaction to substrate and obtain novel theoretical analysis of interference formation, knowing that parameters of laser, such as laser influence, laser pulses and laser repetition can also affect the shape of laser interference pattern. The chapter discusses the effect of heat transfer and plasma on silicon wafer using laser interference lithography with equations for the effect of heat

and plasma distribution. In Chapters 6, 7, and 8, suitable surfaces with both functions of antireflection and self-cleaning are fabricated with the study and application of these basic theories. Chapter 6 presents a novel triadic hierarchical structure on silicon wafer surfaces with good antireflection and hydrophobic properties. This triadic hierarchical structure is fabricated with three-beam laser interference in one step. Chapter 7 presents highly-ordered superhydrophobic micro and nano dual structures on silicon obtaining the contact angle of 153.2°, fabricated with direct laser interference lithography. Chapter 8 presents arrays of hexagonally-distributed hole structures fabricated by three-beam laser interference, providing a design guideline to achieve a considerably low solar-weighted reflectance (SWR) (1.86%) in the wavelength range of 300 nm to 780 nm and a relatively large contact angle (140°) with a strong self-cleaning capability on the solar cell surface.

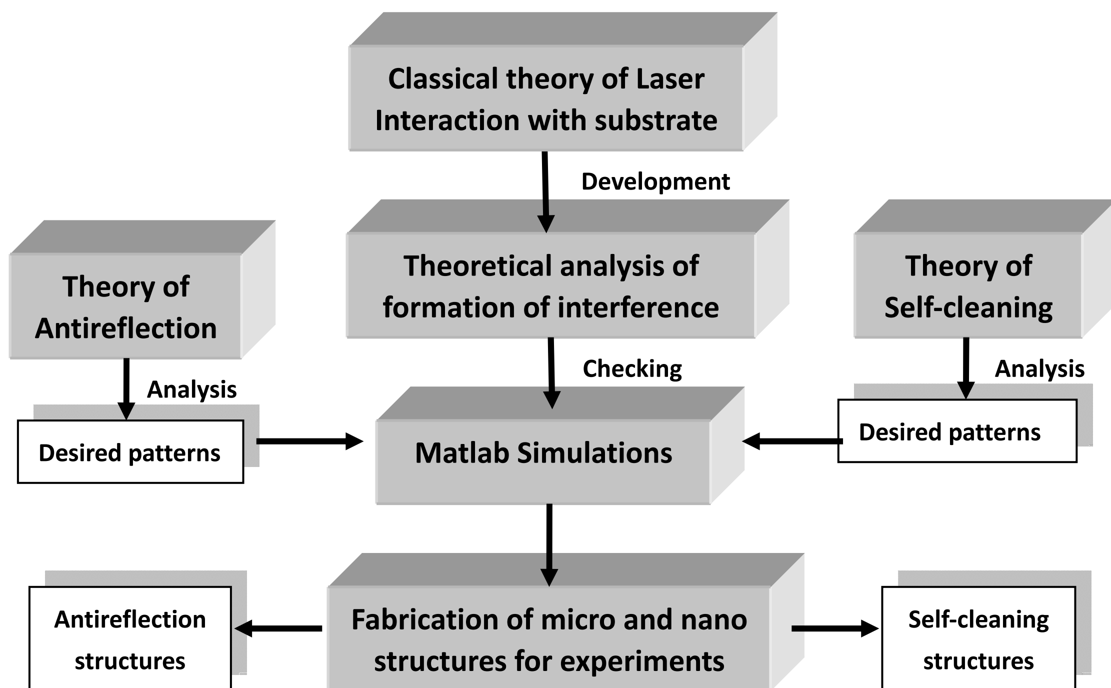

Figure 3.12 Framework for research methodology.

Chapter 4
Fabrication and Measurement

In this Chapter, the fabrication and measurement methods used in this work have been presented, in addition, the fabrication and measurement methods have supported part of the work and results in my published papers (***Appendix A [1]-[3] and [8]-[10]***). The first section discussed the fabrication process by laser interference lithography on the silicon wafer surface, the second part showed the measurements of reflection and contact angle for the texture silicon wafer surface.

4.1 Fabrication Process by Laser Interference Lithography

The methodology is represented in the state diagram at Figure 4.1 and divided in four steps as described below.

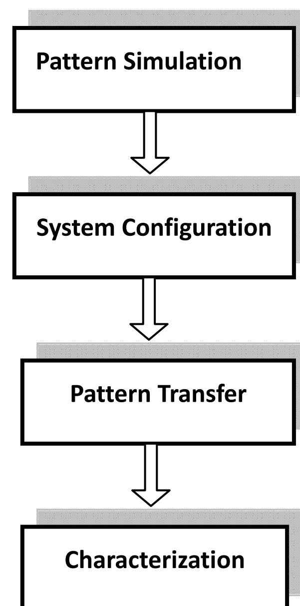

Figure 4.1 State diagram of the fabrication process.

- **Pattern simulation:** A simulation program can reproduce different beam arrangements until the desired pattern is fabricated. This simulation software can simulate the periodic structures of laser interference before manufacturing. The

procedure is represented in a flow diagram at Figure 4.2. Through this simulation software, different beam arrangements can repeatedly simulate until the desired pattern is obtained. The main parameters selected by the user include the angle of incidence, azimuth angle, amplitude, polarization and wavelength. These simulation parameters are partly explained as follows.

- Angle of incidence: definition as the angle between the beam and the axis of the mechanical system.
- Azimuth angle: definition as the angle between the electric field vector (E) and the vector normal to the propagation direction.
- Intensity: representation the relative intensity of the values and not an absolute value. It is considered that all beams have the same intensity and set to 1.

☐ **System configuration**: According to the variables of system configuration, the number of the required beams, orientation and distance, the system must be configured to the desired configuration. Firstly the system has to be explained by two modules, which are laser system and beam generation module, and interference control and substrate positioning module.

- Laser system and beam generation module: The laser interference system uses seeded Q-switched Nd:YAG laser source and a beam multipolariser system based on beamsplitters to implement the first module of the optical layout. Table 4.1 shows the laser source parameters selected for the fabrication process. The energy control is performed with a 1/4 wave plate and a polarizer, as shown in Figure 4.3. When a linear polarized laser beam that emits from the laser passes through a 1/4 wave plate, the polarization direction will turn into circular or elliptical polarization determined by the angle of intersection. Then rotating a polarizer behind the 1⁄4 wave plate can control the final linear polarization direction. By using 1⁄4 wave plates and polarisers can obtain arbitrary polarization combination with the same pulse energy of each incident beams of multiple-beam interference, and rotating the 1⁄4 wave plates can also modify the output energy of each beam.

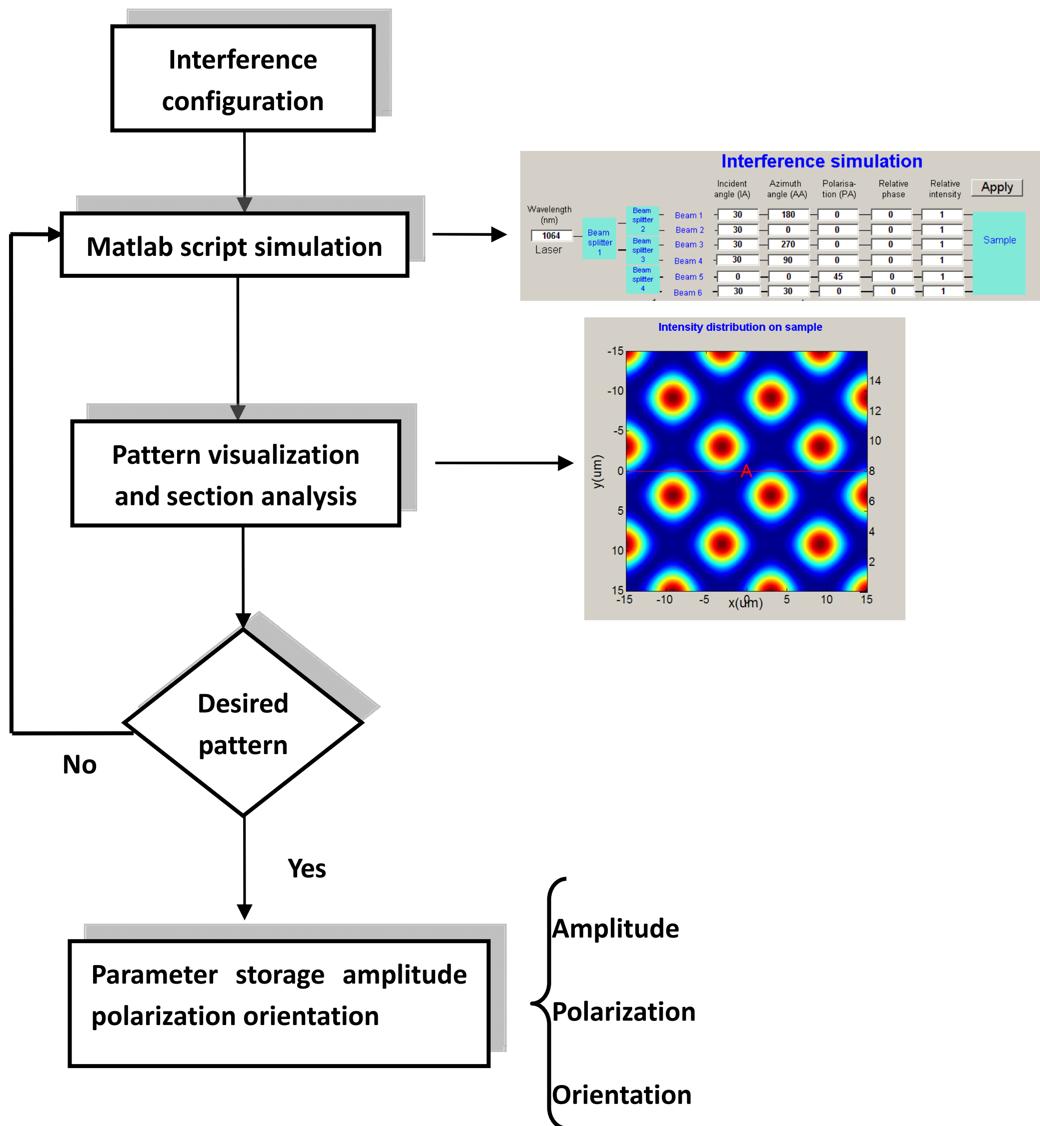

Figure 4.2 Flow diagram of the simulation code. Two screenshots of the interference simulation tool are displayed. The first one is the introduction of main parameters and the second is simulation pattern of corresponding intensity distribution.

Table 4.1 Specifications of the laser source selected for the fabrication process

Laser source parameters	
Wavelength	213, 266, 355, 532 and 1064
Pulse duration	7ns-9ns
Pulse repetition rate	Up to 10Hz
Beam diameter	6mm
Beam spatial profile	Gaussian

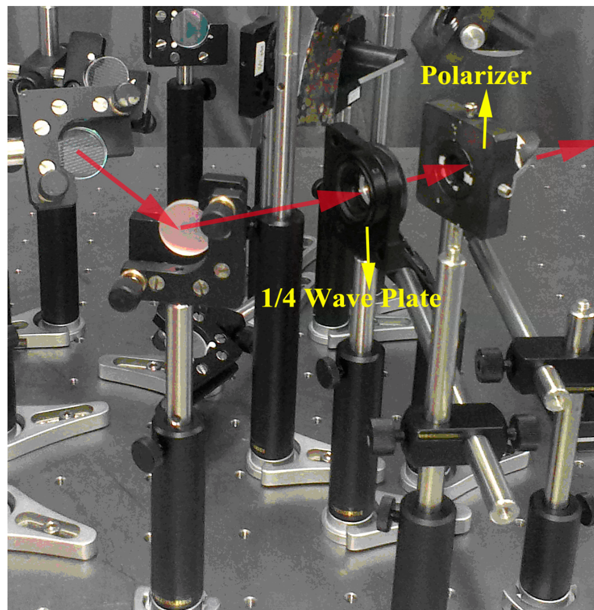

Figure 4.3 Implementation of the optical design for energy control.

- Interference control and substrate positioning module: the main function of this part is that it can control the parameters of the interference system to obtain the desired interference pattern including the feature size, period, pattern shape and size.

- Pattern transfer: the material can be located at the interfered point and irradiated by interfering beams. After the building of system, this laser interference lithography system can fabricate the desired patterns either by a direct-write process onto the material or by an indirect process through an intermediate step or phtoresist. Figure 4.4 shows the typical flow charts of indirect and direct processes. In this work, direct-write processes onto the silicon wafer surface are used.
- **Characterization:** Finally, the samples are observed and analyzed by different characterization techniques. The structural characterization is made by optical microscopy, scanning electron microscopy and atomic force microscopy.

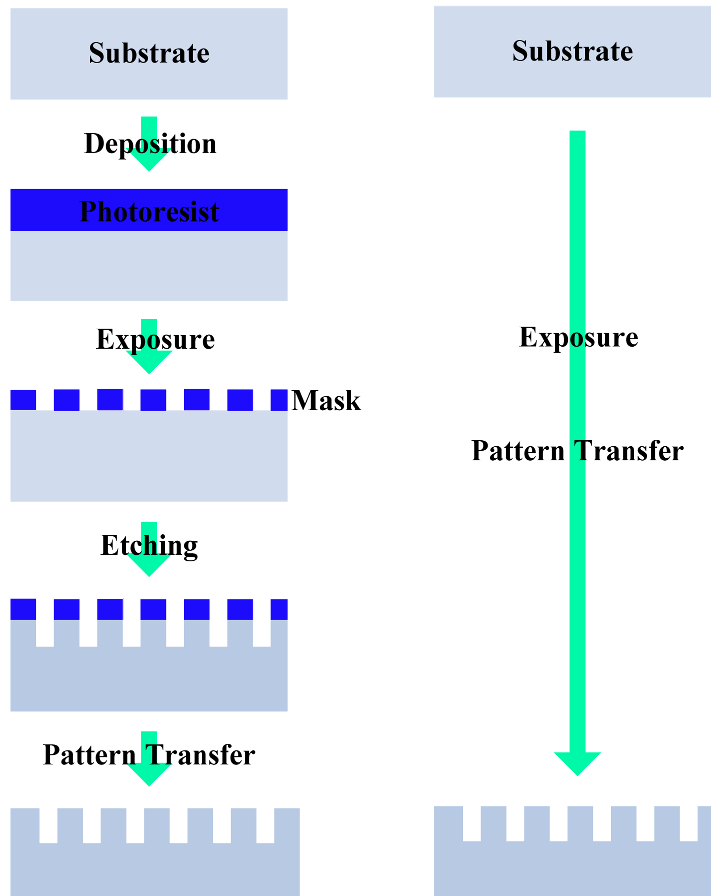

Figure 4.4 Typical flow charts of indirect and direct processes.

- A scanning electron microscope (SEM) is an important high resolution electron microscope. It is used high-energy beam of electrons in a raster scan structure and display image. The system FEI Quanta™ 250 in the lab is used to evaluate the detail of the patterns in the laser spot and compared different conditional structures generated by laser interference.

- Atomic force microscopy (AFM) or scanning force microscopy (SFM) is a mainly scanning probe microscopy with high resolution, and having demonstrated resolution about fractions of a nanometre, more than 1000 times better than the limit of optical diffraction. The measurements were performed by Atomic Force Microscope System of CSPM5500 as shown in Figure 4.6. It can provide a surface topography analysis of the silicon surface structures, and thus allows analyzing the depth and width of the patterned features.

Figure 4.5 Scanning Electron Microscopy (SEM) of the FEI Quanta™ 250 in our lab.

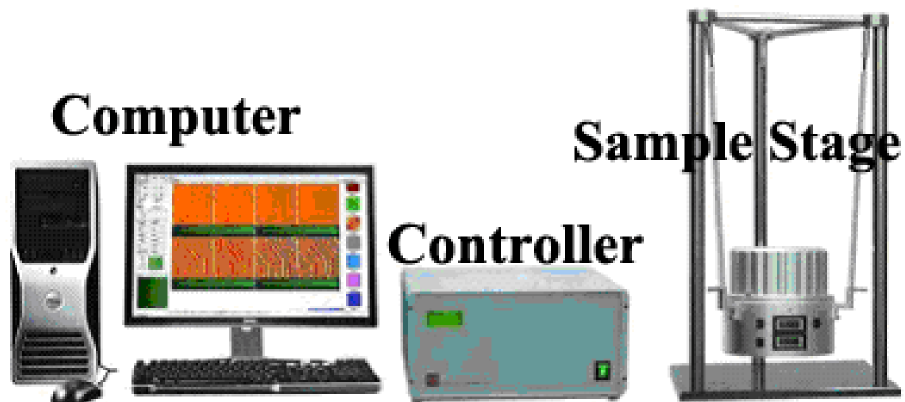

Figure 4.6 Atomic Force Microscope System of CSPM5500 in our lab.

- Optical microscopy is a type of microscopewhich uses visible light and a system of lenses to magnify images of small samples. It is very simple and can be used to adjust the light path for laser interference system. Moverover, the optical microscopy also can observe the whole structures of large area silicon surface fabricated by laser interference. Figure 4.7 shows the optical microscopy system used in this research.

4.2 Systems and Patterns of Multiple-Beam Laser Interference

In order to fabricated micro and nano structures by laser interference system, different architectures for the systems have been implemented. If a two-beam laser interference system is used, the system of two-beam interference can generate 1D structure, such as gratings. If multiple-beam laser interference system impacts on the sample surface, it can create 2D periodic structures can also produce 3D periodic structures. Thus, the arrangements of multiple-beam laser interference systems, which are more beams (three or more) to generate the interference pattern, increase the flexibility of the technique and the complexity of the patterns that can be achieved. In the following sections, the two-beam, three-beam and four-beam laser interference systems are introduced.

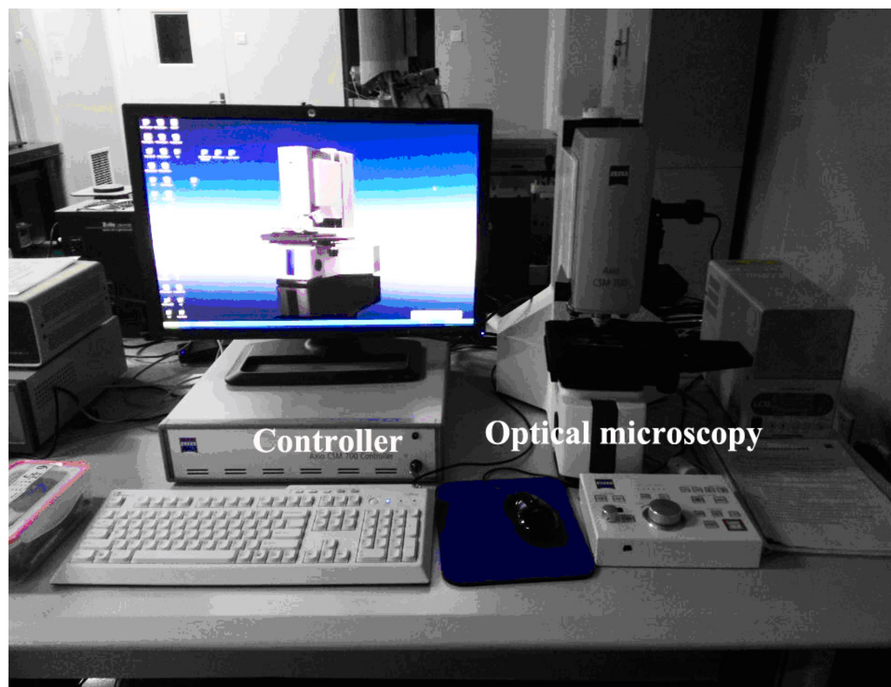

Figure 4.7 Optical microscopy used in this research.

4.2.1 Two-beam Laser Interference

Two-beam laser interference is widely used for the generation of 1D grating. This method has been used in my published paper, titled "Silicon wafer modification by laser interference"[55]. Figure 4.8 illustrates the schematic diagram of two-beam laser

interference lithography. Figure 4.9 shows the real system of two-beam laser interference lithography. The theoretical equations of two-beam laser interference intensity distributions are derived on a basis of the methodology describing the electric field vectors in Chapter 3 and expressed as Equation (3.1). Using the Matlab simulation software, the distribution of the two-beam interference patterns with 2D and 3D profiles can be obtained as shown in Figure 4.10 (a) and (b). This simulation example of 2D and 3D profiles illustrates that the incident angle is 30°, the wavelength is 1064 nm, the azimuthal angels are 0° and 180°, and the polarized angles are 0° and 0° as shown in Table 4.1. The intensity distributions equation is shown as

$$I_{2\text{-beam}} = 2I_0[1 + \cos(2kx \sin\theta)] \tag{4.1}$$

Using the tow-beam laser interference technology can construct 2D periodic structures. Initially, a 1D grating is created on a material and then changing 90°of the material is irradiated again. Figure 4.11 shows the schematic diagram of tow-beam and double exposure laser interference process. Normally double exposure of the sample results in a 2D square or hexagonal structure, although this process can be repeated as many times as the desired pattern requires. Figure 4.12 shows a simulation of the resulting pattern of double exposure process. Multiple-exposure laser interference is commonly used over a positive or negative photoresist and obtain various flower-like structures [50].

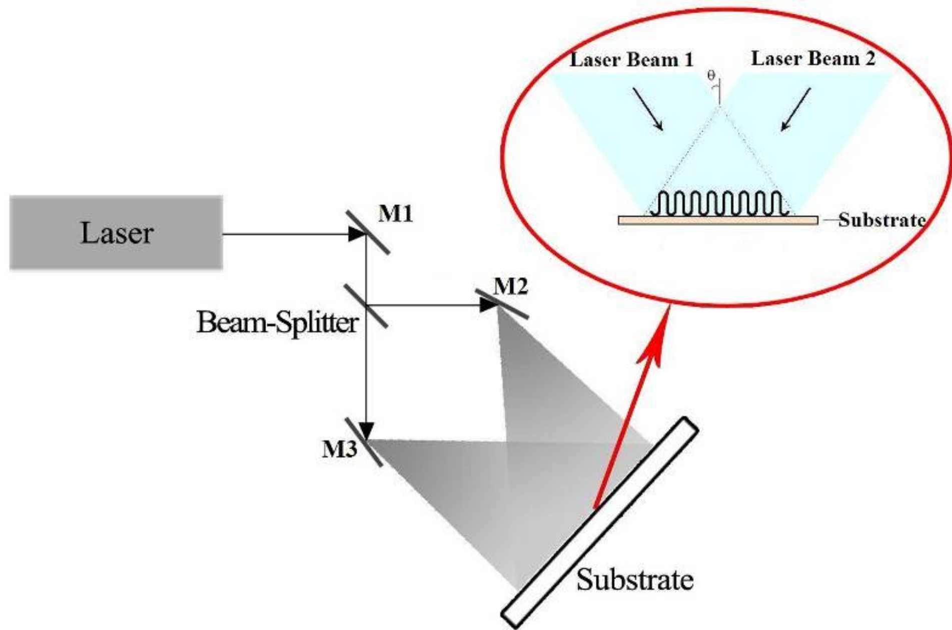

Figure 4.8 Schematic diagram of two-beam laser interference lithography.

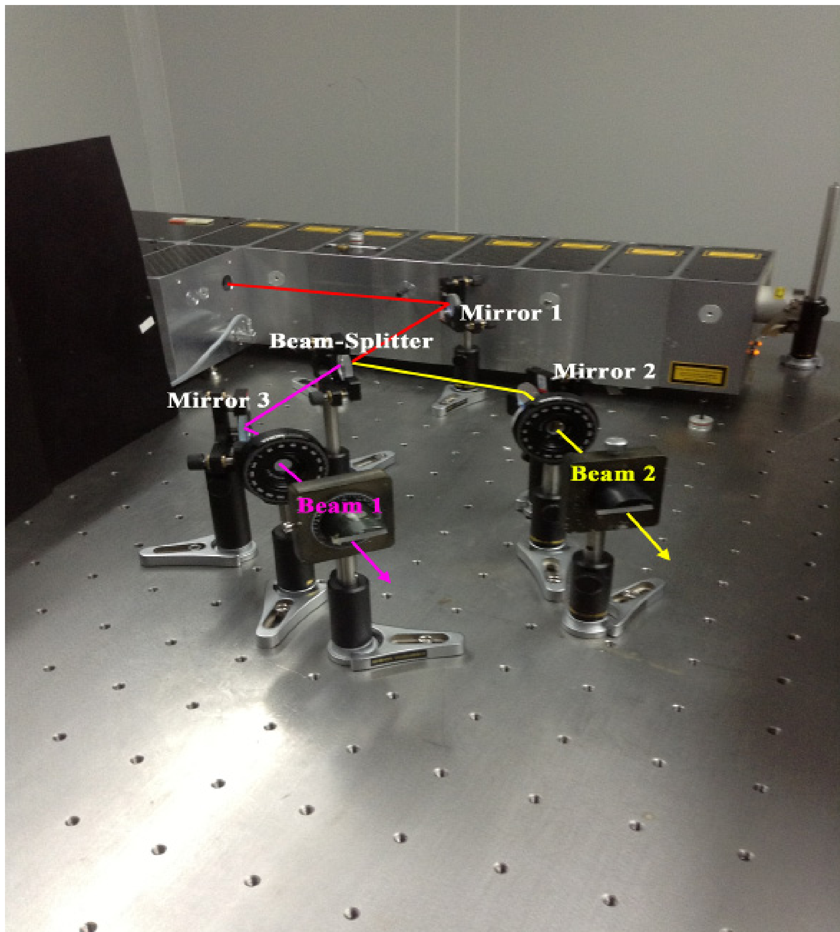

Figure 4.9 System of two-beam laser interference lithography.

Table 4.2 Matlab simulation of beam configuration parameters of grating structure.

Parameter	Beam 1	Beam 2
Angle of Incidence	30°	30°
Azimuth	0°	180°
Polarization	0°	0°
Relative Intensity	1	1

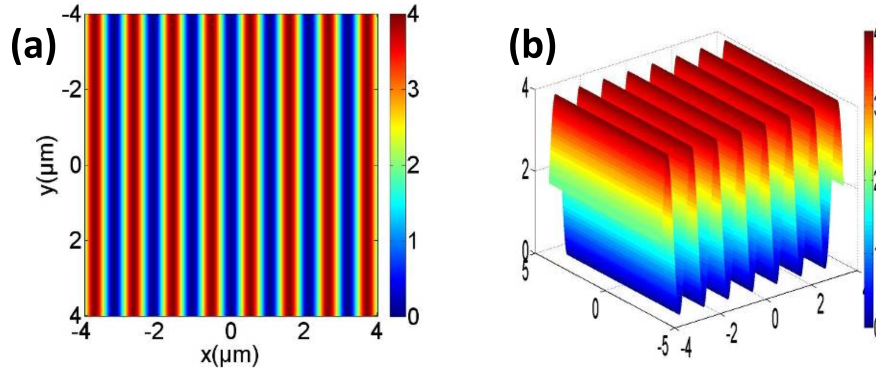

Figure 4.10 Multi-beam interference simulations, (a) is 2D intensity distribution for two-beam interference and (b) is 3D intensity distribution for two-beam interference ($\lambda = 1064\,nm, \theta = 30°$).

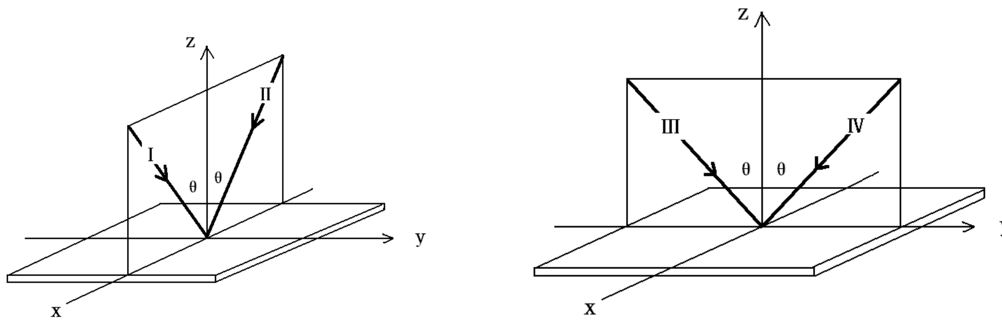

Figure 4.11 The schematic diagram of tow-beam and double exposure laser interference process.

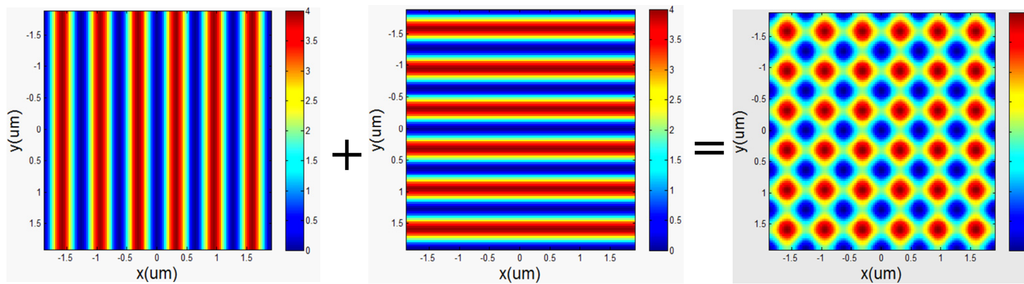

Figure 4.12 A simulation of the resulting pattern of the double exposure process.

4.2.2 Multiple-beam Laser Interference

4.2.2.1 Three-beam Laser Interference

For three-beam laser interference, it can generate the gratings and dots periodic patterns as well with hexagonal geometries and the periods proportional to $\lambda / \sin\theta$, when three beams are placed symmetrically at 120° around the central axis with the same incidence angle. Such resultant hexagonal structure has a lattice constant, which is $a = b = 2\lambda / 3\sin(\theta)$. This method has been used in my published paper, titled "Antireflection silicon structures with hydrophobic property fabricated by three-beam laser interference" [56]. This kind of hexagonal structure should be taken into account because it has symmetry of the interference pattern and it affects optical and hydrophobic properties. Figures 4.13 and 4.14 show the schematic diagram and the system setup of three-beam laser interference lithography. The intensity distributions equation has shown as

$$I_{3b} = I_0\{3 + 2\cos(2kx\sin\theta) + 2\cos[2k(\frac{x}{2} + \frac{\sqrt{3}y}{2})\sin\theta] + 2\cos[2k(\frac{x}{2} - \frac{\sqrt{3}y}{2})\sin\theta]\} \tag{4.2}$$

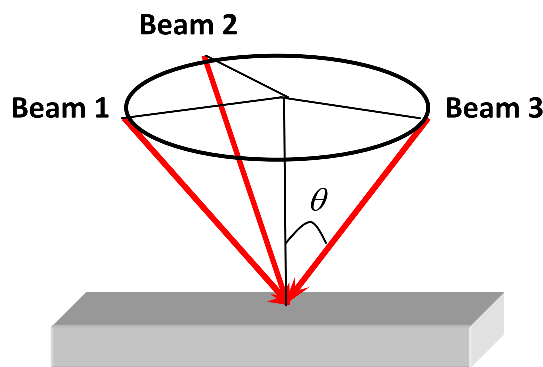

Figure 4.13 The schematic diagram of three-beam laser interference lithography.

The conditions of Matlab simulation of three-beam are that the same incident angles are 30°, the wavelength is 1064 nm, the azimuthal angels are 0°, 120° and 240°, and the polarized angles are 90°, 90° and 0° as shown in Table 4.3. This kind of interference of

three non-coplanar beams can generate 2D period patterns with hexagonal geometries. The hexagonal geometries pattern has excellent antireflection and hydrophobic properties as discussed in the Chapter 9. Furthermore, the three-beam laser interference is not the only to produce this kind of 2D period dots, but also fabricate the gratings. The conditions of Matlab simulation are that incident angles are 35°, 35° and 40°, the wavelength is 1064 nm, the azimuthal angels are 180°, 0° and 180°, and the polarized angles are 0°, 0° and 0° as shown in Table 4.4. This kind of grating is dual-periodic gratings distinguished from two-beam laser interference and has very important significance for various applications. Using the Matlab simulation software, the distributions of the three-beam interference patterns with 2D and 3D profiles can be obtained as shown in Figure 4.15(a) and (b).

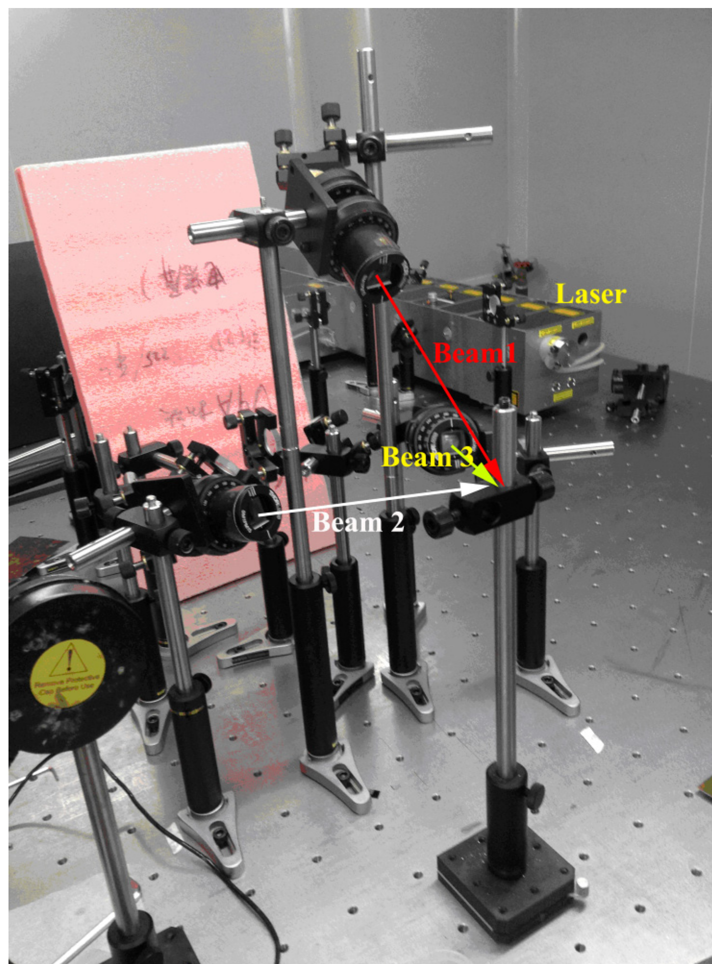

Figure 4.14 The system setup of three-beam laser interference lithography

Table 4.3 Matlab simulation of beam configuration parameters of hexagonal patterning by three-beam laser interference.

Parameter	Beam 1	Beam 2	Beam 3
Angle of Incidence	30°	30°	30°
Azimuth	0°	120°	240°
Polarization	90°	90°	0°
Relative Intensity	1	1	1

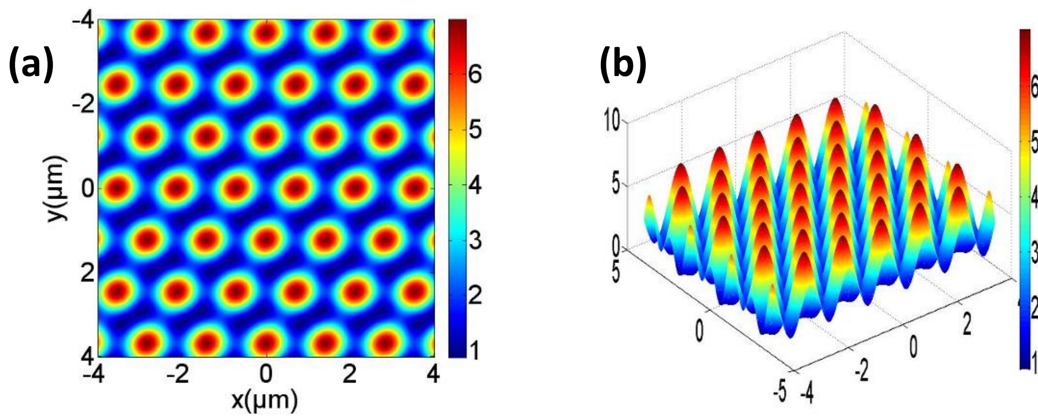

Figure 4.15 (a) is 2D intensity distribution with hexagonal geometries for three-beam interference and (b) is 3D intensity distribution with hexagonal geometries for three-beam interference.

Table 4.4 Matlab simulation of beam configuration parameters of dual-periodic gratings by three-beam laser interference.

Parameter	Beam 1	Beam 2	Beam 3
Angle of Incidence	35°	35°	40°
Azimuth	180°	0°	180°
Polarization	0°	0°	0°
Relative Intensity	1	1	1

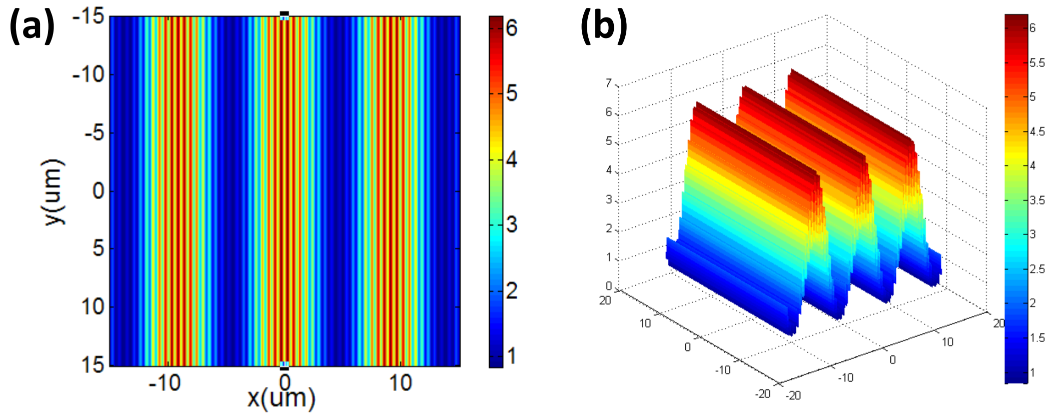

Figure 4.16 (a) is 2D intensity distribution with dual-periodic gratings for three-beam interference and (b) is 3D intensity distribution with dual-periodic gratings for three-beam interference.

4.2.2.2 Four-beam Laser Interference

For four-beam laser interference, the shape and geometry of the interference patterns are more complex than in the case of a three-beam configuration. "It was found that the secondary periodicity or modulation in four-beam laser interference was the result of the misalignment of incident angles or unequal incident angles" [57]. Figures 4.17 and 4.18 illustrate the schematic diagram and the real system of four-beam laser interference lithography. The conditions of Matlab simulation are that the same incident angles are 30°, the wavelength is 1064, the azimuthal angels are 0°, 90°, 180° and 270°, and the polarized angles are 90°, 90°, 90° and 90° as shown in Table 4.5. Figure 4.19 shows the Matlab simulation of four-beam laser interference. This method has been used in my published papers, titled "Effects of laser fluence on silicon modification by Four-beam Laser Interference" [58]; and "Effect of pulse repetition rate on silicon wafer modification by four-beam laser interference[59]". The intensity distributions equation of four-beam is shown as:

$$I_{4-beam} = 2I_0\{2 + \cos(2kx\sin\theta) + \cos(2ky\sin\theta) + 2\cos[k(x-y)\sin\theta] + 2\cos[k(x+y)\sin\theta]\} \tag{4.3}$$

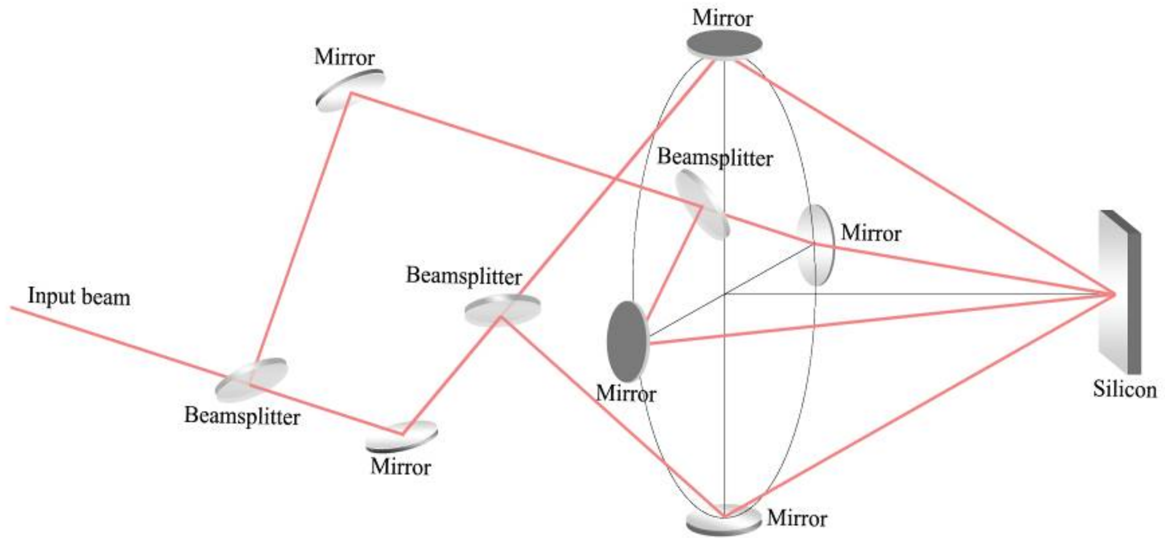

Figure 4.17 Four-beam laser interference diagram.

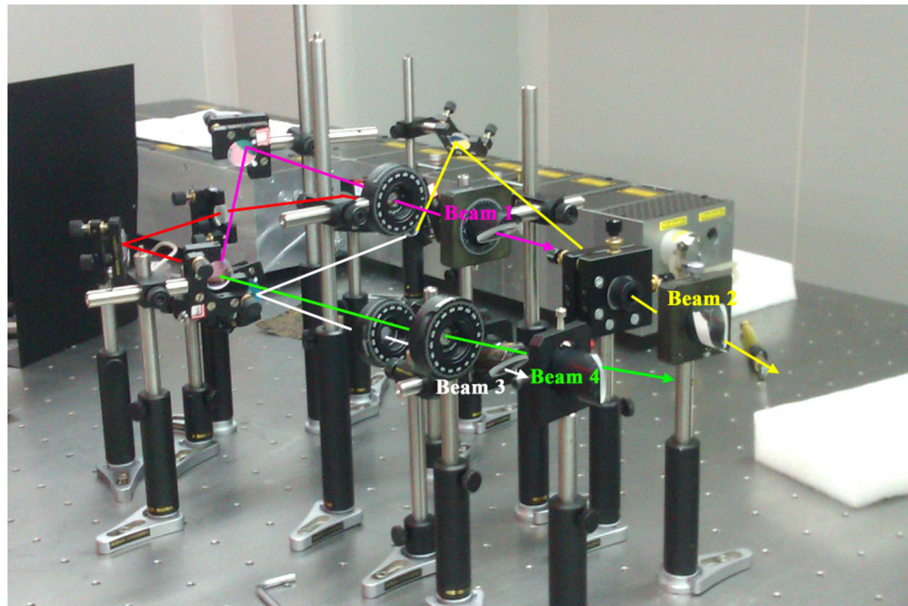

Figure 4.18 System of four-beam laser interference lithography.

Table 4.5 Matlab simulation of beam configuration parameters of square dots patterning by four-beam laser interference.

Parameter	Beam 1	Beam 2	Beam 3	Beam 4
Angle of Incidence	30°	30°	30°	30°
Azimuth	0°	90°	180°	270°
Polarization	90°	90°	90°	90°
Relative Intensity	1	1	1	1

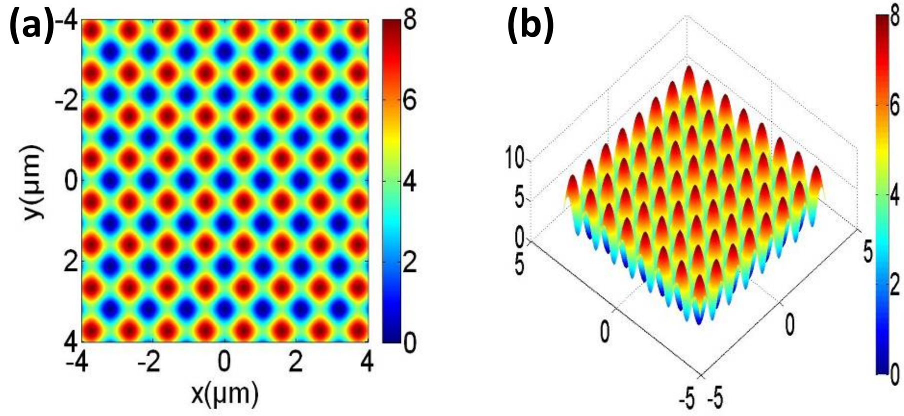

Figure 4.19 (a) is 2D intensity distribution for four-beam interference and (b) is 3D intensity distribution for four-beam interference ($\lambda = 1064\,nm, \theta = 30°$).

4.3 Fabrication of Interference Patterns

In order to prove the theoretical simulation is correct, it is demonstrated that grating pattern is fabricated by the two-beam interference, hexagonal array pattern is fabricated by the three-beam interference, and square array pattern is fabricated by the four-beam interference. Figure 4.20 shows the grating pattern generated by two-beam interference on the silicon wafer surface. The initial laser beam is divided into two beams with the azimuthal angles of $\varphi_1 = 0°$, $\varphi_2 = 180°$, $\vec{p}_1 = \vec{p}_2 = 90°$ and the incident angles of $\theta_1 = \theta_2 = 4°$, as shown in Table 4.6. The laser fluence is 560 mJ/cm^2 used for a good feature patterning.

Table 4.6 Beam configuration parameters of grating structure.

Parameter	Beam 1	Beam 2
Angle of Incidence	4°	4°
Azimuth	0°	180°
Polarization	90°	90°

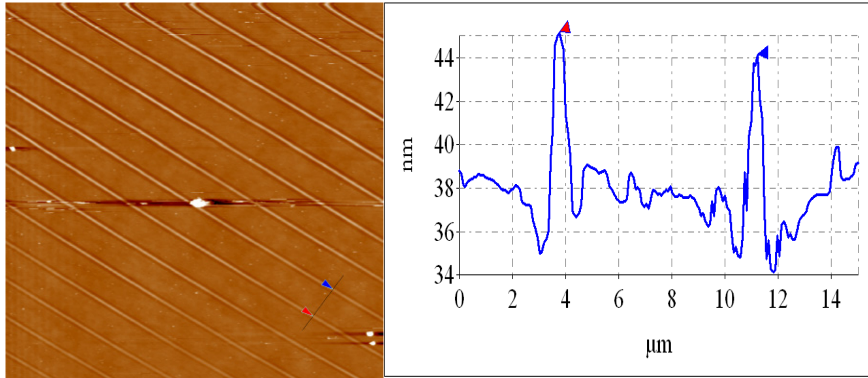

Figure 4.20 The grating pattern generated by two-beam interference on the silicon wafer surface and its cross section.

Figure 4.21 shows the hexagonal array pattern generated by three-beam interference on the silicon wafer surface with the laser fluence is 560 mJ/cm^2 and the laser parameters are shown in Table 4.7.

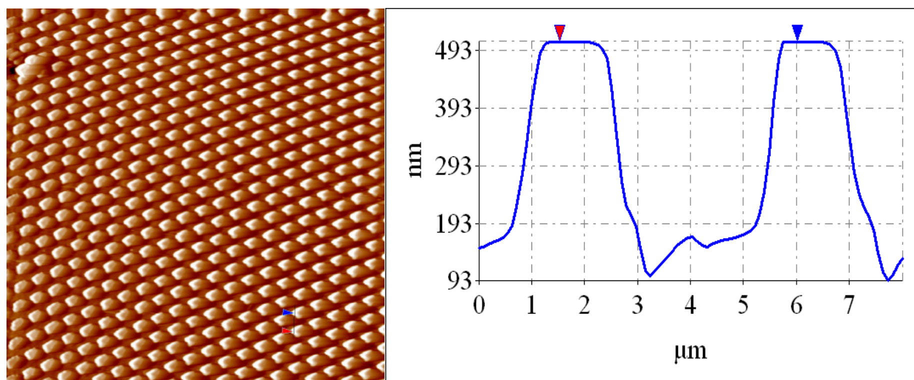

Figure 4.21 The hexagonal array pattern generated by three-beam interference on the silicon wafer surface and its cross section.

Table 4.7 Beam configuration parameters of grating structure.

Parameter	Beam 1	Beam 2	Beam 3
Angle of Incidence	6.8°	6.8°	6.8°
Azimuth	0°	120°	240°
Polarization	90°	90°	0°

Figure 4.22 shows the square array pattern generated by four-beam interference on the silicon wafer surface with the laser fluence is 560 mJ/cm^2 and the laser parameters are shown in Table 4.8.

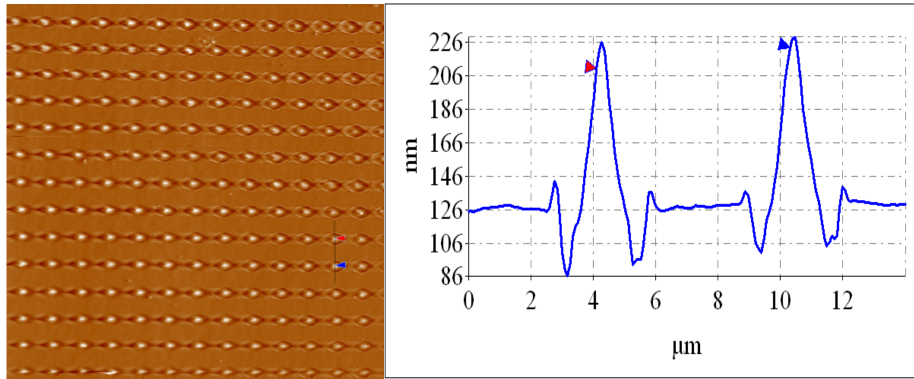

Figure 4.22 The square array pattern generated by four-beam interference on the silicon wafer surface and its cross section.

Table 4.8 Beam configuration parameters of square array pattern.

Parameter	Beam 1	Beam 2	Beam 3	Beam 4
Angle of Incidence	5°	5°	5°	5°
Azimuth	0°	90°	180°	270°
Polarization	90°	90°	90°	90°

Multiple-exposure laser interference is commonly used over a positive or negative photoresist. Figures 23 shows the 2D and 3D results of 2D structures by tow-beam and double exposure laser interference process. This result has obtained by the method tow-beam and double exposure laser interference process on the silicon surface covering photoresist of AZ5214.

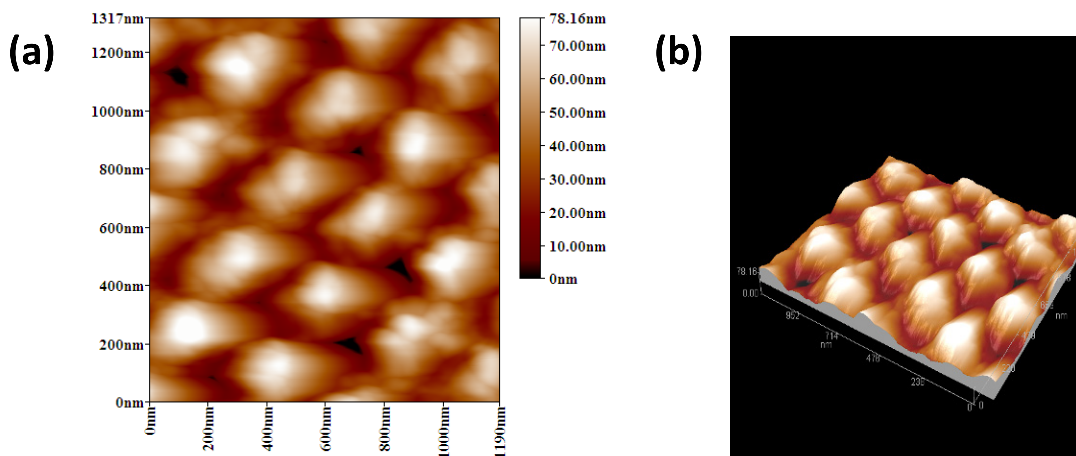

Figure 4.23 AFM images of tow-beam and double exposure laser interference pattern, (a) is 2D image and (b) is 3D image.

Figure 4.24 shows SEM image of dual-periodic gratings fabricated by three-bean laser

interference on silicon wafer surface.

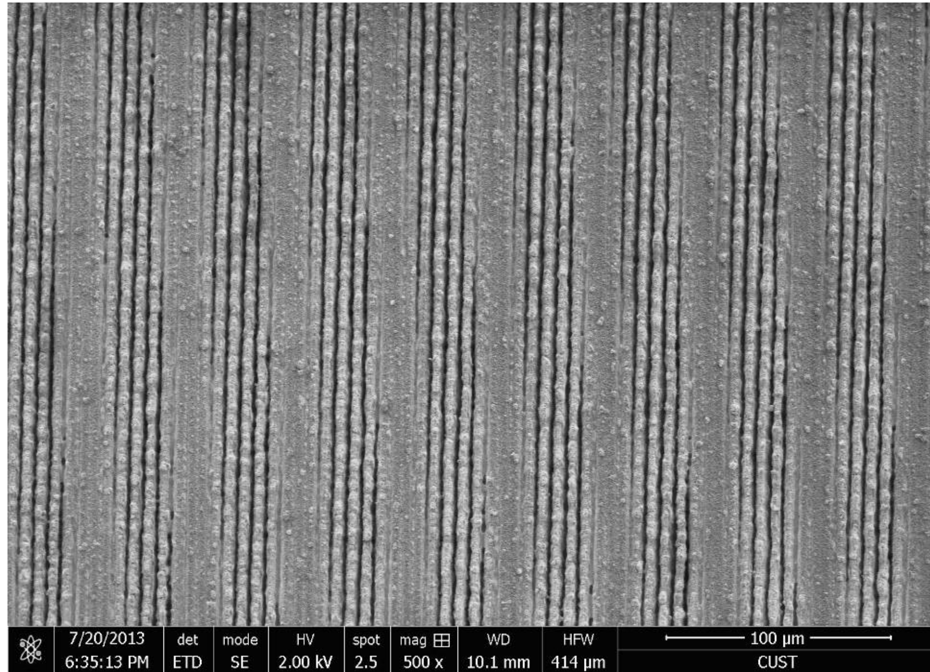

Figure 4.24 SEM image of dual-periodic gratings fabricated by three-bean laser interference on silicon wafer surface.

Therefore, the formation of interference patterns exhibits a large variation as the investigation of parameters, which are wavelengths, incident angles, azimuthal angles, polarized angles and relative phases,. Herein, the resulting patterns have shown a good correspondence with the theoretical analysis and simulations. However, except these parameters, the threshold of materials as another factor can affect and modify the surface morphology of materials, which is discussed in the next section.

4.4 Measurements System

As shown in Figures 4.25 and 4.26, the system uses a 150 W Xenon-lamp as light source which has a similar spectral distribution to sunlight. Firstly, incidence light is divided into specific wavelengths by Monochromator, then through the integrating sphere, the light turns to be homogeneous and transfers to the standard reflector. Finally, the detector of the electrochemical workstation gets the light from the integrating sphere and transforms it into the electrical signal which can be analyzed by this equipment.

The result is the value of current I1 from the electrochemical workstation as shown in Figure 4.27(a). Similarly, we obtain the value of current I2 by changing the standard reflector to a solar cell sample as shown in Figure 4.27(b). The reflective value of the standard reflector is known (Rs), and it can get the reflectivity of the measured samples (Rr) through Equation

$$R_r = (I_2 / I_1) \times R_s \tag{4.4}$$

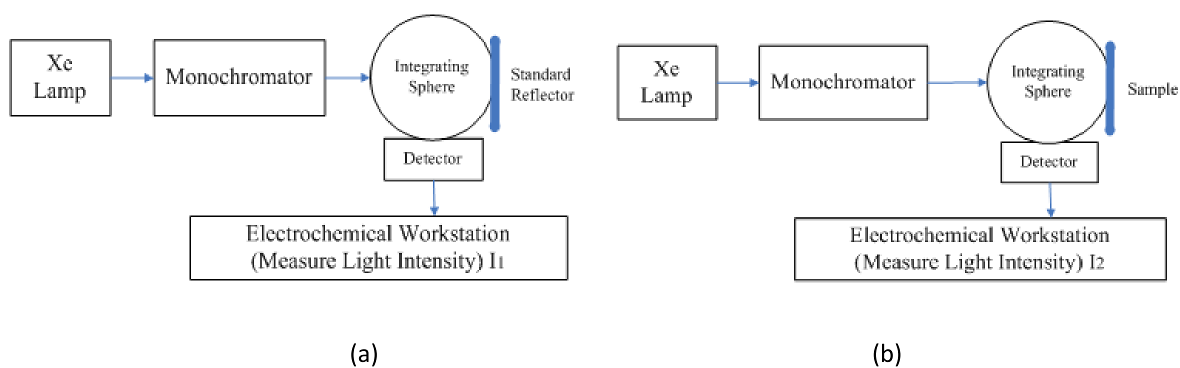

(a) (b)

Figure 4.25 Principle of antireflection measurement.

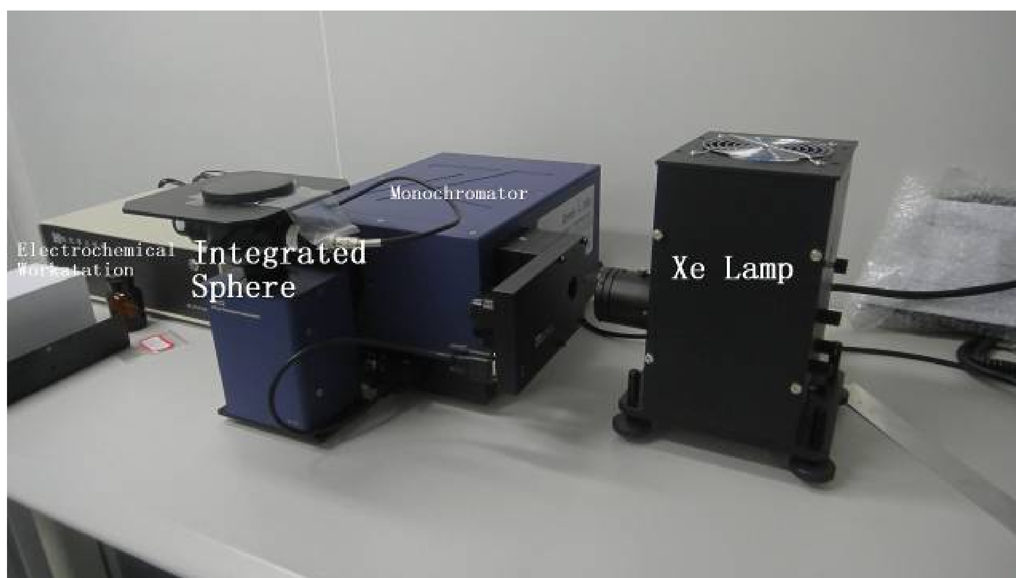

Figure 4.26 Real system for reflection measurement.

In addition, Table 4.9 lists the main specifications of spectrometer and electrochemical workstation to use in the experiment.

Table 4.9 Main specifications of spectrometer and electrochemical workstation.

Spectrometer	Specifications	Electrochemical workstation	Specifications
Focal length	300 mm	Pulse width of CA/CC	0.0001 to 1000 s
Resolution	0.1 nm	Min sampling interval of CA/CC	1us
Accuracy	0.2 nm (1200g/mm grating)	Pulse width of DPV/NPV	0.001 to 10 s
Repeatability	0.1 nm	SWV frequency	1 to 100 kHz
Wavelength Range (nm)	200-2500 nm	i-t min sampling interval	1 us

Analysis of the image of the liquid drop on the surface with the nano-micro structures can obtain the contact angle. The system includes a light source, image acquisition system and optic system. Figure 4.27 is the real system for self-cleaning measurement.

Figure 4.27 System for contact angle (CA) measurement

Chapter 5
Laser Interference Interaction with Silicon Wafers

In this chapter, firstly the introduction of laser process interaction with silicon wafers has been presented in Section 5.1. The theoretical analysis of Laser interaction with silicon wafer has been given by the second part. And then, different micro and nano structures, which are the shapes of gratings, holes and cones, have been fabricated by laser interference lithography on the silicon wafer surfaces in the air. The equations of heat flow and radiation effects of laser plasma of interfering patterns in a four-beam laser interference distribution are proposed to describe their laser radiation impacts on silicon wafer surfaces. In this Chapter, two-beam laser interference and four-beam laser interference as representatives have been discussed in the laser interference process interaction with silicon wafers. The findings have been published in my conference paper and journal paper, as show in ***Appendix A([2]-[3] and [8])***.

5.1 Introduction

Silicon is the basic and important semiconductor material for optical and electronic devices, and the laser processing of silicon wafers is widely used in the fabrication of ICs, processors, memories, sensors and solar cells. Thus, laser interactions with silicon surfaces have been extensively studied and attracted more interest in recent years.

Focused laser processing was widely used for the texturization of silicon surfaces for the fabrication of solar cells, and the black silicon with superior absorption property was demonstrated [22]. Many investigations have been devoted to the processes induced by direct femtosecond (fs), picosecond (ps) and nanosecond (ns) laser processing to produce silicon surface textures for decades [60, 61]. The results are dependent on the laser beam parameters (such as the energy density, pulse duration, wavelength and

pulse repetition rate), and the number of exposure pulses or interaction time and material modification threshold [62, 63]. The defined structures with special features such as ripples and columns can be created with proper selections of the above parameters [63, 64]. The physical phenomena of amorphization, melting, re-crystallization, nucleated vaporization and ablation were observed during a whole laser processing cycle [63]. A number of approaches have been made to study the interaction mechanism between focused laser beams and semiconductor materials. Wang et al investigated the damage thresholds on single-crystals induced by millisecond, nanosecond and picosecond lasers [65]. Chichkov et al presented the theoretical models and explanations of experimental results from femtosecond, picosecond and nanosecond lasers [66]. Nolte et al reported the ablation of metals by ultrashort laser pulses [53]. All the above approaches are based on focused laser processing technologies, and time consuming is a significant disadvantage for low-cost mass production due to the laser scanning speed limit.

Compared with focused laser processing, an alternative approach is laser interference lithography technology, which is concerned with the use of interference patterns generated from two or several coherent beams of laser radiation for the modification of materials [25, 49]. Zhang et al demonstrated "periodic antireflection surface structure fabrication on silicon by four-beam laser interference lithography" [41]. Zhao et al made "a silver grating by direct laser interference writing" [67]. Pérez et al fabricated "the sub-micrometric metallic hollow-core structures by laser interference lithography" [68]. These approaches have demonstrated that laser interference lithography is a promising technology, which has the advantages of re-configurable patterns and the creation of program controlled structures over large areas for the fabrication of periodic structures on various materials [11]. However, the effect of laser fluences on silicon modification by laser interference is not adequately addressed considering the heat flow distribution, the radiation effects of laser plasma and the fluence accumulation with the selection of the number of exposure pulses or the interaction time.

5.2 Theoretical Analysis

5.2.1 Laser Interaction with Silicon Wafers

Different types of laser can be used in a wide range of material processing applications. The process of laser interaction with material involves many physical phenomena, which are transmission, conduction, absorption, reflection of radiant energy, convection and radiation of thermal energy.

Thus, the selection of appropriate process parameters is very important in order to achieve precise patterns which are desired [69]. Therefore, the laser sources with output energy, pulse duration, wavelength and beam profile have been selected to guarantee high speed and precise processing. In additional, laser interaction with materials is typically a dynamic and complicated process and also include that many factors [70], such as laser fluence, focus spot size, repetition rate and processing time setting, processing methodology and ambient (ambient temperature) can be affected the resulting patterns.

The laser interaction with a material is dominated by photophysical processes, which include the photothermal and the photochemiacal processes as shown in Figure 5.1. Photothermal process will dominate the interaction of laser and materials with high quantities of free electrons, just like metals and semiconductors. As one example of materials is silicon wafers and interaction, the incident light energy is absorbed by electrons in the silicon wafers. The electrons reach higher energy, travel in the silicon and transfer this absorbed energy to the silicon lattice by intense collisions. The temperature of the silicon wafer is increased and can be high enough to overpass the melting or vaporization temperature of silicon. Therefore, the phase changes from solid to liquid, to gas, as well as plasma state can be occur in this process [70]. The silicon wafer cools down the solid state maintaining the structures on the substrate surface after the laser irradiation. When the laser irradiation finishes, the material is cooled down in a very short period of time and returns to solid state but maintaining

Photothermal process will dominate the laser-matter interaction in materials with high quantities of free electrons like metals and semiconductors.

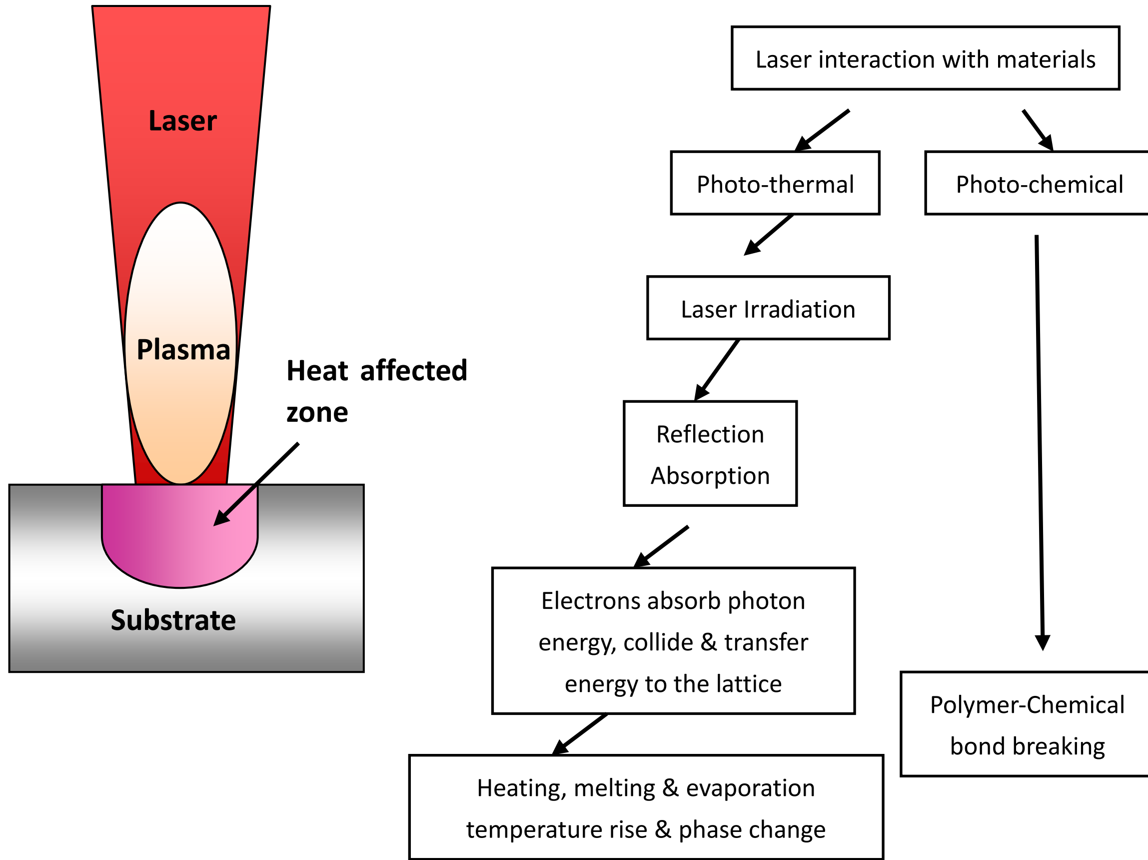

Figure 5.1 Dynamics of laser interaction with materials [70].

There are two physical models that can explain the interactions between laser and silicon wafer surface in the fabrication process of different structures: the heat transfer model and the radiation effects of laser plasma [71]. Following the laser radiation, the silicon wafer will be heated, melted and then vaporized, and several physical processes will also happen, such as oxidation, amorphization and re-crystallization. A heat flow expression can describe the laser influence process [53, 66].

$$C_e \frac{\partial T_e}{\partial t} = \frac{\partial}{\partial z} K \frac{\partial}{\partial z} T_e - \gamma (T_e - T_i) + S \tag{5.1}$$

$$C_i \frac{\partial T_i}{\partial t} = \gamma (T_e - T_i) \tag{5.2}$$

$$S = I(t) A \alpha \exp(-\alpha z) \tag{5.3}$$

where S is the laser heating source term, T_e and T_i are the temperatures of the electron gas and the lattice, C_e and C_i are the heat capacities, K is the thermal conductivity, γ is the coupling constant, $\tau_e = C_e / \gamma$ is the electron cooling time, and $\tau_i = C_i / \gamma$ is the lattice heating time. *I(t)* is the laser intensity and assumed to increase exponentially with time as $I(t) = I \exp(t / \tau_L)$, where τ_L is the laser pulse duration, A is the surface absorptivity, α is the material absorption coefficient, and I is the intensity distribution.

Femtosecond pulses [66]

In the case that the laser type is the femtosecond pulses laser, the laser pulse duration is shorter than the electron cooling time, that is $\tau_L << \tau_e$.

When $t << \tau_e$, the coupling of electron-lattice can be neglected. According to the Equation (5.1), it can be deduced and gives

$$C_e^{'} \partial T_e^2 / \partial t = 2 I_a \alpha \exp(-\alpha z) \tag{5.4}$$

$$T_e(t) = (T_0^2 + \frac{2 I_a \alpha}{C_e^{'}} t \exp(-\alpha z))^{1/2} \tag{5.5}$$

At the end of the laser pulse the electron temperature is given as:

$$T_e(\tau_L) \approx (\frac{2 F_a \alpha}{C_e^{'}})^{1/2} \exp(-z / \sigma) \tag{5.6}$$

Where, $I(t)=I_0$ is assumed constant, $I_a=I_0A$, and $T_0=T_e(0)$ is the initial temperature.

In additional, $T_e(\tau_L) >> T_0$ is assumed, $F_a = I_a \tau_L$ is the absorbed laser fluence, and $\delta = 2 / \alpha$ is the skin depth.

After the laser pulse, the electrons are rapidly cooled and the evolution of the electron and lattice temperatures is described by Equations (5.1)-(5.3) with S=0. The lattice temperature is given by

$$T_i \approx T_e^2(\tau_L)\frac{C_e^{'}}{2C_i} \approx \frac{F_a\alpha}{C_i}\exp(-\alpha z) \quad (5.7)$$

Equation (5.7) is determined by the average cooling time of the electrons. The process of femtosecond laser pulses interaction with silicon wafer can be considered as a direct solid-vapour (or solid-plasma) transition. Therefore, the femtosecond laser is a very precise and pure laser-processing interaction on the materials as its advantages.

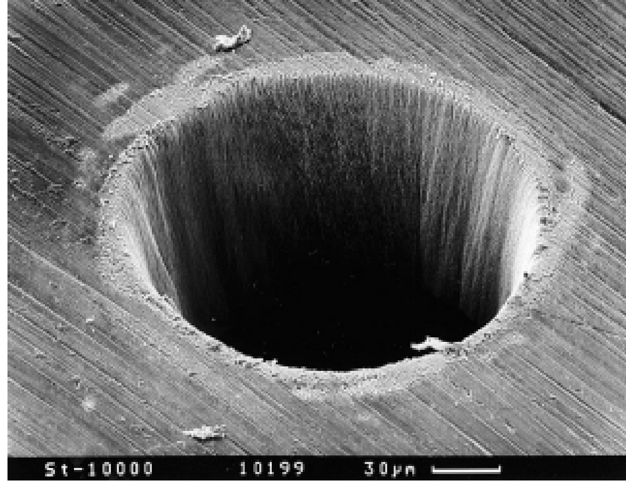

Figure 5.2 A SEM photograph of a hole drilled by femtosecond-pulse laser ablation.

Picosecond pulses [66]

In the case of picosecond laser pulses, the condition of $\tau_e << \tau_L << \tau_i$ has been fulfilled. When the time $t >> \tau_e$, which is equivalent to $C_e T_e / t << \gamma T_e$, Equations (5.1)-(5.3) can be written as

$$\partial / \partial z(k_e \partial T_e / \partial z) - \gamma(T_e - T_i) + I_a\alpha\exp(-\alpha z) = 0 \quad (5.8)$$

The temperatures electron and lattice at the end of the laser pulse are

$$T_e \approx \frac{I_a\alpha}{\gamma}\exp(-\alpha z) \quad (5.9)$$

$$T_i \approx \frac{F_a\alpha}{C_i}\exp(-\alpha z) \quad (5.10)$$

From Equations (5.7) and (5.10), it is noted that the equations for the lattice temperature are the same expressions from the femtosecond and picosecond regimes, respectively. In this case the lattice is heated on a picosecond time scale which results

in the creation of vapour and plasma phases happened at the surface. However, there is melted zone inside the sample and present the liquid phase to reduce the precision of laser process.

Nanosecond pulses [66]

Since the heating source is the nanosecond laser, and $\tau_L >> \tau_i$. It means that the temperatures of the electron gas T_e and the lattice T_i are equal, i.e. $T_e = T_i = T$. Hence, Equations (5.1) and (5.2) can be simplified as [66].

$$C_i \frac{\partial T}{\partial t} = \frac{\partial}{\partial z} K \frac{\partial}{\partial z} T + S \quad (5.11)$$

where *z* is the direction perpendicular to the silicon wafer surface. The process of laser interaction with the silicon wafer surface can be described as that the laser pulses firstly heat the silicon wafer surface to the melt and then to the boiling point.

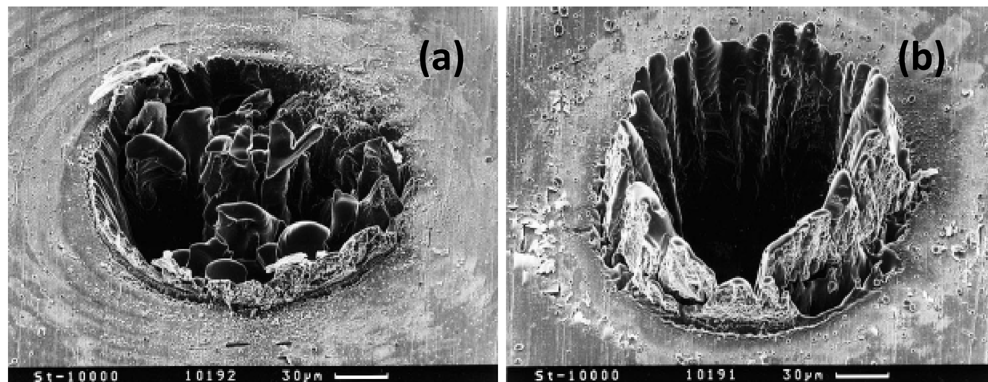

Figure 5.3 Holes drilled by a nanosecond-pulse, (a) 80ps and (b) 3.3ns [66].

5.3 Silicon Wafer Modification by Two-beam Laser Interference[55]

This section presents the study of silicon wafer modification by two-beam laser interference. In the section, two-beam laser interference was used to form gratings of pattern on silicon wafers with the fabrication process of different laser fluences and pulses in the air. The results were obtained from single laser pulse exposures and

multiple laser pulses was also investigated in this section. In the experiment, the laser wavelength was 1064nm, the pulse duration was 7-9ns, the repetition rate was 10Hz and the laser fluences were 637mJ/cm^2, 780mJ/cm^2 and 1280mJ/cm^2. The results indicate that the laser fluence and number of pulses have to be properly selected for the fabrication of gratings using laser interference.

5.3.1 Experimental Details

The experiment was carried out using a high power laser with the wavelength of 1064nm, the pulse duration of 7-9ns and the repetition rate of 10Hz, Different laser fluences and pulses were applied to modify silicon wafers in the air by two-beam laser interference. The emitted energy fluences of single pulses were 637mJ/cm^2, 780mJ/cm^2 and 1280mJ/cm^2, and the fluence of ten pulses was 1280mJ/cm^2. A two-beam laser interference lithography system was used to modify silicon wafers for the fabrication of gratings. In addition, in order to observe the evolution of gratings, the silicon wafer was irradiated with the energy fluence of 710mJ/cm^2 using two-beam laser interference. The structures of the surface of silicon wafer were observed by using atomic force microscope (AFM) and optical microscope. Figure 4.8 shows the setup and principle of two-beam laser interference lithography. One beamsplitter divided the input beam into two beams. A set of mirrors (M1, M2 and M3) steered the beams towards the substrate with the desired angles of incidence. The optical paths of the two beams were identical in order to ensure the spatial overlapping of the same parts of the laser spot in the interference point.

For two-beam laser interference, the pattern is an array of lines or grating as shown in Figure 4.8. The intensity distribution for the interference pattern I can be expressed using Equation (3.1). From Equation (3.1), it is evidenced that the peak intensity of interference pattern ($4I_0$) is greater than the sum of the intensities of the two interfering beams ($2I_0$). The period of the fringe pattern P can be calculated by Equation (3.2). The pattern period is a function of the wavelength and the incident angle of the

beams. It indicates that the period can be adjusted from nano to micro meters, which is flexible for many applications. Figure 5.4 illustrates the principle of two-beam laser interference lithography with three material modification thresholds corresponding to three planes. A particular feature size can be obtained by adjusting the laser pulse energy according to the material modification thresholds.

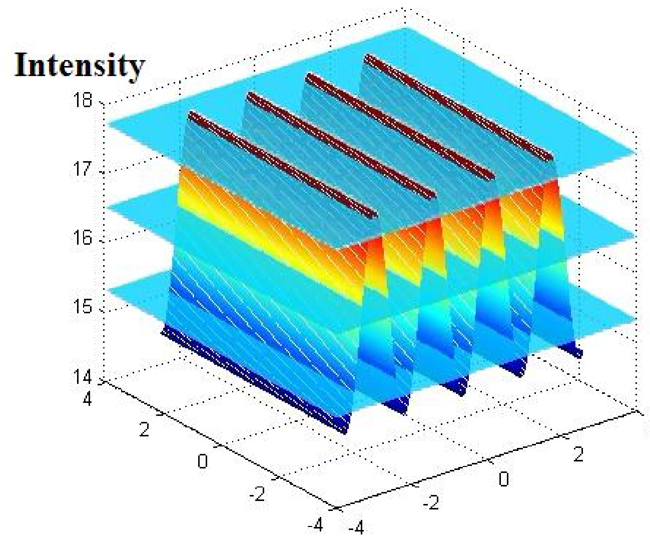

Figure 5.4 Principle of two-beam laser interference lithography.

Table 5.1 Beam configuration parameters for the selected interference pattern

Parameter	Beam 1	Beam 2
Angle of Incidence	5.5°	5.5°
Azimuth	0°	180°
Polarization	0°	0°

5.3.2 Morphological Features with Different Fluences of Single and Multiple Laser Pulses [58]

The grating was generated on a silicon wafer with a single laser pulse of 786mJ/cm^2 using two-beam laser interference lithography, as shown in Figure 5.5. Equation (3.1)

expresses the intensity distribution of two-beam laser interference. The peak intensity of interference pattern (*$4I_0$*) appeared on the polished silicon surface.

Increasing of the laser fluence to 821mJ/cm^2, the formation of the holes can be observed by AFM in Figure 5.6. These circular holes first happened on the silicon wafer grating where peak intensities were formed, and some holes were evidently observed with its cross-section analysis as shown in Figure 5.6(c). When the laser fluence was increased to 1280mJ/cm^2, the size of the holes was significantly increased and the gratings were not evident as shown in Figure 5.7 The circular holes were generated during the lithography due to the inhomogeneous intensity distribution of laser beams or locally enhanced absorption caused by surface defects or the dust on the surface.

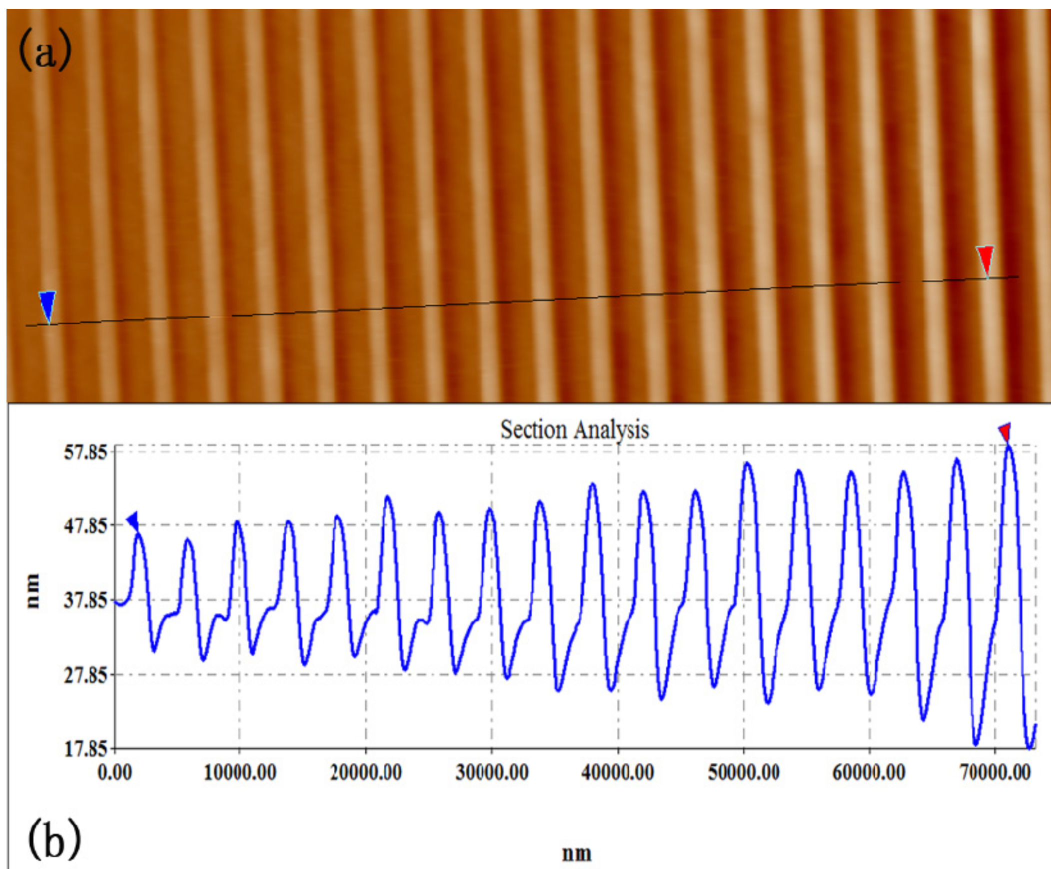

Figure 5.5 (a) AFM image of the result from a single laser pulse with the fluence of 786mJ/cm^2; (b) Cross-section analysis.

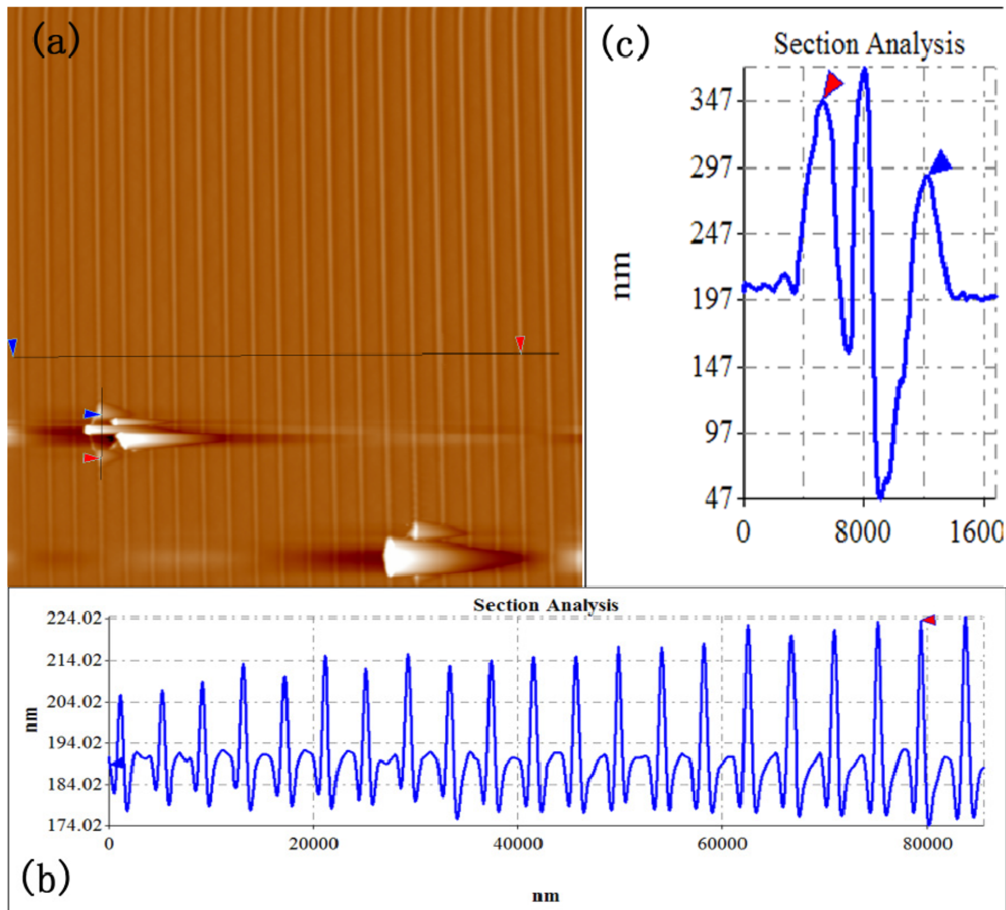

Figure 5.6 (a) AFM image of the result from a single laser pulse with the fluence of 821mJ/cm^2; (b) and (c) Cross-section analysis.

The dominant process of nanosecond laser ablation is "the heating of the target material through the liquid phase to the vapour phase, resulting in expansion and expulsion of the desired target material" [72]. When the laser fluence was further increased to ten pulses of 1280mJ/cm^2, as shown in Figure 5.8, the strongly overheated surface layer was deformed and removed by phase explosion, normal boiling including inhomogeneous bubbles occurred in the remaining liquid layer [73]. Afterwards, the surface was corrugated from the local vaporization and subsequently re-deposited material.

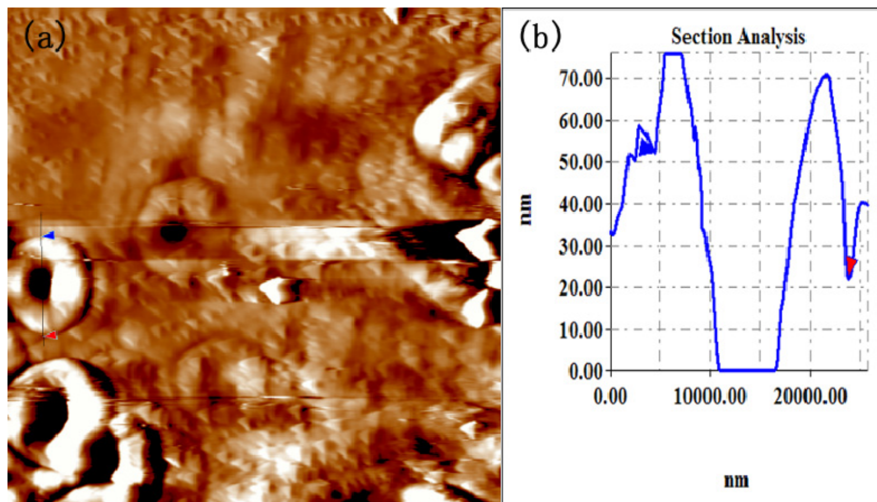

Figure 5.7 (a) AFM image of the result from a single laser pulse with the fluence of 1280mJ/cm^2; (b) Cross-section analysis (hole diameter: 16529nm; depth: >75nm).

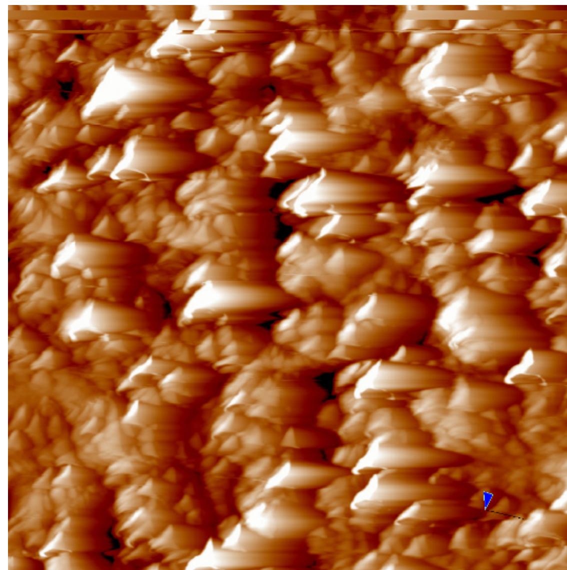
Figure 5.8 AFM image of the result from 10 laser pulses with the fluence of 1280mJ/cm^2.

5.3.3 Evolution of Grating Structures Formed by Laser Interference

Other interesting surface morphologies of gratings were observed by OM and AFM, as shown in Figures 5.9 and 5.10. The evolution of the surface morphology was studied by performing experiment with the laser fluence of 710mJ/cm^2. Due to the Gaussian distribution of laser energy and the high temperature of the centre, more impacts can be seen in the centre of the irradiated area than the border region from Figure 5.9. It is clearly observed, from the border to the centre of the irradiated area, that the width of the grating lines corresponding to the peak intensity lines of the interference pattern is

also increased with the laser fluence. Figure 5.10 clearly shows the detail of the grating evolution from the border to the centre of the irradiated area by AFM. Figures 5.10(a)-(b) show the feature size, period and height. Close to the centre of the irradiated area, the grating lines become wider and higher, and the silicon wafer surface becomes rougher, as shown in Figures 5.10(c)-(f).

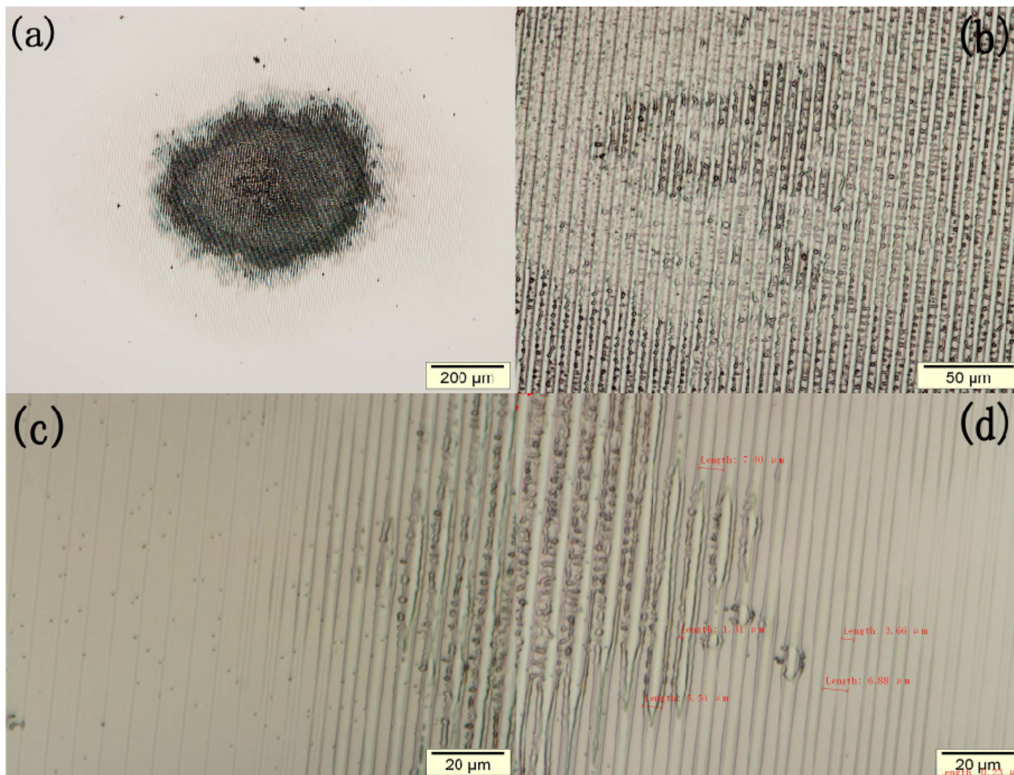

Figure 5.9 Optical microscopy images of the results from a single laser pulse with the fluence of 710mJ/cm^2; (a) Whole pattern spot, (b) Centre of the irradiated area, (c) and (d) Border regions of the irradiated area.

More close to the centre of the irradiated area, the circular holes are formed along the peak intensity lines of the interference pattern, and the bubbles are ejected from the melt layer, as shown in Figure 5.9(d). With the increase of fluences, the circular holes have connected to each other or emerged together, and led to the single grating lines divided into double ones with more outthrusts, showing the phenomena of the re-deposition and re-crystallization in Figures 5.9(b), 5.10(c) and 5.10(e). The phenomena can be observed all over the centre of the irradiated area in Figure 5.9 (b).

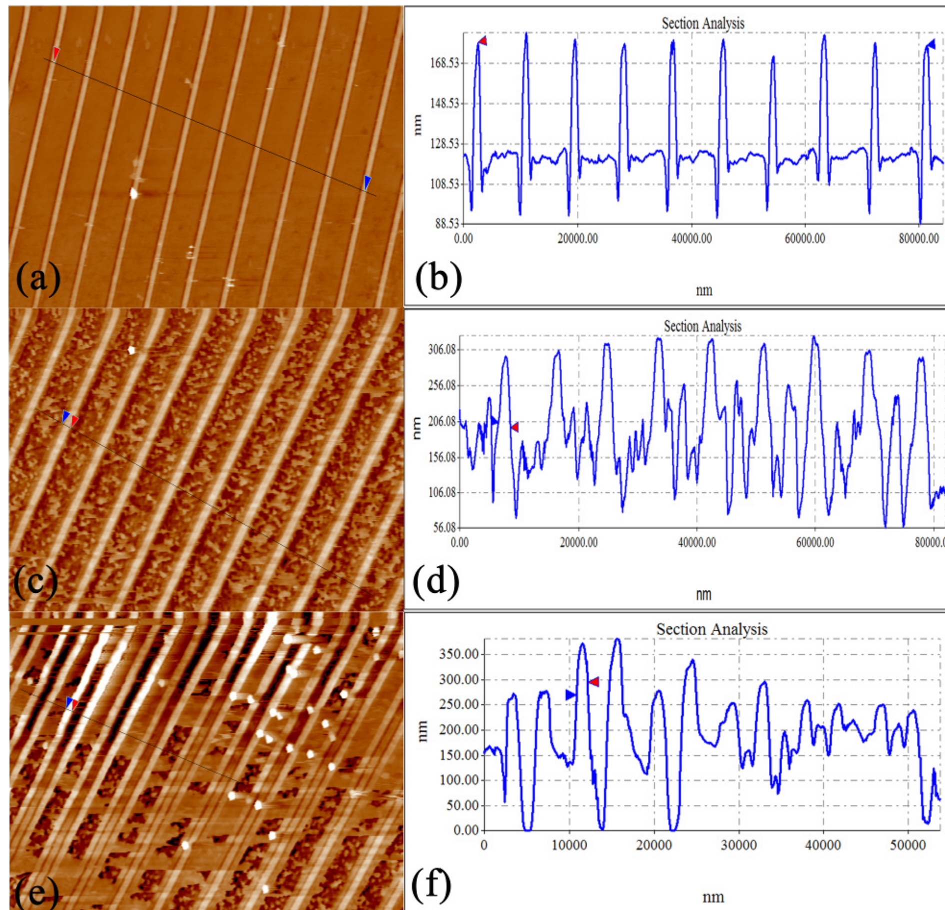

Figure 5.10 (a), (c) and (e) AFM images of the result from a single laser pulse with the fluence of 710 mJ/cm^2; (b) Cross-section analysis (period: 8479nm; feature size: 1868nm; height: 82.30nm); (d) Cross-section analysis (period: 8144nm; feature size: 2012nm; height: 251nm); (f) Cross-section analysis (period: 8086nm; feature size: 1343nm; height: 374nm).

In the section, two-beam laser interference was used to form gratings of pattern on silicon wafers with the fabrication process of different laser fluences and pulses in the air. The results were obtained from single laser pulse exposures and multiple laser pulses were also investigated in this section. Several physical processes such as the formation of bubbles and the ablation have been discussed. The results indicate that the laser fluence and number of pulses have to be properly selected for the fabrication of gratings using laser interference.

5.4 Effect of Pulse Repetition Rate on Silicon Wafer Modification by Four-beam Laser Interference[59]

This section discusses the effect of pulse repetition rates on silicon wafer modification

by four-beam laser interference. In the section, four-beam laser interference was used to from a pattern of dots on silicon wafers. The results were obtained from 10 laser exposure pulses with the single laser fluence of 283mJ/cm^2, the pulse repetition rates were 1Hz, 5Hz and 10Hz, the laser wavelength was 1064nm and the pulse duration 7-9ns. The results have been observed using a scanning electron microscope (SEM) and optical microscope. They indicate that the laser pulse repetition rate has to be properly selected for the fabrication of the structures of dots using four-beam laser interference.

5.4.1 Experiment

The laser interference system used a seeded Q-switched Nd:YAG laser source with 1064nm output wavelength, pulse duration of 7-9 ns, the pulse repetition rate of 1Hz, 5Hz and 10Hz, and Gaussian beam of 6mm in diameter. In the four-beam interference system, as shown in Figure 5.12, one laser beam was split into four parts using beam splitters and mirrors. Three optical beamsplitters divided the input beam into four noncoplanar coherent beams. A set of mirrors steered (M1, M2, M3, M4, M5 and M6) the beams towards the substrate of silicon wafer with the desired angles of incidence ($\theta_1 = \theta_2 = \theta_3 = \theta_4 = \theta$). The optical paths of the two beams were identical in order to ensure the spatial overlap of the same parts of the laser spot in the interference point.

The emitted energy fluence of a single pulse was 283mJ/cm^2, divided into four beams by beam splitters. The four beams were recombined on the silicon wafer surface with specified incident angles, creating periodic interference patterns. The four beams were symmetrically configured in space distribution with the azimuthal angles of 0°, 90°, 180° and 270°. In the experiment, the incident angles of 5° were chosen, and interference patterns with a period of 6.2μm were generated. The beam configuration parameters have been shown in Table 5.2. The combination of 1/4 wave plates and polarizers were used to control the pulse energy level of single beams varied from 20 mJ to 60 mJ and the polarization direction of each beam. The polarization has a great influence on the intensity distribution of laser interference. The substrates used in the experiment were single side polished monocrystalline silicon wafers with (100) orientation. After the

structures fabricated on the samples, the SEM and optical microscope were used to analyze and examine them.

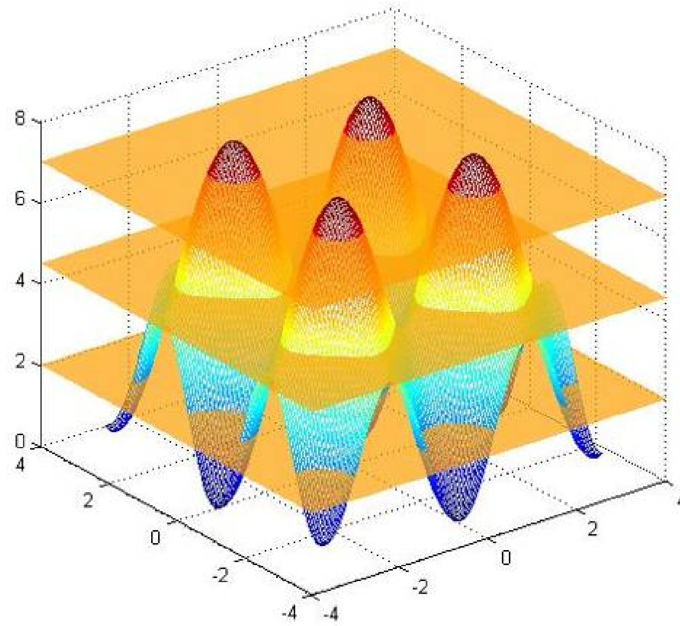

Figure 5.11 Principle of four-beam laser interference lithography.

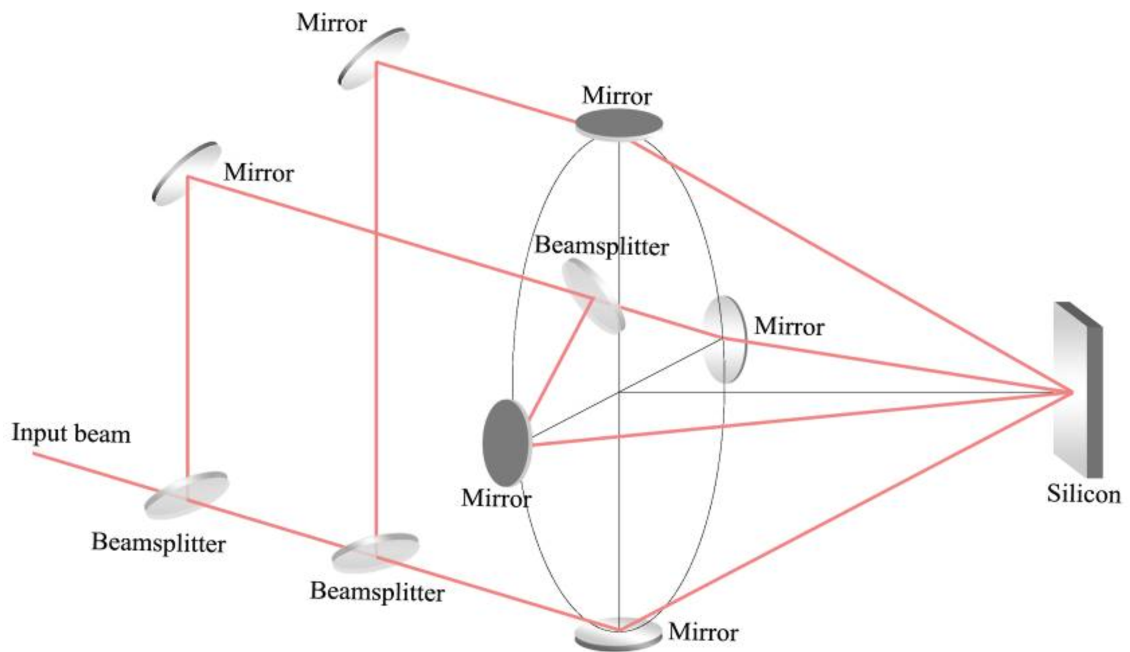

Figure 5.12 The schematic diagram of four-beam laser interference system.

Table 5.2 Beam configuration parameters for the selected interference pattern

Parameter	Beam 1	Beam 2	Beam 3	Beam 4
Angle of Incidence	5°	5°	5°	5°
Azimuth	0°	90°	180°	270°
Polarization	0°	90°	0°	90°

5.4.2 Results and Discussions

Figure 5.13 shows the optical images of damage centre of the irradiated area formed on the surface of silicon wafer and the morphologies were fabricated by four-beam laser interference technology with 10 laser pulses and pulse repetition rates were 1Hz, 5Hz and 10Hz respectively. Each of the laser energy fluences for all the samples was 283mJ/cm^2, which was single pulse fluence of well-defined dots in the previous experiments on silicon wafer. The images show that the pulse repetition rates affect the damage of morphologies on the silicon surface by laser interference technology. Changed the value of the pulse repetition rates 1Hz, 5Hz and 10Hz, it was evidently observed that the damage was decreased significantly on the irradiated silicon surface and the morphology of dots was gradually well-defined.

For the relationship of the nanosecond laser interaction with the silicon wafer, there is a heat flow expression describing the laser impact process as shown in Equation (5.14) [66]:

$$C_E \frac{\partial T_E}{\partial t} = \frac{\partial}{\partial T} K \frac{\partial}{\partial X} T_E + S(x,t) \tag{5.14}$$

where *S(x,t)* is the laser heating source term, T_E is the temperatures of the electron gas, C_E is the heat capacities, *K* is the thermal conductivity, *G* is the coupling constant, and $\tau_e = C_E / G$ is the electron cooling time. Equation (5.14) is used to calculate the temperature of samples in nanosecond heating experiments. The process of nanosecond laser interaction with the silicon wafer, the laser pulses firstly heat the silicon wafer to the melt and then heat to the boiling point of silicon wafer [66].

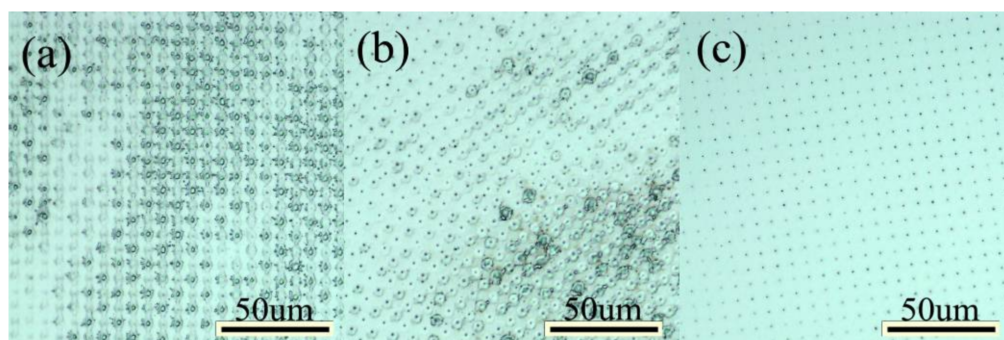

Figure 5.13 Optical images of damage centre of the irradiated area fabricated by four-beam laser interference technology; (a) The pulse repetition rate of 1 Hz and 10 laser pulses; (b) The pulse repetition rate of 5 Hz and 10 laser pulses and (c) The pulse repetition rate of 10 Hz and 10 laser pulses.

Figure 5.13 shows that the pulse repetition rates affect the morphologies of damage on silicon wafer surface by laser interference technology. In other words, in the case of the interaction of multiple laser pulses with the silicon wafer, there are two parameters that the energy accumulation and the energy diffusion affect the morphologies of damage on the silicon surface by laser interference technology.

Figure 5.14 shows the SEM images of damage centre of the irradiated area with the images of single dots, using the 10 laser pulses and the pulse repetition rates were 1Hz, 5Hz and 10Hz, respectively. In the case of the repletion rate was 1Hz, the arrays of holes on the silicon wafer surface were observed, as shown in Figures 5.14 (a)-(b). The reason of the phenomena could be explained that there was enough time to make laser energy thermal diffusion and homogenization in a certain area. Furthermore, the laser energy accumulation had been greater than the thresholds of melt silicon, when the 10 laser pulses were working in the process of ablation in the area. In the case that the repetition rate was 5Hz, the arrays of holes changed dots with thick ripples and many particles on silicon wafer surface, as shown in Figures 5.14 (c)-(d). In the case that the repetition rate was 10Hz and competed with the repetition rate of 5Hz, the arrays of dots changed greater, appeared thin ripples around the dots and less particles, as shown in Figures 5.14 (e)-(f). Due to increasing of the laser pulse repetition rate, the time of laser energy thermal diffusion contracted short and more energy accumulated

on the centre of the area. The thermal energy made the speed of molecular motion to change faster and gasification inside silicon wafer. Therefore, the formation of array of dots on the surface of silicon wafer was according to this reason.

The ripples around the dots like the frozen capillary waves and the formation are due to molten silicon, as shown in Figures 5.14(c)-(f). The following is the principle for the ripples [68]. The space of the capillary wave d in a shallow liquid surface is given by [48]

$$d = \left[\frac{\sigma \cdot h}{\rho}\right]^{1/4} (2 \cdot \pi \cdot \tau_l)^{1/2} \tag{5.15}$$

where σ is the coefficient of surface tension, τ_l is the life time of the molten state, ρ is the density of the molten silicon, and the height of the molten layer h is defined by [74]

$$h = \frac{f_0(1-R)}{C_v \cdot Tm + Lm} \tag{5.16}$$

where R is the reflectivity, f_0 is the laser fluence, C_v is the specific heat capacity, *Lm* and Tm are the specific heat of melting and the melting temperature, respectively. The time of need to melt a highly absorbing material τ_m can be defined as [68]

$$\tau_m = \frac{1}{D}\left(\frac{\theta_m \cdot k_s}{I_a}\right) \tag{5.17}$$

where D is the thermal diffusivity, $\theta_m = t_m - t_{(\alpha)}$ where tm is the melting temperature and $t_{(\alpha)}$ is the temperature of the substrate far away from the irradiated area, k_s is the thermal conductivity and I_a is defined as $I_a = I_0 \cdot (1-R)$ where I_0 is the initial laser light intensity and R is the reflectivity of silicon. The lifetime of molten state τ_l can be defined as $\tau_l = \tau_s - \tau_m$, where τ_s is the pulse duration. These results shown in Figure 5.14 can be explained by the fact that the different pulse repetition rates have different thermal diffusion times between laser pulses.

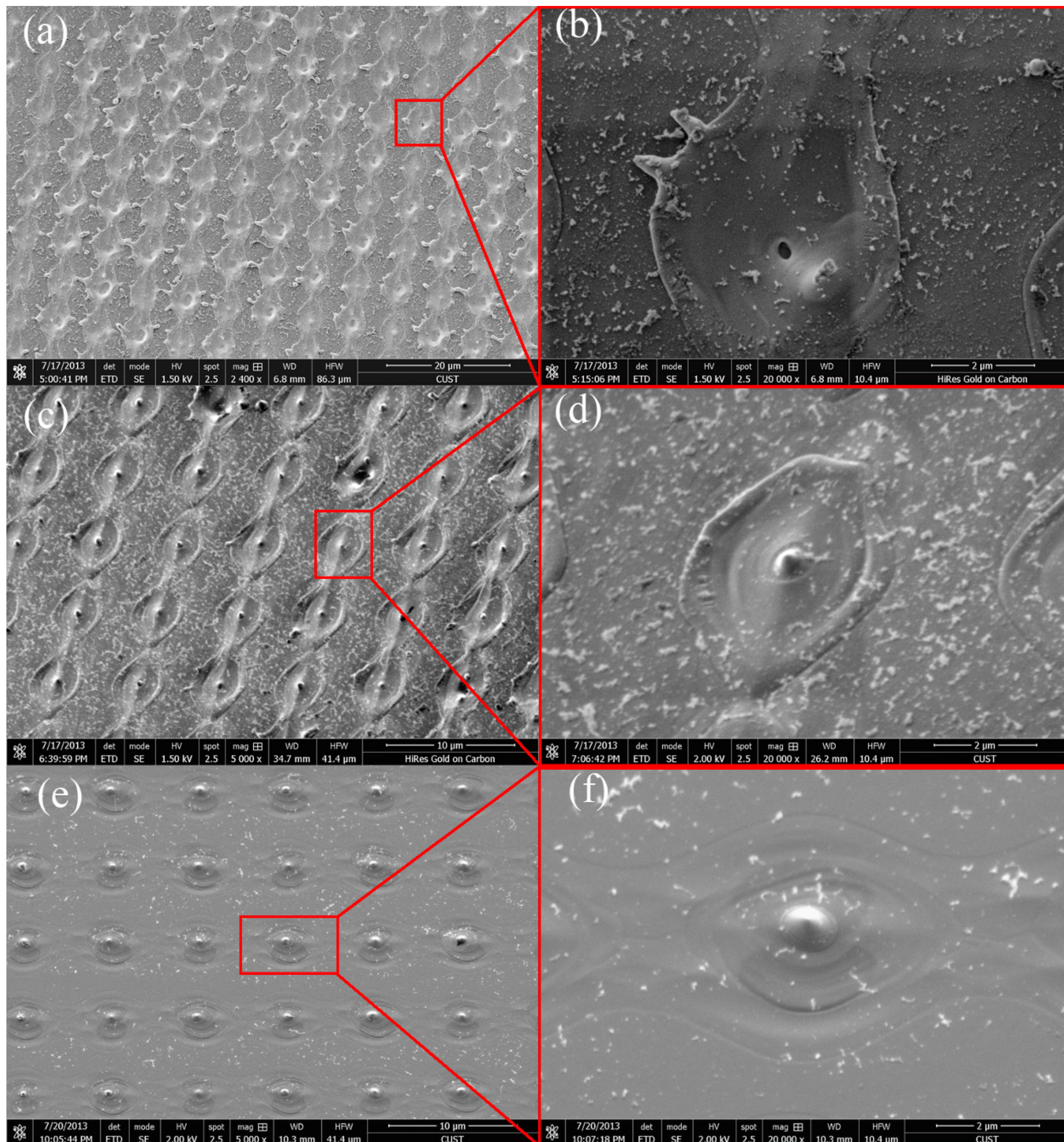

Figure 5.14 SEM images of damage centre of the irradiated area; (a)-(b) The pulse repetition rate of 1 Hz and 10 laser pulses; (c)-(d) The pulse repetition rate of 5 Hz and 10 laser pulses and (e)-(f) The pulse repetition rate of 10 Hz and 10 laser pulses; the scale bar of (a) is 20 μm, the scale bar of (a) is 20 μm, the scale bar of (a) is 20 μm, the scale bar of (a) is 20 μm, the scale bars of (e) and (e) are 10 μm, the scale bars of (b), (d) and (f) are 2 μm.

In this section, four-beam laser interference was used to form a pattern of dots on silicon wafers. The results have been observed using the SEM and optical microscope. With the different pulse repletion rates, several physical processes such as the formation of holes, dots, ripples and the ablation have been discussed. The results

indicate that the laser pulse repetition rates have to be properly selected for the fabrication of the structures of dots and affect the structures or shapes using four-beam laser interference lithography.

5.5 Effects of Laser Fluences on Silicon Modification by Four-beam Laser Interference

This section discusses the effects of laser fluences on silicon modification by four-beam laser interference. In this section, four-beam laser interference was used to pattern on silicon wafers for the fabrication of various structures, and the numbers of laser pulses were applied to the process in the air. By controlling the parameters of laser irradiation, different shapes of silicon structures have been fabricated. The results were obtained from the single laser fluences of 354 mJ/cm^2, 495 mJ/cm^2 and 637 mJ/cm^2, the pulse repetition rates of 10 Hz, the laser exposure pulses of 30, 100 and 300, the laser wavelength of 1064 nm and the pulse duration of 7-9 ns. The effects of the heat transfer and the radiation effects of laser interference plasma on silicon wafer surfaces were investigated. The equations of heat flow and radiation effects of laser plasma of interfering patterns in a four-beam laser interference distribution are proposed to describe their laser radiation impacts on silicon wafer surfaces. The experimental results have shown that the laser fluences have to be properly selected for the fabrication of well-defined surface structures in a four-beam laser interference process. Laser interference patterns can directly fabricate different shape structures for their corresponding applications.

5.5.1 Experiment

The laser interference system used a seeded Q-switched Nd:YAG laser source with the wavelength of 1064 nm, pulse duration of 7-9 ns, pulse repetition rate of 10 Hz and Gaussian beam of 6 mm in diameter. Two experiments were carried out. One was that the single laser pulses of 354 mJ/cm^2, 495 mJ/cm^2 and 637 mJ/cm^2 were used. The other was that the laser pulses of 30, 100 and 300 were used. In the experiments, the

four beams were symmetrically configured in the space distribution with the azimuthal angles of 0°, 90°, 180° and 270°. The incident angles of 5.5°and the polarization angles of 0°, 90°, 0° and 90° were selected. The substrates used in the experiments were single side polished monocrystalline silicon wafers with (100) orientation. The beam configuration parameters have been shown in Table 5.3. After the structures fabricated on the samples, SEM was used to perform the measurements.

Table 5.3 Beam configuration parameters for the selected interference pattern

Parameter	Beam 1	Beam 2	Beam 3	Beam 4
Angle of Incidence	5.5°	5.5°	5.5°	5.5°
Azimuth	0°	90°	180°	270°
Polarization	0°	90°	0°	90°

5.5.2 Results and Discussions

There are two physical models that explain the interactions between the laser and silicon wafer surface in the fabrication process of different structures: the heat transfer model and the radiation effects of laser plasma [71]. Following the laser radiation, the silicon wafer will be heated, melted and then vaporized, and several physical processes will also happen, such as oxidation, amorphization and re-crystallization.

For the heat transfer interaction process between the laser and silicon wafer surface, there are two crucial absorption mechanisms, which are intrinsic absorption and free-carrier absorption during the interaction process between the laser and silicon wafer surface depending on the laser and material parameters [65]. A heat flow expression can describe the laser influence process [53, 66]

$$C_e \frac{\partial T_e}{\partial t} = \frac{\partial}{\partial z} K \frac{\partial}{\partial z} T_e - \gamma (T_e - T_i) + S \tag{5.18}$$

$$C_e \frac{\partial T_e}{\partial t} = \frac{\partial}{\partial z} K \frac{\partial}{\partial z} T_e - \gamma (T_e - T_i) + S \tag{5.19}$$

$$S = I(t) A \alpha \exp(-\alpha z) \tag{5.20}$$

where *S* is the laser heating source term, T_e and T_i are the temperatures of the electron gas and the lattice, C_e and C_i are the heat capacities, *K* is the thermal conductivity, γ is the coupling constant, $\tau_e = C_e / \gamma$ is the electron cooling time, and $\tau_i = C_i / \gamma$ is the lattice heating time. The spatial model of the incident laser beam is assumed as Gaussian distribution and assumed to increase exponentially with time as $I(t) = I \exp(t / \tau_L)$, where τ_L is the laser pulse duration, *A* is the surface absorptivity, α is the material absorption coefficient, and I is the intensity distribution. The heat flow expression for the single beam laser influence expressed in Equations (5.18)-(5.20) can explain the phenomena of laser interaction with the silicon wafer such as heat distribution, transfer and ablation [63].

The intrinsic absorption is the generation of electron–hole pairs when electrons are thermally excited from valence bands into conduction bands. The condition of the intrinsic absorption is that the corresponding photon energy (*hv*) is greater than the band gap (*Eg*). In the experiments, the laser wavelength was 1064 nm, the band gap (*Eg*) of silicon was 1.12 eV at room temperature, and the corresponding photon energy was $hv = h(c / \lambda) = 1.17eV > 1.12eV$. The temperatures T_e and T_i are produced by intrinsic absorption and free-carrier absorption, as shown in Equations (5.18) and (5.19). The process of laser energy transition inside a silicon wafer can be considered as the generation of carriers, the energy absorption of carriers, and the energy transfer from carriers to lattices [65].

Since the heating source is the nanosecond laser, and $\tau_L >> \tau_i$. It means that the temperatures of the electron gas *Te* and the lattice *Ti* are equal, i.e. $T_e = T_i = T$. Hence, Equations (5.18) and (5.19) can be simplified as [66]

$$C_i \frac{\partial T}{\partial t} = \frac{\partial}{\partial z} K \frac{\partial}{\partial z} T + S \tag{5.21}$$

where *z* is in the direction perpendicular to the silicon wafer surface. The process of laser interaction with the silicon wafer surface can be described as that the laser pulses

firstly heat the silicon wafer surface to the melt and then to the boiling point [66].

In the case of four-beam laser interference, the interference pattern consists of an array of periodic intensity distributions. Figure 5.11 shows the principle of four-beam laser interference lithography with the intensity distribution from computer simulation. The intensity distribution of interference pattern $I_{m\times n}$ can be expressed as

$$I_{mn} = \begin{bmatrix} I_{11} & I_{12} & \cdots\cdots & I_{1n} \\ I_{21} & I_{22} & \cdots\cdots & I_{2n} \\ \cdots\cdots & \cdots\cdots & \cdots\cdots & \cdots\cdots \\ I_{m1} & I_{m2} & \cdots\cdots & I_{mn} \end{bmatrix} \tag{5.22}$$

and each element in the matrix can be considered as a laser intensity distribution. The laser interference intensity is assumed to increase exponentially with the exposure time. Hence, the laser interference intensity $I(t)_{m\times n}$ with the exposure time *t* expressed as [53]

$$I(t)_{mn} = I_{mn}\exp(t/\tau_L) = \begin{bmatrix} I_{11} & I_{12} & \cdots\cdots & I_{1n} \\ I_{21} & I_{22} & \cdots\cdots & I_{2n} \\ \cdots\cdots & \cdots\cdots & \cdots\cdots & \cdots\cdots \\ I_{m1} & I_{m2} & \cdots\cdots & I_{mn} \end{bmatrix} \cdot \exp(t/\tau_L) \tag{5.23}$$

and the laser interference heating source term $S_{m\times n}$ can be expressed as

$$\begin{aligned} S_{mn} &= I(t)_{mn} A\alpha \exp(-\alpha z) = I_{mn} A\alpha \exp(-\alpha z + t/\tau_L) \\ &= \begin{bmatrix} I_{11} & I_{12} & \cdots\cdots & I_{1n} \\ I_{21} & I_{22} & \cdots\cdots & I_{2n} \\ \cdots\cdots & \cdots\cdots & \cdots\cdots & \cdots\cdots \\ I_{m1} & I_{m2} & \cdots\cdots & I_{mn} \end{bmatrix} \cdot A\alpha \exp(-\alpha z + t/\tau_L) \end{aligned} \tag{5.24}$$

Figure 5.15 shows a sectional plot of the four-beam laser interference intensity distribution based on the Gaussian laser interference source. The heat flow expression of the four-beam laser interference distribution can be written as

$$C_i \frac{\partial T_{mn}}{\partial t} = \frac{\partial}{\partial z_{mn}} K \frac{\partial}{\partial z_{mn}} T_{mn} + S_{mn} \tag{5.25}$$

where T_{mn} is the temperature distribution of laser interference and Z_{mn} is the direction perpendicular to the silicon wafer surface. Each interfering dot intensity distribution in an interference pattern can be considered as a heat flow process, and Equation (5.25) describes the process of an array of the dot intensity distributions. Different distributions of temperatures and depths with time on silicon surface can be obtained according to the total heat flow process of four-beam laser interference.

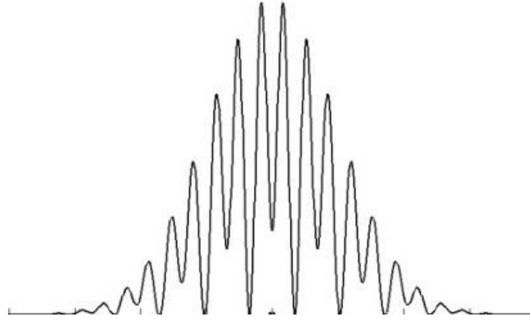

Figure 5.15 A sectional plot of the four-beam laser interference intensity distribution.

An expression for the ablation threshold fluence after irradiation with *N* pulses is related to the single shot ablation threshold [63]

$$\phi(N) = \phi(1) \cdot N^{\xi - 1} \tag{5.26}$$

where $\phi(N)$ denotes the modification threshold fluence for N laser pulses, and ξ is a material-dependent coefficient of 0.845. The diameter of the ablation crater D is related to the maximum laser fluence on the silicon wafer as the following expression [75]

$$D^2 = 2w_0^2 \ln\left(\frac{\phi_0}{\phi_{th}}\right) \tag{5.27}$$

where, ϕ_0 is the maximum fluence of the Gaussian beam profile, ϕ_{th} is the ablation threshold fluence, and w_0 is the beam radius.

Thus, for the four-beam laser interference, Equations (5.26) and (5.27) can be expressed in the form of matrix as

$$\phi_{mn}(N) = \phi_{mn}(1) \cdot N^{\xi - 1} \tag{5.28}$$

$$D_{mn}{}^{2} = 2w_{0mn}^{2} \ln\left(\frac{\phi_{0mn}}{\phi_{thmn}}\right) \tag{5.29}$$

An accumulation of energy (i.e. non-complete dissipation of the deposited energy) into the silicon wafer has also successfully been employed as $N \cdot \phi_{mn}(N)$.

For the laser plasma process that affects on the silicon wafer surface, the accumulation of laser energy can cause the increase of the temperature of silicon wafer, break its threshold, and make a small part of the sample melted and gasified. Then, the gaseous silicon can tend to ionize and form the laser plasma. In addition, the laser plasma can absorb more laser energy, becomes high-temperature and high-pressure, and then continuously explodes sharply and compresses the ambient air [76].

Hence, the generation and expansion of the laser plasma can cause the appearance of laser shock wave, which forms the flower-like silicon structures and the subsequent heat transfer inside the silicon wafer. Each of flower-like silicon structures consists of a silicon hole and many irradiated particles which are homogeneous around the hole, as shown in Figure 5.16. The shock wave radius can be written as [77]

$$R(t) = A\left(\frac{Q}{\rho_1}\right)^{\frac{1}{5}} t^{\frac{2}{5}} \tag{5.30}$$

where *Q* is the laser energy, *R* is the radius of laser shock wave, t is the interaction time, ρ_1 is the density of surrounding air, and A is the constant related to the air parameters. Thus, in the case of four-beam laser interference, the laser energy Q_{mn} distribution can be expressed as

$$Q_{mn} = \begin{bmatrix} Q_{11} & Q_{12} & \cdots\cdots & Q_{1n} \\ Q_{21} & Q_{22} & \cdots\cdots & Q_{2n} \\ \cdots\cdots & \cdots\cdots & \cdots\cdots & \cdots\cdots \\ Q_{m1} & Q_{m2} & Q_{m3} & Q_{mn} \end{bmatrix} = I_{mn} \cdot S_{Amn} \cdot T_{Laser} \tag{5.31}$$

$$S_{\mathrm{A}mn} = \begin{bmatrix} S_{A11} & S_{A12} & \cdots\cdots & S_{A1\mathrm{n}} \\ S_{A21} & S_{A22} & \cdots\cdots & S_{A2n} \\ \cdots\cdots & \cdots\cdots & \cdots\cdots & \cdots\cdots \\ S_{Am1} & S_{Am2} & \cdots\cdots & S_{Amn} \end{bmatrix} \tag{5.32}$$

where $T_{Laser} = N_{laser} \cdot \tau$, *N* laser is the number of laser pulses, τ is the pulse duration, I_{mn} is the laser fluence, and S_{Amn} is the area of the laser spot. The four-beam interference shock wave radius can be written as

$$R_{mn}(t) = A(\frac{Q_{mn}}{\rho_1})^{\frac{1}{5}} t^{\frac{2}{5}} = A(\frac{I_{mn} \cdot \mathrm{S}_{\mathrm{Amn}} \cdot T_{Laser}}{\rho_1})^{\frac{1}{5}} t^{\frac{2}{5}} \tag{5.33}$$

Compared to single laser beam processing, an array of multiple laser shock waves can be obtained, and the laser shock wave radius distribution on the silicon wafer surfaces can be estimated by Equation (20).

Figure 5.16 shows the SEM images of an array of flower-like silicon structures fabricated by four-beam laser interference lithography with the single laser fluences of 354 mJ/cm^2 (Figure 5.16 (a)), 495 mJ/cm^2 (Figure 5.16 (b)) and 637 mJ/cm^2 (Figure 5.16 (c)), and the pulse repetition rate of 10 Hz, the laser wavelength of 1064 nm and the pulse duration of 7-9 ns. Figures 5.16 (a)-(c) show the laser plasma processes with the splashed flower-like silicon structures around each of the silicon holes.

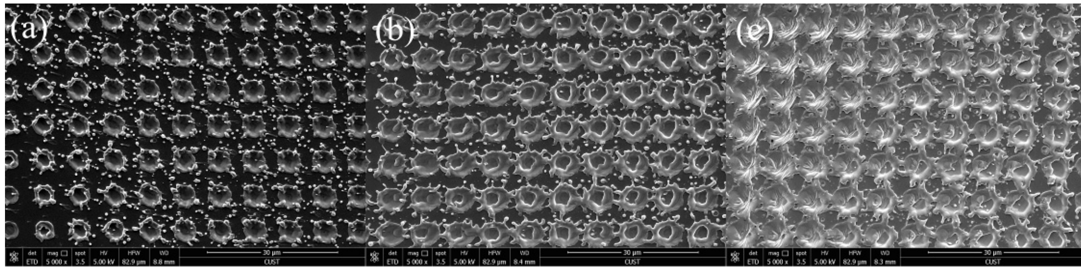

Figure 5.16 SEM images of the flower-like silicon structures fabricated by four-beam laser interference lithography. (a) the single laser fluence of 354 mJ/cm^2, (b) the single laser fluence of 495 mJ/cm^2 and (c) the single laser fluence of 637 mJ/cm^2.

In the case that the laser fluence was 354 mJ/cm^2, and an array of flower-like silicon

structures on the beam irradiation region was observed on the silicon wafer surface, as shown in Figure 5.16 (a). Figure 5.17 shows the diameter sizes of holes with error bars obtained from different laser fluences. The error bars were the average of 10 samples. The average diameter size of the obtained flowers was approximately 6.5 µm and each of flowers consists of the silicon hole and many irradiated particles which are homogeneous around the silicon hole. The average diameter size of the holes was about 2.7 µm and that of the particles around the silicon holes was about from 300 nm to 800 nm. When the laser fluence was 495 mJ/cm^2, and an array of large flower-like silicon structures was observed, as shown in Figure 5.16 (b). The average diameter size of flowers was increased to about 7.5 µm, that of the holes was increased to about 3.8 µm and the particles were distributed around the hole on the silicon wafer surface. When the laser fluence was 637 mJ/cm^2, the diameter size of the flowers became larger, as shown in Figure 5.16 (c). The average diameter size of flowers was about 7.9 µm and almost all the particles were connected to the centre of the flower. The holes became larger on the silicon wafer surface and the average diameter size was about 4.5 µm. Figure 5.16 indicates that different laser fluences can produce different shapes of flower-like silicon structures. The formation process can be provided by the condition of melting, gasification and ionization of silicon [77]. Thus, the particles have splashed around each of silicon holes in the experiment.

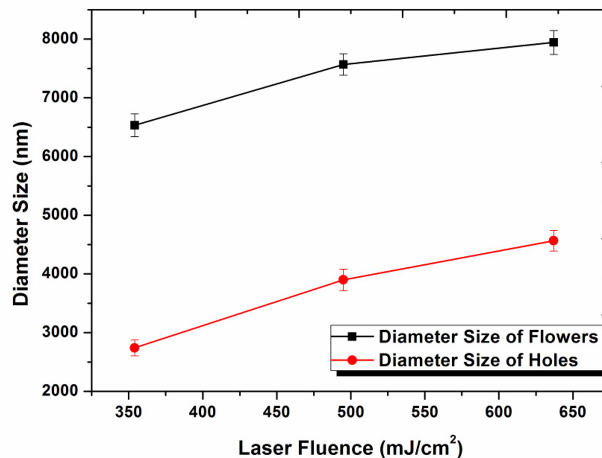

Figure 5.17 Diameter sizes of holes with error bars to the average size obtained from different laser fluences.

Figures 5.18-5.20 show the results obtained from the repetition rate of 10 Hz and the laser pulses of 30, 100 and 300. Each laser fluence for all the samples was 637 mJ/cm^2. The different numbers of laser pulses affect the modifications of silicon surfaces and the evolution processes of structures in laser interference lithography. The images present the laser ablation processes, and the physical processes can be described by Equations (5.22)-(5.29).

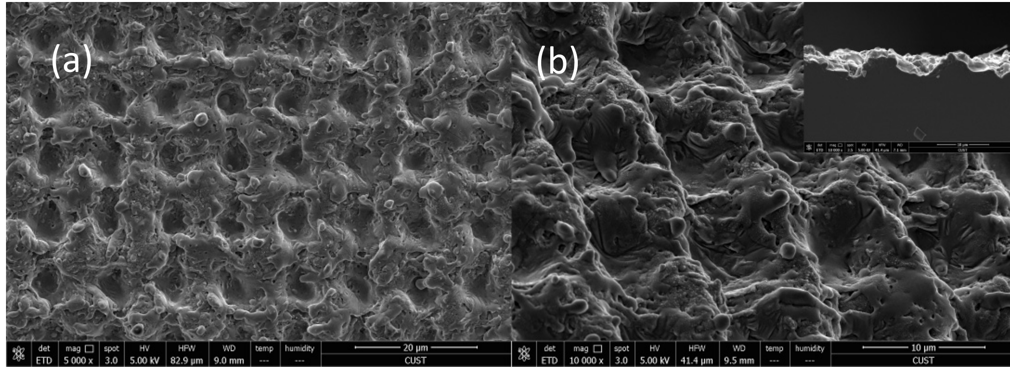

Figure 5.18 (a) SEM image (0°) and (b) SEM image (45°) of the pattern centres of the structures fabricated on the silicon wafer surface by four-beam laser interference lithography with 30 laser pulses.

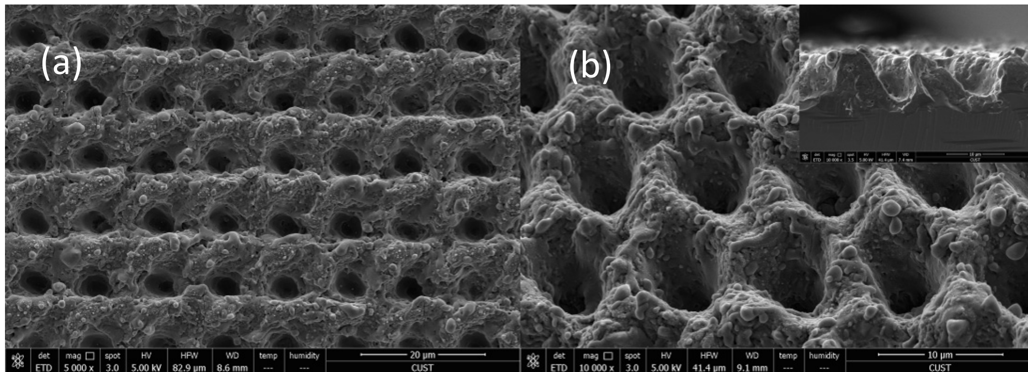

Figure 5.19 (a) SEM image (0°) and (b) SEM image (45°) of the pattern centres of the structures fabricated on the silicon wafer surface by four-beam laser interference lithography with 100 laser pulses.

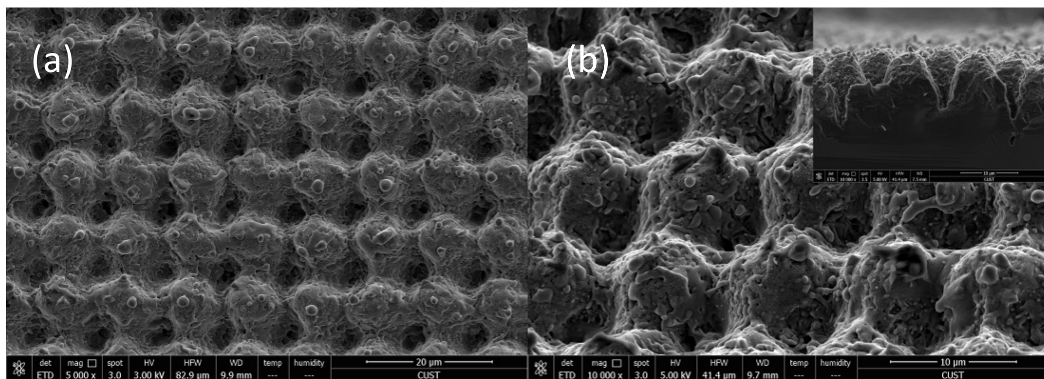

Figure 5.20 (a) SEM image (0°) and (b) SEM image (45°) of the pattern centres of the structures fabricated on the silicon wafer surface by four-beam laser interference lithography with 300 laser pulses.

In the case that the laser exposures were 30, an array of holes in the beam irradiation center were observed on the silicon wafer surface, as shown in Figures 5.18 (a)-(b). The average depth and diameter size of holes were about 5.5 μm and 5.8 μm. When the exposures were 100, an array of deep holes was observed on the silicon wafer surface, as shown in Figures 5.19 (a)-(b). The average depth of holes was about 8.9 μm, and the average diameter size of the holes was about 6.8 μm. When the exposures were 300, the depth of the holes became deeper and the diameter size also became larger. An array of cones was formed by the same conditions of four-beam laser interference, as shown in Figures 5.20 (a)-(b). The average depth of holes was about 13.8 μm and the average diameter size was changed to 7.8 μm. An array of holes was not evident and replaced by an array of cones on the silicon wafer surface due to the laser interference fluence having reached the threshold value of the silicon wafer. Thus, the surrounding materials of silicon micro holes have been etched and formed the array of cones on the silicon wafer surface. The theoretical diameter size on silicon wafer surfaces can be estimated with Equations (5.28) and (5.29) in the laser ablation process. Figures 5.18-5.20 were the SEM images obtained in the beam irradiation centre, and the theoretical diameter size was accordingly calculated. The theoretical diameters were obtained as 3.8 μm, 5.3 μm and 9.1 μm.

Figures 5.18-5.20 show the evolution process of the structures fabricated by four-beam laser interference on the silicon wafer surface. The process was due to the increase of the exposure pulses. It means that the laser energy accumulation is the result of the increase of laser impact on the silicon wafer surface. The increases of the depth and the diameter of the holes are due to that the four-beam laser interference intensity is higher than the silicon material threshold, as shown in Figures 5.11, 5.21 and 5.22. Figures 5.21 and 5.22 show that different energy accumulations of pulses can meet different demands of material modification thresholds for different shapes of features. Thus, different numbers of laser pulses can also affect the morphology of laser interference structures on the silicon wafer surface. Figure 5.23 shows theoretical and experimental results for the comparison of their radius sizes with laser pulses.

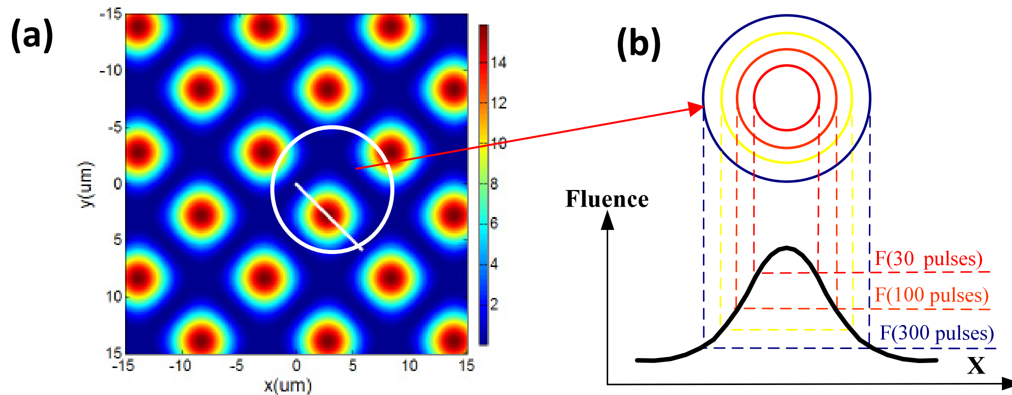

Figure 5.21 (a) The computer simulation of intensity distribution of four-beam laser interference, the incident angle was 5.5°, the azimuthal angles were 0°, 90°, 180° and 270°, and the polarization angles were 0°, 90°, 0° and 90°, and (b) The schematic profile of a single positive peak dot intensity distribution after the effect of four-beam interference with the laser pulses of 30, 100 and 300.

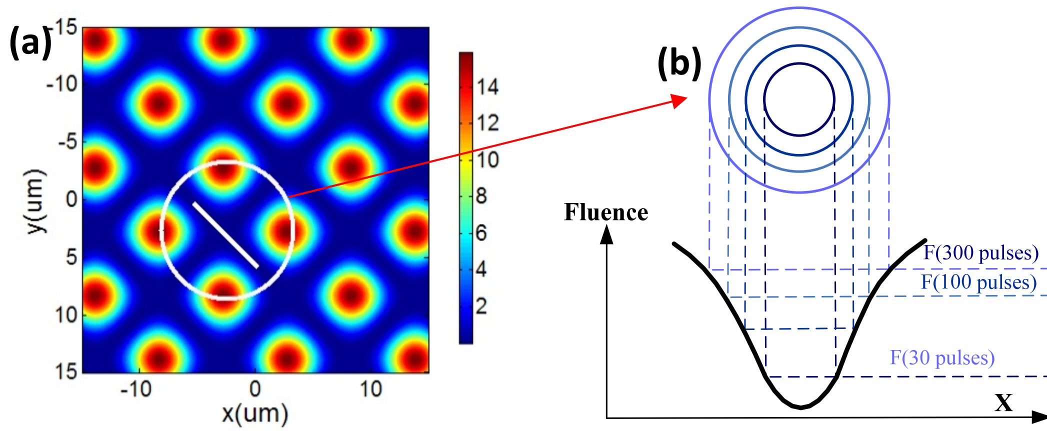

Figure 5.22 (a) The computer simulation of intensity distribution of four-beam laser interference, the incident angle was 5.5°, the azimuthal angles were 0°, 90°, 180° and 270°, and the polarizers were 0°, 90°, 0° and 90°, and (b) The schematic profile of a single negative peak dot intensity distribution after the effect of four-beam interference with the laser pulses of 30, 100 and 300.

Figure 5.24 shows the micro-nano silicon structures evolution with increasing numbers of laser pulses, from 1 to 200 and each SEM image shows a different expose sample. The samples were fabricated by four-beam laser interference lithography with the single laser fluences of 354 mJ/cm^2, the pulse repetition rate of 10 Hz, the laser wavelength of 1064 nm, the pulse duration of 7-9 ns and Figures 5.24(a)-(i) show the different laser pulses of 1, 2, 3, 4, 10, 12, 30, 50 and 200. From Figure 5.24, the effect of multiple laser pulses evolution with increasing numbers has been observed.

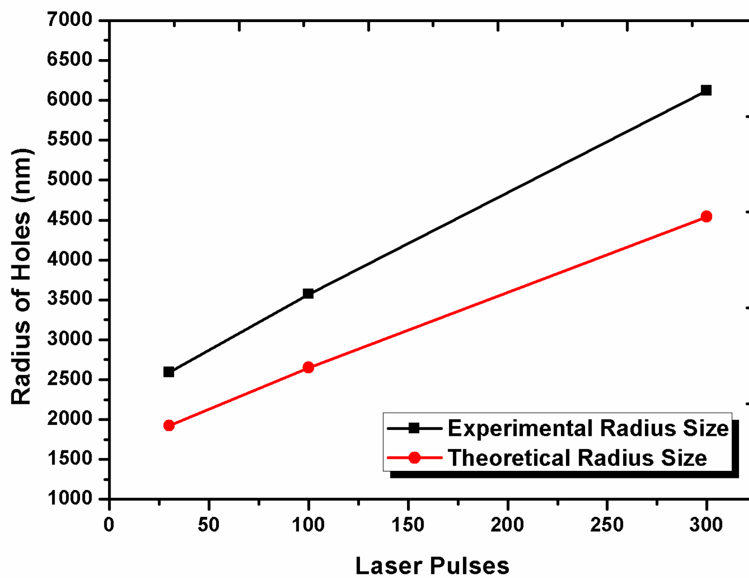

Figure 5.23 Theoretical and experimental results for the comparison of their radius sizes with laser pulses.

After the first laser pulse, an array of flower-like silicon structures appeared on the irradiated area, as show in Figure 5.24(a). The array of flowers consisted of a main silicon hole and many dots, and the structure of flower-like was very clear and obvious. With the second pulse, a large array of flower-like was observed on silicon wafer surface, as shown in Figure 5.24(b). The diameter size of the flowers was about 7770 nm, the diameter size of holes was about 3938 nm, and the diameter size of particles was about 834 nm and lots of particles homogeneously connected to the border of the holes. When the number of laser pulses was 3, an array of flower-like silicon structures changed larger and closed to each other, and the diameter size of the flowers was about 8691 nm, as shown in Figure 5.24(c). During pulses of 4, 10 and 12, as shown in Figures 5.24(d)-(f), the array of flower-like silicon structures transformed to an array of hole silicon structures. The flower structures were not evident and the size of hole structures changed deeper and larger. When the numbers of laser pulses were 30, 50 and 200, a clearly array of cones formed, as shown in Figures 5.24(g)-(i). The array of flower-like silicon structures had completely disappeared.

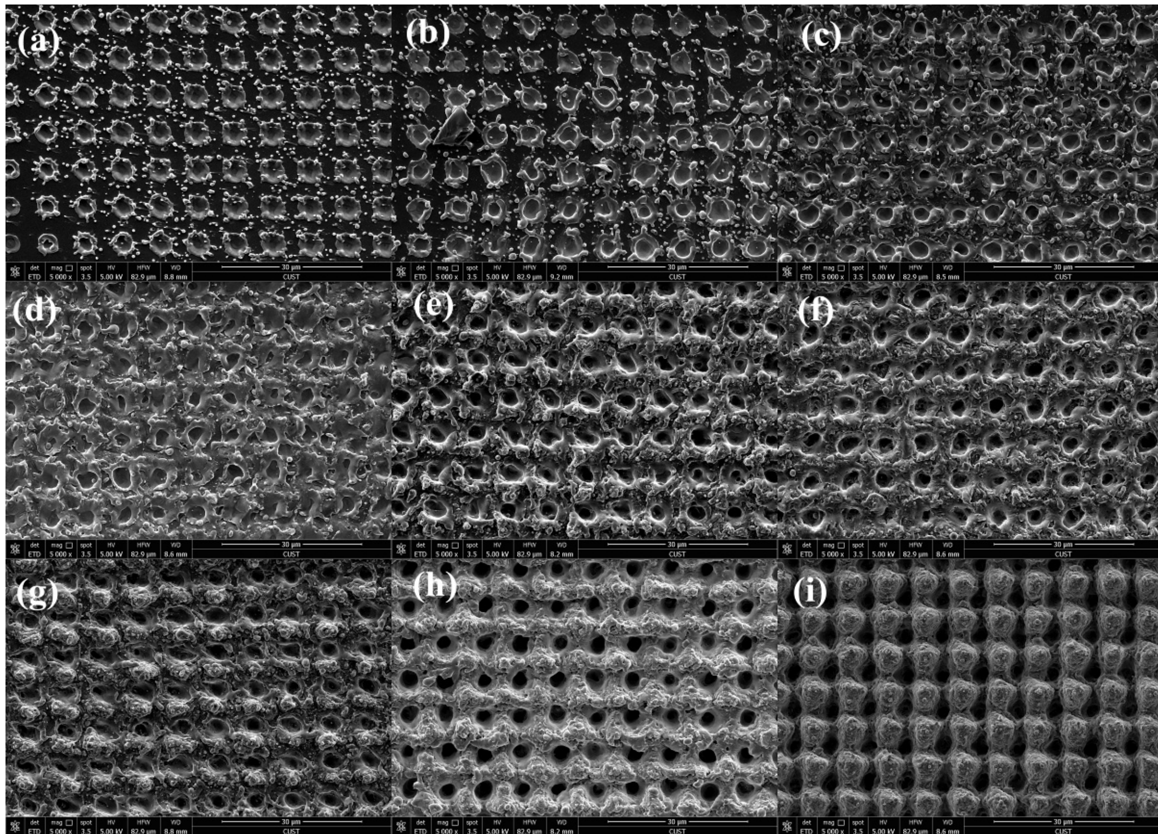

Figure 5.24 SEM images of flower-like silicon structures fabricated by four-beam laser interference lithography with the single laser fluences of 354 mJ/cm^2, the pulse repetition rate of 10 Hz, the laser wavelength of 1064 nm and the pulse duration of 7-9 ns. (a) is the one single laser pulse, (b) is the laser pulses of 2, (c) is the laser pulses of 3, (d) is the laser pulses of 4, (e) is the laser pulses of 10, (f) is the laser pulses of 12, (g) is the laser pulses of 30, (h) is the laser pulses of 50 and (i) is the laser pulses of 200.

In order to measure the reflectance, a Xenon-lamp, a spectrograph and an integrating sphere with a detector were used. Figure 5.25 shows that the reflectance of the pattern fabricated on the silicon wafer surface (blue curve) and the solar-weighted reflectance (*SWR*) is about 6.1 % in the wavelength range from 380 nm to 780 nm. The laser fluences are 637 mJ/cm^2 with 300 laser pulses generated by four-beam laser interference. For comparison, the reflectance of monocrystalline silicon solar cell surface (black curve in Figure 5.25) and polished silicon surface (red curve in Figure 5.25) were also measured and the *SWRs* are 8.9 % and 43.8 %, respectively. Thus, one of the applications corresponding to the patterns fabricated by four-beam laser interference is the antireflection surface of solar cells, and it is important to understand the effects of laser fluences on silicon modification for the fabrication of well-defined surface structures in a four-beam laser interference process.

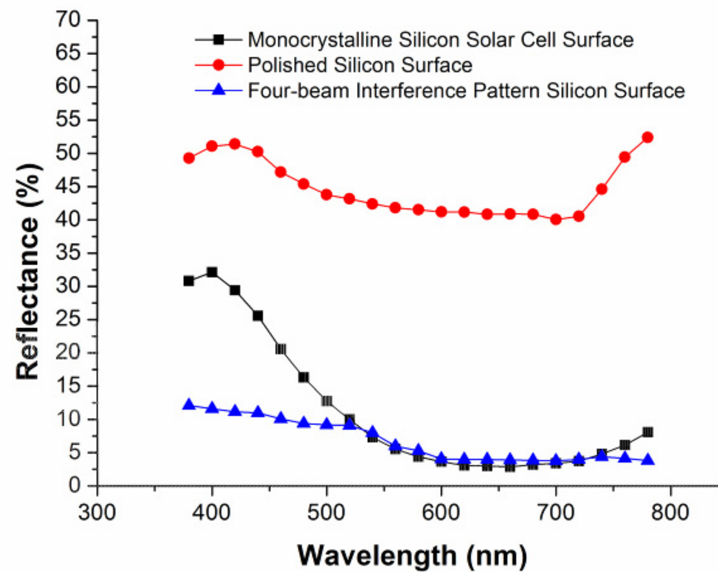

Figure 5.25 The reflectance of the four-beam laser interference patterned silicon surface (blue curve), the monocrystalline silicon solar cell surface (black curve) and polished silicon surface (red curve).

In this work, four-beam laser interference was used to pattern single crystal silicon wafers for the fabrication of various structures, and the numbers of laser pulses were applied to the process in the air. By controlling the parameters of laser irradiation, different shapes of silicon structures were obtained. The equations of heat flow and radiation effects of laser plasma of interfering patterns in a four-beam laser interference distribution were proposed to describe their impacts on silicon wafer surfaces. With the different laser fluences, several physical processes such as the formation of flower-like holes, dots and cones were discussed. The results indicate that the laser fluences have to be properly selected for the fabrication of well-defined surface structures in a four-beam laser interference lithography process.

5.6 Summary

In this Chapter, laser interference experiments with different laser parameters are carried out in order to show the effect of these parameters on the generation of several periodic structures and analyse the relationship of laser interference interaction with silicon. Effects of heat flow and radiation laser plasma of interfering patterns in a four-beam laser interference distribution are proposed. The resulting pattern with

different laser parameters can indicate that the laser fluences have to be properly selected for the fabrication of well-defined surface structures.

Chapter 6

One Step Fabrication of Triadic Hierarchical Silicon Architectures with Excellent Antireflection and Self-cleaning Properties

In nature, some biological surfaces, which are lotus leaves, rice leaves, butterfly wings, water strider legs, mosquito compound eyes, and red rose petals, present excellent properties arising from the cooperative interactions of hierarchical surface structures and chemical compositions. Thus, inspired by nature, lots of scientists have paid considerable attention to the design and fabrication of hierarchically structured micro and nano materials because of the wealth of enhanced properties for applications surface. Lee et al. developed a fabrication method that can produce hierarchical Structures on a polymer surface and have very good superhydrophobic Surfaces.[78] This biomimetic superhydrophobic surfaces have been fabricated by heat- and pressure-driven imprinting methods, obtaining of both nanostructures and microstructures cooperatively with the superhydrophobicity of the polymer surface on all thermoplastic polymers. Figure 6.1 schematically shows the fabrication process of biomimetic hierarchical surfaces comprising various nano- and microstructures. Yang et al. “describe a simple fabrication procedure for creating artificial hierarchical micro/nanopillars on silicon substrates” [79]. Herein, they describe “a simple fabrication procedure for creating hierarchical surfaces by combining nanosphere lithography, and also demonstrate that by controlling the height of the nano/micropillars, hierarchical surfaces with four contact states have been created” [79]. Figure 6.2 illustrates the fabrication processes for the hierarchical pillars. Wu et al. reported gecko foot-like hierarchical microstructures made of PDMS and obtained high surface roughness [80]. Figure 6.3 exhibits the fabrication scheme of gecko foot-like arrays. The resulting hierarchical surfaces have high roughness and exhibit extreme underwater

superoleophobicity, with a contact angle greater than 170° [80]. Therefore, many fabrication methods of hierarchical surface like desired the biological surfaces, in addition to the above, have been researched and obtained many excellent biological surface properties. However, one problem, the complex or multi-step in the fabrication process have not been solved, and affected the efficiency work, increased the fabricating cost, not be suitable mass production and so on.

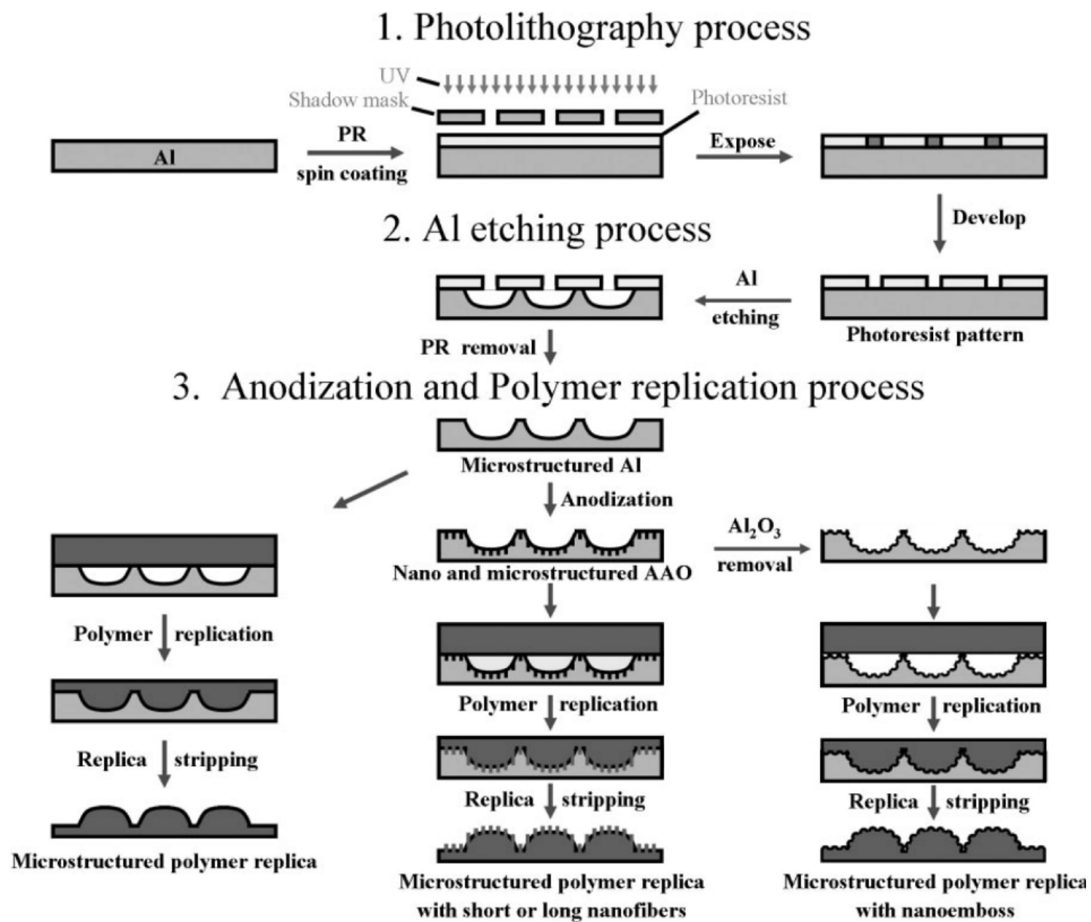

Figure 6.1. Scheme of fabrication process of hierarchical structures [79].

In this Chapter, One step fabrication of triadic hierarchical silicon architectures with excellent antireflection and self-cleaning properties can been shown. Using the three-beam direct laser interference lithography, only one step, can be achieved a triadic hierarchical silicon architectures. In the following section, a brief introduction of direct laser interference lithography has been explained. The second part views the generation micro and nano scale structures of focused laser pulse interaction with

silicon which are called laser-induced periodical surface structures (LIPSS). And then, the experimental procedures for a kind of triadic micro and nano structures have been exhibited. Then, the experimental details and results are presented though following results and discussion and achieved their antireflection and self-cleaning properties.

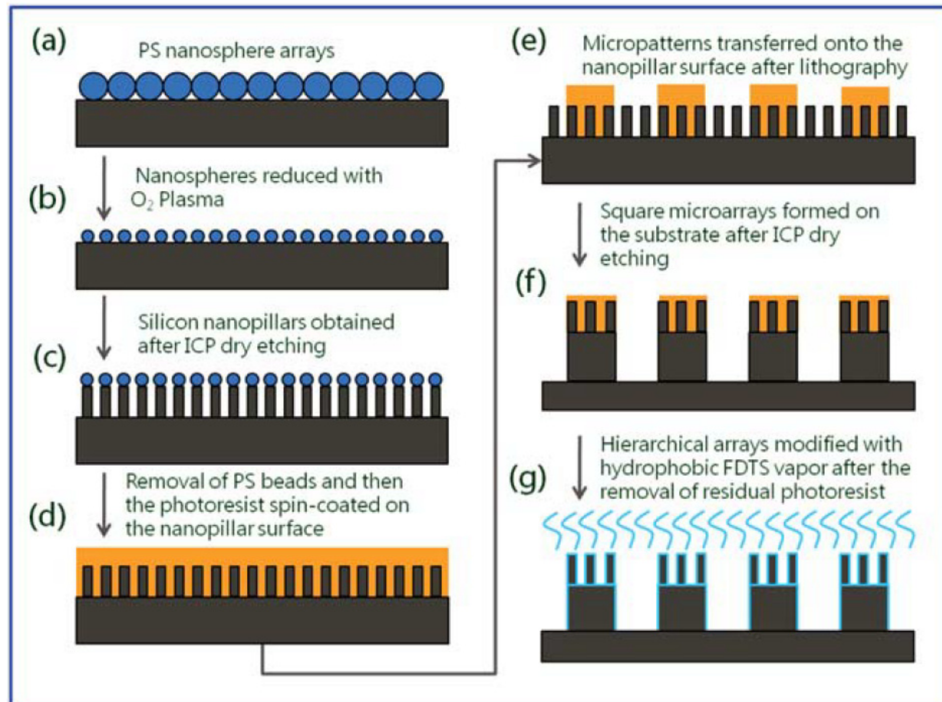

Figure 6.2 Schematic of the integrated fabrications for the hierarchical pillar-like surfaces on the silicon substrates [80].

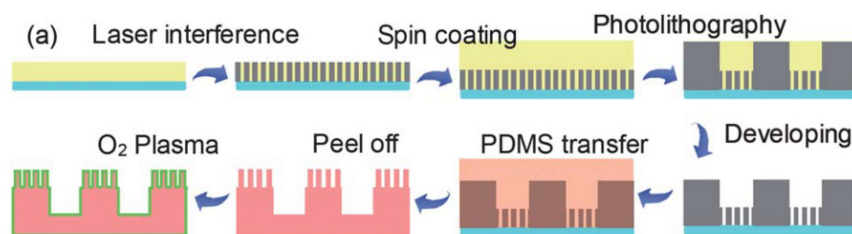

Figure 6.3 The fabrication scheme of gecko foot-like arrays [80] .

6.1 Introduction of Direct Laser Interference

Superficial texturing on silicon wafer is a great importance due to its applications for the fabrication of optical electronic devices and solar cells. The direct irradiation of silicon wafer using high power laser pulses can lead to various permanent surface micro and nano structures. This technology can produce the unique surface modifications and

has a considerable advantage of direct and single-step process, which allows a high production rate while no chemical residues are produced. Therefore, the direct high power laser pulses interaction with materials has attracted much interest by several research groups in order to fabricate regular structures on different materials surface, such as metals or semiconductors. However, there is not much evidence for fabrication the structuring of silicon by direct laser interference lithography. Such direct laser interference pattern has a possibility of fabricating high-resolution structures by interfering laser beams from a high-power pulsed laser.

Direst Laser Interference is a fabrication method of 1D, 2D and 3D structures interference patterning. Using this method, the material is exposed to a desired surface having the interference pattern, when the surface of the material is allowed by direct modification. Direct laser interference patterning usually uses high power light sources, such as Q-switched Nd:YAG lasers, to fabricate the periodic arrays because elevated laser fluences are required. Compared other technologies, such as nanoimprint, optical lithography or laser writing, only direct laser interference lithography, it is a very flexible method, can allow rapid large area fabrication in a single or multiple laser.

Direct laser interference lithography has the advantage of straightforward process without the mask or photoresist. This technology can fabricate various structures by two laser interference or multi-beam laser interference simultaneously and the periodicity of structures is generated by the interference distribution with maximum and minimum intensities, which can be controlled from micrometres to nanometres continuously by adjusting the laser parameters of incident angles and or wavelengths.
In summary, the advantage of direct laser interference lithography can be concluded as follows:

- ☐ High throughput
- ☐ Low cost
- ☐ Controlled periodicity

- Large area manufacturing
- Various materials including metals, polymers and ceramics
- Created structures in Planar surface and non-planar surface
- Fabricated three dimensional structures.

Therefore, direct laser interference lithography has a simple system and technological procedure and also has the advantages of high power laser pulses lithography. Thus, direct laser interference lithography is a promising technology for manufacturing of micro and nano structures and suitable for a large number of potential applications.

6.2 Overview of Focused Laser Pulse Interaction with Silicon

"Some of the important laser-induced morphological changes reported mainly are the formation of ripples and conical micro and nano structures formation" [81]. Since the early 1970's, the periodic surface ripples following laser irradiation have been reported by researchers [1]. The ripples have been named Laser Induced Periodic Surface Structures (LIPPS). They have small undulations on the surface of silicon and the undulations are spatial periods closely related to the central wavelength of the laser. Bonse et al. "investigated the initial modification and ablation of crystalline silicon with single and multiple Ti: sapphire laser pulses of 5 to 400 fs duration" [63]. Figure 6.4 shows the SEM picture of damage undulations with spatial periods on silicon wafer surface.

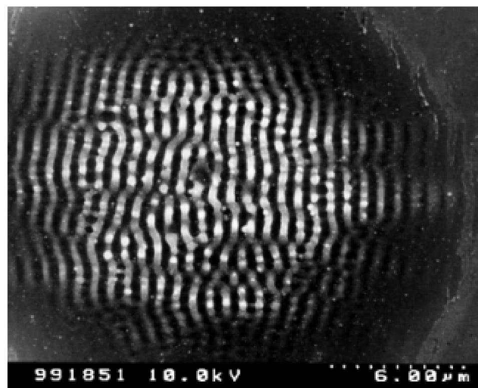

Figure 6.4 SEM image of damage in silicon generated with Ti: sapphire laser pulses in air [63].

Her. et al. “have reported the formation of conical microstructures on silicon in 1998” [82]. Silicon surfaces with an array of sharp conical spikes are fabricated by several hundred femtosecond-laser pulses in an atmosphere of sulphur hexaflouride (SF6). Figure 6.5 shows the conical microstructures formation on silicon.

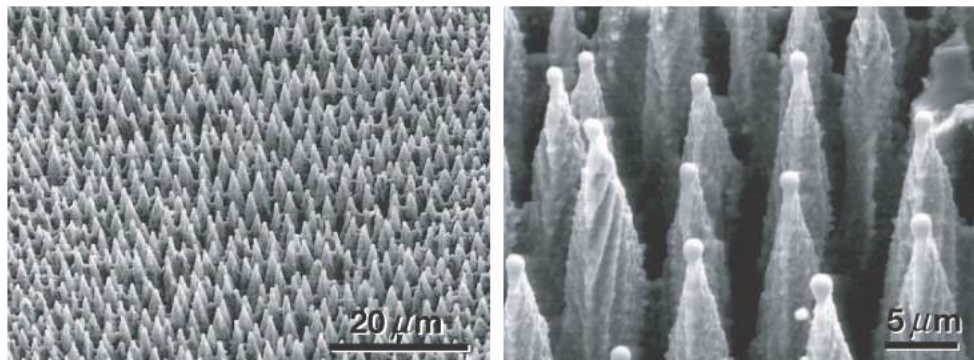

Figure 6.5 SEM images of typical surface morphologies for femtosecond-laser microstructured silicon at two magnifications. Both micrographs are taken at a 45° angle [82].

In the mid to late 1990’s, researchers began more exotic structure formation on silicon following laser irradiation [83, 84]. Sanchez et al. have studied the effects of ArF excimer laser irradiation on silicon single crystals and showed the whisker-like columns morphology. Figure 6.6 shows SEM microphotographs of whisker-like columns formed on silicon [83].

The unique morphology of microstructures is due to the condition of initial experiments and “ambient gas plays a critical role in the formation of sharp conical microstructures” [85]. These early experiments provided that “surfaces irradiated in nitrogen, helium, or vacuum have much blunter structures than surfaces structured in sulphur hexaflouride or chlorine” [85]. “black silicon” has been “obtained by femtosecond laser processing of crystalline silicon wafer surfaces in the presence of ambient gases SF_6 or Cl_2” [82]. Black silicon has an excellent antireflection property. The absorbance of Black silicon can be from near-ultraviolet to the near-infrared. It has generally been used on some potential applications such as solar cells.

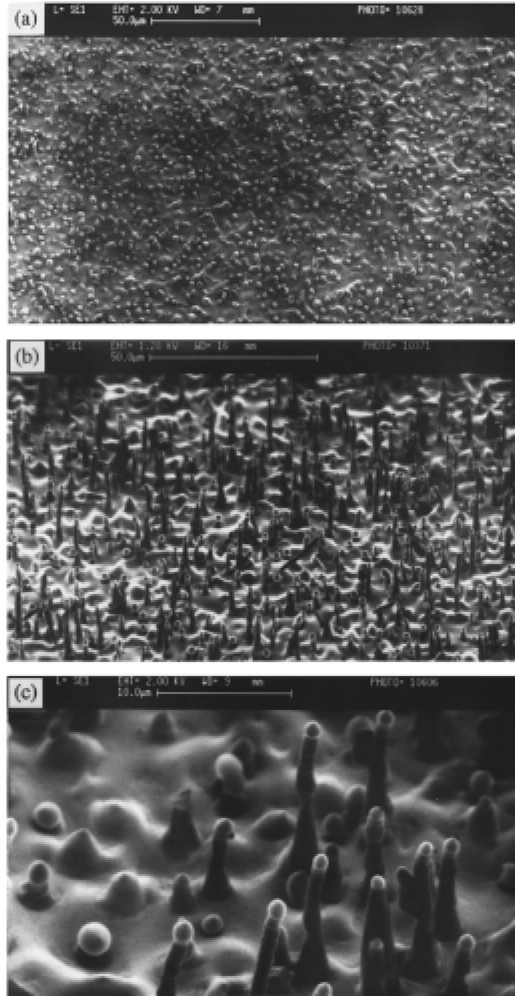

Figure 6.6 shows SEM microphotographs of whisker-like columns formed on silicon irradiated at 1.7 J/cm^2 with 500 laser pulses. (a) is a 10° view, (b) is a 45° view and (c) is a magnified view of (b) [83].

6.3 Experimental Procedures

The laser interference system used a seeded Q-switched Nd:YAG laser source with the wavelength of 1064 nm, pulse duration of 7-9 ns, Gaussian beam of 6 mm in diameter and the laser fluence of 531 mJcm^{-2}. The combination of 1⁄4 wave plates and polarizers w used to control the pulse energy level of single beams and the polarization direction of each beam. The substrates used in the experiments were single side polished monocrystalline silicon wafers with (100) orientation cleaved into small chips and ultrasonically cleaned with acetone and methanol.

One such chip is put on a stage, which is mounted on a high precision computer controlled X, Y stage. The interfering laser beams is focused along the normal onto the sample by 45° degree of total reflection mirror. The three-beam interference system,

the laser beam was divided into three beams with the same incident angles of 30°, the azimuthal angles of 0°, 120° and 240°, and the polarizers of 0°, 90°and 90° as shown in Tables 6.1. After the structures fabricated on the samples, a scanning electron microscope (SEM) was used to perform the measurements of the surface morphology structures.

Table 6.1 Beam configuration parameters for the selected interference pattern

Parameter	Beam 1	Beam 2	Beam 3
Angle of Incidence	30°	30°	30°
Azimuth	0°	120°	240°
Polarization	0°	90°	90°
Relative Intensity	1	1	1

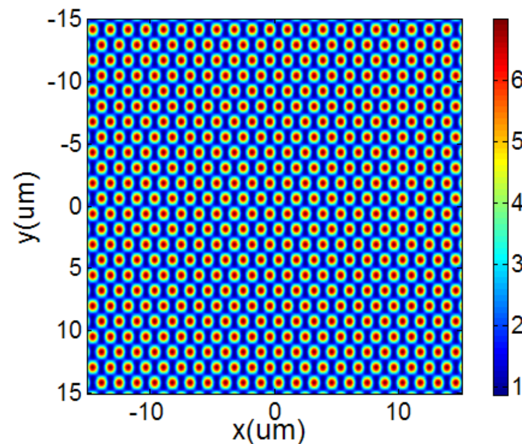

Figure 6.7 The computer simulation of three-beam laser interference.

6.4 Results and Discussions

The point discussions are focusing to the kind of structures fabricated by three-beam interference lithography of the incident angle of 30°. The laser fluence is maintained 531 mJ/cm^2, and the numbers of laser pulses are 30, 50, 200, 300, and 600. Figure 6.7 shows the computer simulation of three-beam laser interference with the incident angle of 30°. A hexagonally-distributed dot-like pattern is obtained and the side length of hexagonal period of intensity distributions is about 1.4 µm. However, after the multiple

exposure of three-beam laser interference with the incident angle of 30°, the interest phenomena have been observed by SEM. Figures 6.8 – 6.12 show the results obtained from the laser pulses of 30, 50, 100, 200, 300 and 600 with each laser fluence for all the samples was 531 mJ/cm^2. From these figures, it can be observed that there are different morphologies with the computer simulation. A kind of triadic micro and nano structures has been obtained. This kind structures is a randomly array of conical micro structures and a hexagonally-distributed holes having the maximum periods of 1.4 µm located on the conical micro structures. Moreover, some randomly nano dots structure evenly distributed on the conical structures with hexagonally-distributed holes and increased the function of its surface roughness, as shown in Figure 6.13 and Figure 6.14. How or why this kind of structures produced will be discussed in the following section.

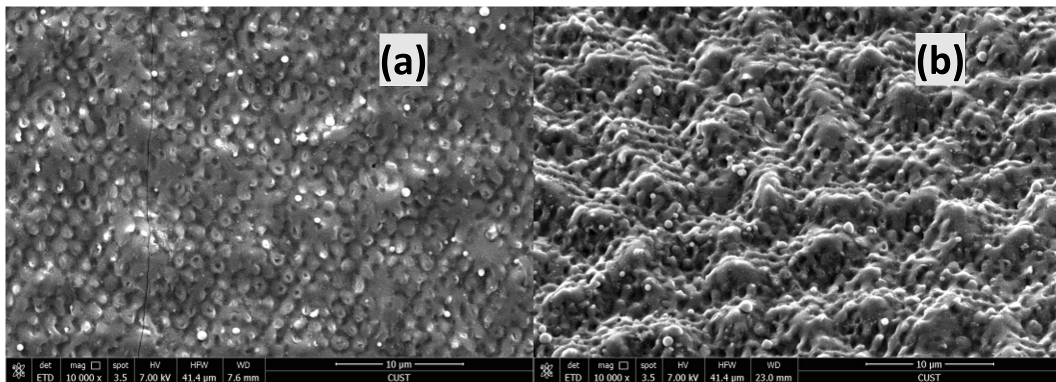

Figure 6.8 (a) SEM images (0°) and (b) SEM image (45°) of the pattern centres of the structures fabricated on the silicon wafer surface by three-beam laser interference lithography with 30 laser pulses.

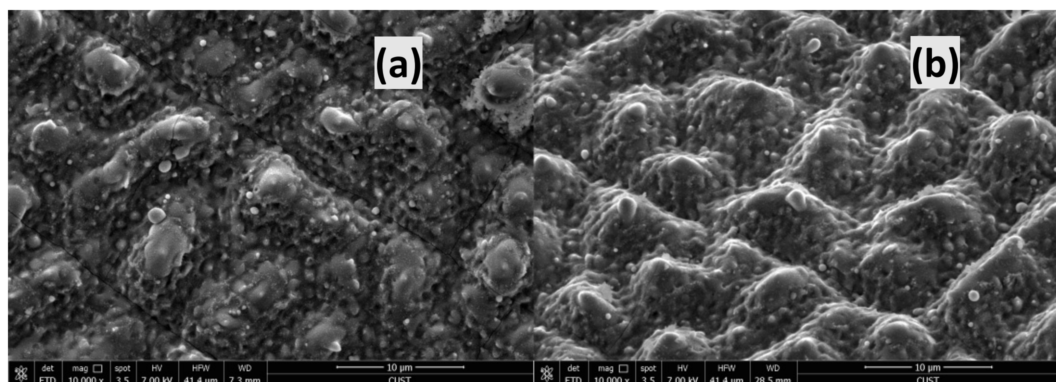

Figure 6.9 (a) SEM images (0°) and (b) SEM image (45°) of the pattern centres of the structures fabricated on the silicon wafer surface by three-beam laser interference lithography with 50 laser pulses.

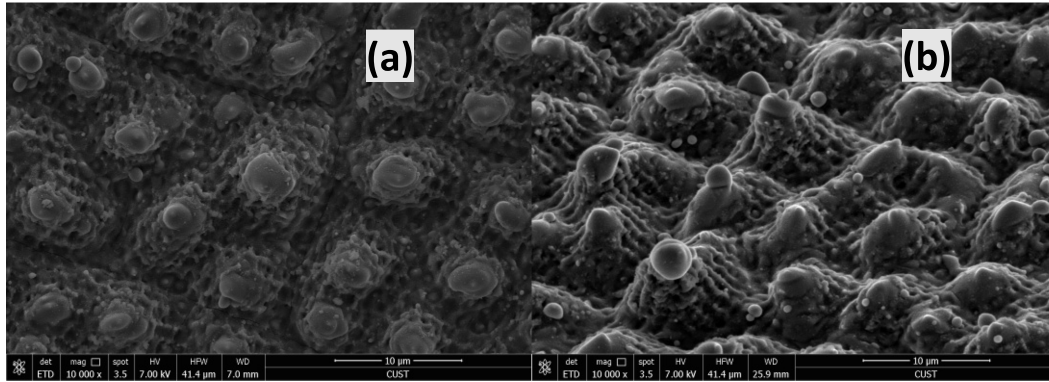

Figure 6.10 (a) SEM images (0°) and (b) SEM image (45°) of the pattern centres of the structures fabricated on the silicon wafer surface by three-beam laser interference lithography with 200 laser pulses.

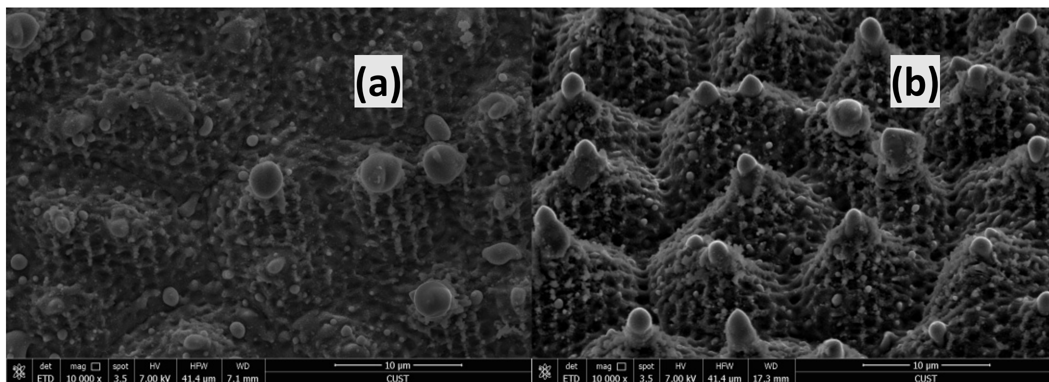

Figure 6.11 (a) SEM images (0°) and (b) SEM image (45°) of the pattern centres of the structures fabricated on the silicon wafer surface by three-beam laser interference lithography with300 laser pulses.

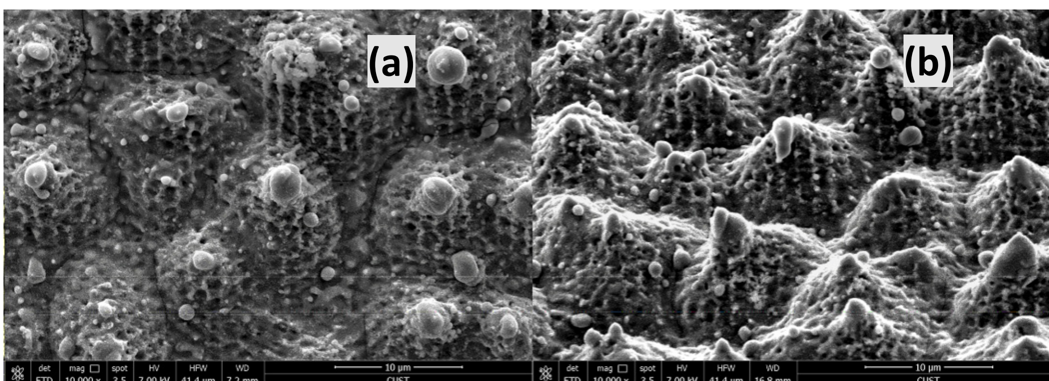

Figure 6.12 (a) SEM images (0°) and (b) SEM image (45°) of the pattern centres of the structures fabricated on the silicon wafer surface by three-beam laser interference lithography with 600 laser pulses.

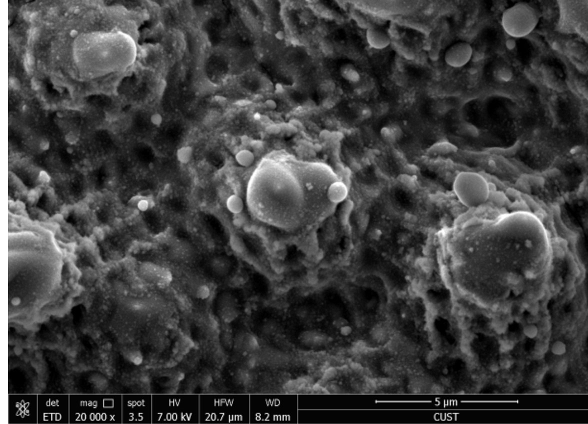

Figure 6.13 SEM image of some randomly nano dot structures evenly distributed on the conical structures with hexagonally-distributed holes using three-beam laser interference with 300 pulses.

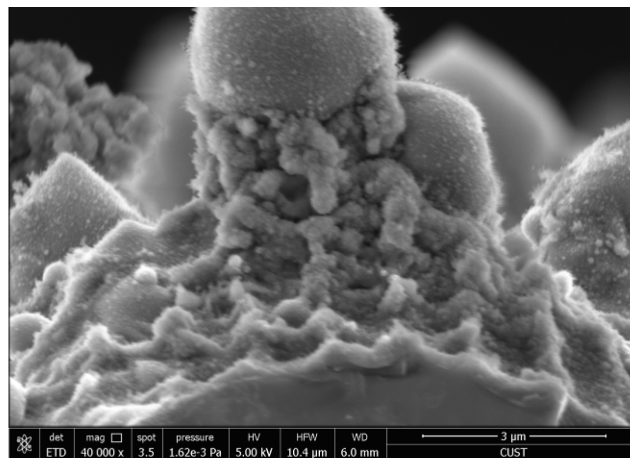

Figure 6.14 Cross Section of SEM image of some randomly nano dot structures evenly distributed on the conical structures with hexagonally-distributed holes using three-beam laser interference with 600 pulses.

Before this kind of structures is discussed, the micro and nano structures produced by laser interaction with silicon wafer must be introduced and the reasons of emergence of such the structures. From overview of focused laser pulse interaction with silicon in Section 6.2, the morphologies of ripples and conical micro and nano structures can be produced by laser pulse. For the reason of formation of these structures, almost two decades ago, Siegman et al. [86] reported that “ripples are readily formed on the material’s surfaces by a single short pulse with high fluence can enough cause some sort of phase transformation such as melting, vaporization, partial, or complete annealing”. It is explained that the formation of ripples is initiated by the scattering of a small amount of incident light by surface irregularities [86, 87]. Huang et al. [88] reported “the

formation of the sub-wavelength ripple in silicon wafer and attributed the formation reason to the interference between the incident laser beam and surface plasmons”. For the formation of conical micro and nano structures, it happens at the late stage of repetitive exposure of pulses “when the laser fluence is at or above ablation threshold and due to self-masking for the incident laser radiation. Light gets reflected from these angle shaped structures and ablates materials selectively” [81]. Nayak et al. [81] reported that the formation evolutions from micro and nano ripples to conical structures and systematic explained their formation reason and obtained the following conclusions.

- ☐ The morphologies of ripples and conical micro and nano structures are self-organized formation on silicon wafer surface irradiated by multiple ultrafast laser pulses.
- ☐ “With subsequent exposures, ripples structures are formed, and its periods are in the order of laser wavelength possibly arising due to scattering centres and are found to be oriented in arbitrary directions” [81].
- ☐ “Finally, ripples break down due to the continuous formation of circular surface waves and conical micro/nano structures start appearing along the ripple. These structures are further developed due to self-masking for the incident laser radiation. Light gets reflected from these angle shaped structures and ablates materials selectively” [81].

In the case that laser pulses were 30, an array of hexagonally-distributed holes in the beam irradiation centre were observed on the silicon wafer surface, as shown in Figures 6.8 (a)-(b). The diameter size of hexagonally-distributed holes was about 1.4 µm, which was the same as the computer simulation. From Figure 6.8(b), a lot of localized projections emerge from the surface of hexagonally-distributed holes and the height of the projections was about 3885 nm as shown in Figure 6.15. By increasing the number of laser pulses to 50 and 200, the height of projections increase to about 6286 nm and 6750 nm as, respectively. When the exposures were 300, the projections change larger and higher, and the random conical structures were formed. The height of cones was

increased to 10880 nm as shown in Figure 6.15. Thus, the height of the cones grows with an increasing number of laser pulses. The reason of the growing of conical structures could be explained that the self-organized formation on silicon wafer surface irradiated by multiple nanosecond laser pulses. The size of the conical structures is according to the numbers of exposure pulses and the development of conical structures is due to self-masking for the incident laser radiation [81]. Light have be reflected from these angle shaped structures and ablates materials selectively. The formation of hexagonally-distributed holes is surely due to direct three-beam laser interference on the silicon wafer surface. Therefore, both mechanisms lead to the occurrence of this phenomenon.

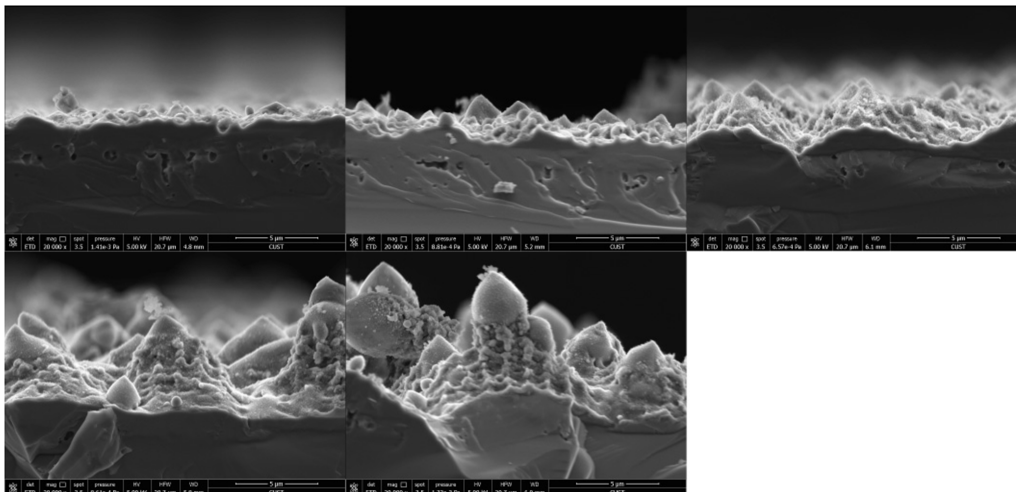

Figure 6.15 Cross Section of SEM image of some randomly nano dot structures evenly distributed on the conical structures with hexagonally-distributed holes using three-beam laser interference, (a) is 30 pulses, (b) is 30 pulses, (c) is 50 pulses, (d) is 200 pulses, (e) is 300 pulses, (d) is 600 pulses.

6.5 Optical and Hydrophobic Properties Measurements

For reflectance measurements, samples are carefully put on the sample stage with a window for support. The window placed on integrating sphere is used because the incident light can irradiate on the sample surface through the access ports of the integrating sphere and then reflect back into the integrating sphere detector. The operational wavelength range of monochromator is 250 nm to 2500 nm. The incident light from xenon lamp sources, which is similar to the sunlight spectrum, is sent into a

monochromator that selects a single wavelength and directs it onto a sample. Then, the relative curves are measured as demonstrated in the Chapter 3. Due to the band-gap energy of crystalline silicon is 1.07 eV, the absorptance for crystalline silicon is corresponded to near 1100 nm. The energy of sunlight is mainly at the visible light range, which is the wavelength from 300nm to 800nm. Thus, the reflectivity of the wavelength range from 300 to 800 for silicon wafer has been concerned.

To investigate the effective reflections of the two different regular structures on silicon wafer surfaces, the light source of solar irradiation (*AM1.5G*) and the spectrograph equipped with an integrating sphere were used in the experiment [63, 89]. The solar-weighted reflectance (*SWR*) can be calculated by

$$SWR = \frac{\int R(\lambda) N_{photon} d\lambda}{\int N_{photon} d\lambda} \qquad (6.1)$$

where $R(\lambda)$ is the reflectance, λ is the wavelength and N_{photon} is the photon number of *AM1.5G* per unit area per unit wavelength.

For hyophobic properties measurements, increasing roughness of the surface is one way to improve the hydrophobicity of the surface, and the roughness surface fabrication has become a subject to be investigated. The roughness has been used to assess the wettability in order to design the superhydrophobic surface [90]. As the silicon was oxidised during the etching process in the air, the silicon wafer surface was covered a layer of Silica. Silica has the hydrophilic performance with the hydroxy on the silica surface. Thus, the fabricated structures were processed with HF to remove silica in this case. The process can be described by

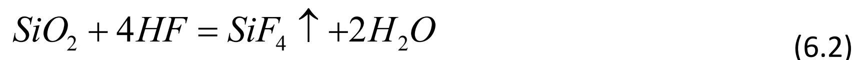

$$SiO_2 + 4HF = SiF_4 \uparrow + 2H_2O \qquad (6.2)$$

Thereby the silica was generated and it adhered to the interfering structures during the lithography process. In order to wipe off it and the dust on the surface, the samples were immersed in hydrofluoric acid with a concentration of 5% for 1 minutes.

After the laser interference and the removed silica process, the micro and nano structures have the hyophobic properties.

6.5.1 Optical Measurements

In the experiment, the laser pulses of 30, 50, 200, 300 and 600 were chosen to analyse the AR performance of structures. Figure 6.16 shows the reflectance of the samples in the visible spectrum obtained as solar cells mainly absorbed the light in that range. From Figure 6.16, the reflectance decreases over the wavelength range from 380 to 780 following the number of laser pulses increases. In the experiment, the laser pulses of 30, 50, 200, 300 and 600 were chosen to analyse the AR performance of structures. Figure 6.17 shows the SWR curves of different laser pulses. With the number of laser pulses increased, the SWR of the conical structures silicon surface with hexagonally-distributed patterns was decreased from 9.1% to 3.4% in the wavelength range from 380 nm to 780 nm and the lowest SWR was obtained by the laser exposures of 600. Figures 6.16 and 6.17 should be noted that this kind of structures has good antireflection property.

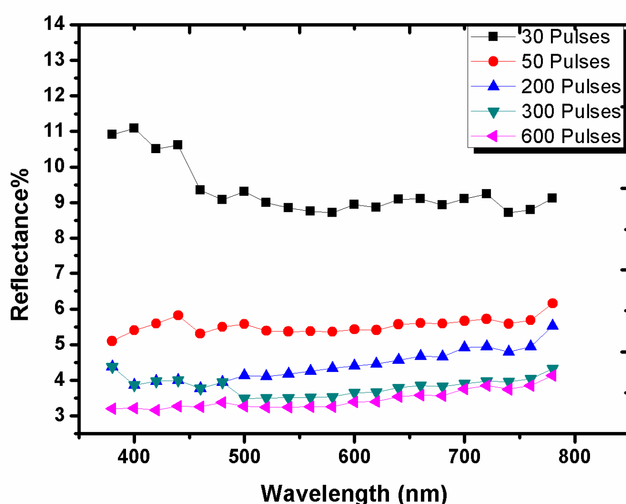

Figure 6.16 The reflectance of the samples irradiated by three-beam laser interference with laser pulses of 30, 50, 200, 300 and 600 in the visible spectrum range from 380 to 780.

6.5.2 Hydrophobic Properties Measurements

The hydrophobic properties of triadic micro and nano structures fabricated by three-beam laser interference lithography have been examined. Figure 6.18 shows the contact angle of conical micro structures with hexagonally-distributed silicon patterns as a function of the number of pulses. (a)-(d) are water droplets with a contact angle for hexagonally-distributed patterns fabricated by three-beam laser interference with laser

exposures of 30, 50, 100 and 300, respectively. For the micro and nano roughness structures, Cassie-Baxter model is used to explain the sample surface results [53]. Dong et al. reported a significant improvement of oil contact angle and presented distinct adhesive behaviours, adhesive force, can explain the hydrophobic properties [80]. It reveals that the performance of hydrophobicity is better when the measurement value of adhesive force is greater, and inversely the performance of hydrophobicity is bad when the measurement value of adhesive force is low. Thus, Figure 6.12 shows the SEM images of conical micro structures with hexagonally-distributed silicon patterns fabricated by three-beam laser interference with laser pulses of 600. Figure 6.19 shows the video screenshot of hydrophobic measurement process. It proves that the conical micro structures with hexagonally-distributed silicon patterns have excellent surperhydrophobic properties. Therefore, the sample of optimum reflectance condition also has excellent surperhydrophobic properties achieve improved efficiency and realize the functions of self-cleaning and antireflection.

6.6 Summary

This Chapter demonstrates a fabrication method about one step can fabricate a triadic hierarchical structures on silicon wafer surfaces with antireflection and hydrophobic properties fabricated. In this work, such triadic hierarchical structures is consist of a randomly array of conical micro structures, a regular hexagonally-distributed holes having the maximum periods of 1.4 μm located on the conical micro structures and some randomly nano dots structure evenly distributed on the conical structures with hexagonally-distributed holes. a three-beam laser interference system was set up to generate periodic micro-nano hole structures with hexagonal distributions. Excellent antireflection and hydrophobic properties have been observed and the results have shown the solar-weighted reflectance (SWR) (3.4%) in the wavelength range of 300 nm to 780 nm and larger contact angle (147°) providing with a self-cleaning capability on the solar cell surface.

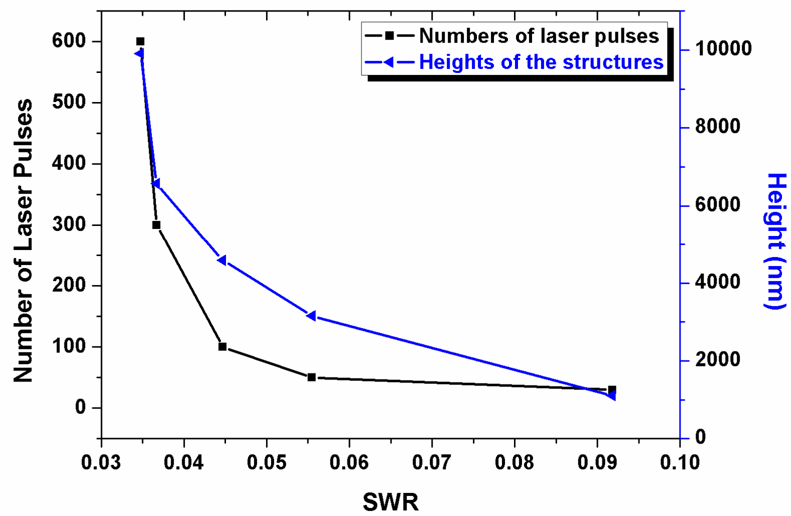

Figure 6.17 The numbers of laser pulses as a function of calculated SWRs.

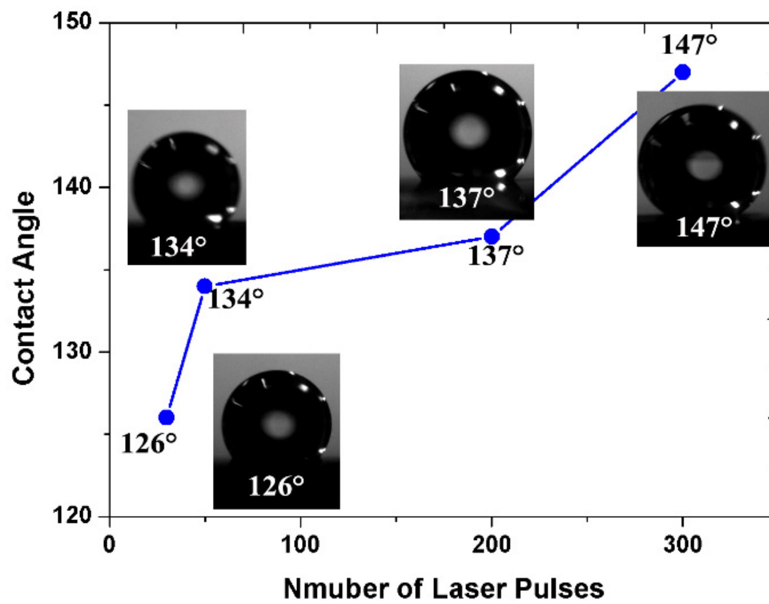

Figure 6.18 The numbers of laser pulses as a function of calculated SWRs.

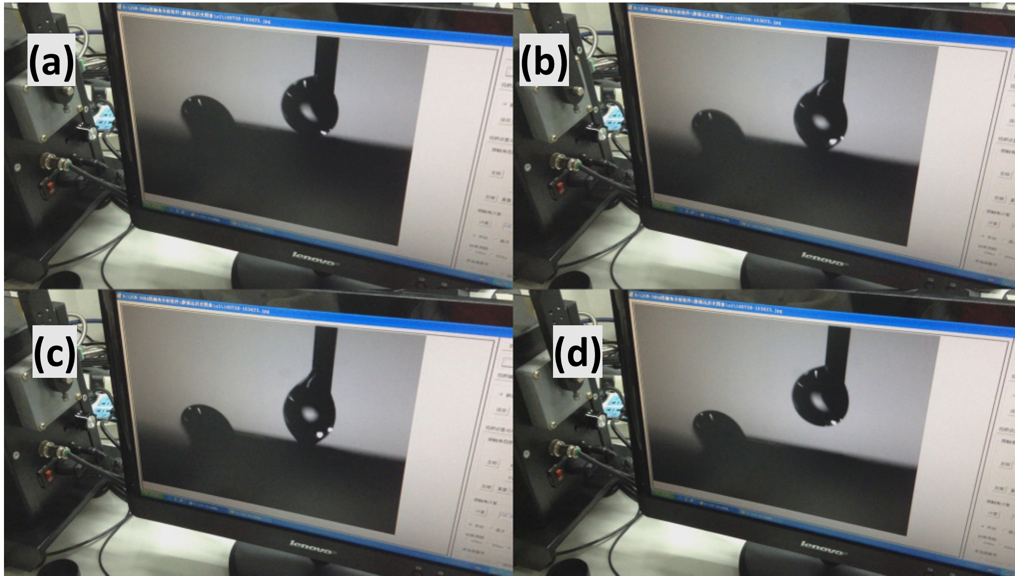

Figure 6.19(a) Video screenshots of hydrophobic measurement process from (a) to (d).

Chapter 7
Superhydrophobic Micro and Nano Dual Structures Fabricated by Direct Laser Interference Lithography

This Chapter presents a method for the fabrication of highly-ordered superhydrophobic micro and nano dual structures on silicon by direct laser interference lithography (LIL). The method offers its innovation that the superhydrophobic micro and nano dual structures can be fabricated directly by controlling the process of four-beam laser interference. Different laser fluences, exposure durations and cleanout times have been investigated to obtain the optimum value of the contact angle (CA). The superhydrophobic surface with the CA of 153.2° is achieved after the exposure of 60 s. Compared with other approaches, it is a facile and efficient method with its significant feature for the macro scale fabrication of highly-ordered superhydrophobic micro and nano dual structures on silicon.

7.1 Experimental Procedures

In the experiment, highly-ordered hydrophobic structures were fabricated by laser lithography technology based on four-beam interference. Single crystal p-doped (100) and polished silicon wafers with the electrical resistivity of 10 Ωcm were used. The laser source was a high-power pulsed Nd:YAG laser with the wavelength of 1064 nm, frequency of 10 HZ and pulse duration of 7 ns. In the experiment, the beam configuration parameters for selected interference pattern are shown in Table 7.1 and the computer simulation is shown in Figure 7.1. The energy of each interference beam was measured by laser power and energy meter (Coherent LabMax-top). The hydrofluoric acid with a concentration of 5% was prepared to immerse the patterned silicon for 3 minutes. The contact angle measurement was made by a contact angle system JGW-360A.

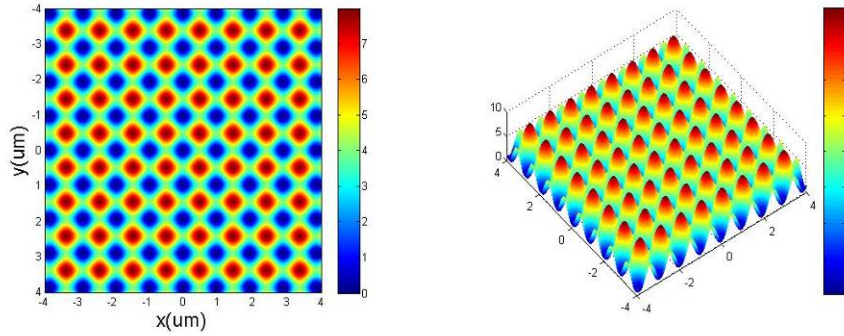

Figuer 7.1 2D and 3D plots of four-beam laser interference simulation results.

Table 7.1 Beam configuration parameters for the selected interference pattern

Parameter	Beam 1	Beam 2	Beam 3	Beam 4
Angle of Incidence	5.6	5.6	5.6	5.6
Azimuth	0	90	180	270
Polarization	90	90	90	90

7.2 Results and Discussions

Figure 7.2 shows the typical scanning electron microscope (SEM) images of the result silicon after exposure and immersion procedures. Micro and nano dual structures are formed obviously. These hierarchical structures are regarded to the critical reason for the functional surface. It can be seen from Figure 7.2 (b) that the period of dots is about 5.5 μm, which is a good agreement with theoretical analysis.

In the experiment, laser fluence, exposure duration T_e and cleanout time T_c have a strong influence on the CA. The superhydrophobic surface can be obtained with proper values of them. Since the threshold of silicon ablation depends on the energy of single pulses to a great extent, influences of different fluences need to be investigated. The results are shown in Table 7.2.

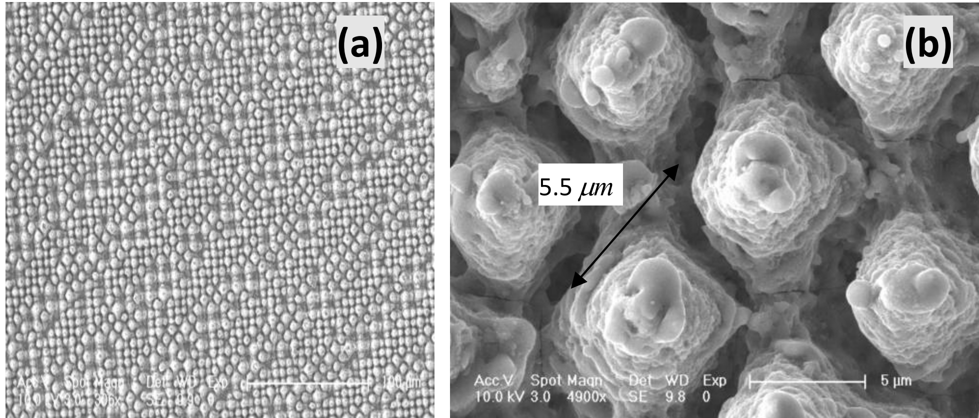

Figure 7.2. (a) SEM image (low magnification) of the micro and nano dual structures fabricated by four-beam laser interference. (b) Close-up image of micro pine trees at high magnification.

Table 7.2 Different fluences versus the contact angles on the result substrate.

Samples	Fluences	Exposure durations	Contact angles
1#	0.64 J/cm^2	60s	153.2°
2#	0.71 J/cm^2	60s	150.4°
3#	0.92 J/cm^2	60s	144.4°

The exposure duration also has the effect on the height of the periodic patterns. The samples which have been processed with different exposure durations of interference beams were characterized with SEM, as shown in Figure 7.3. The height in Figure 7.3 (a) is 2-3 μm and it is 10-14 μm in Figure 7.3 (c). The structure height will decrease the fraction of the solid area and result in increasing the CA. Within a range of laser fluences, the structure height will increase with the exposure duration. Finally, the superhydrophobic surface was obtained with the process parameter: T_e =60s and T_c =3min.

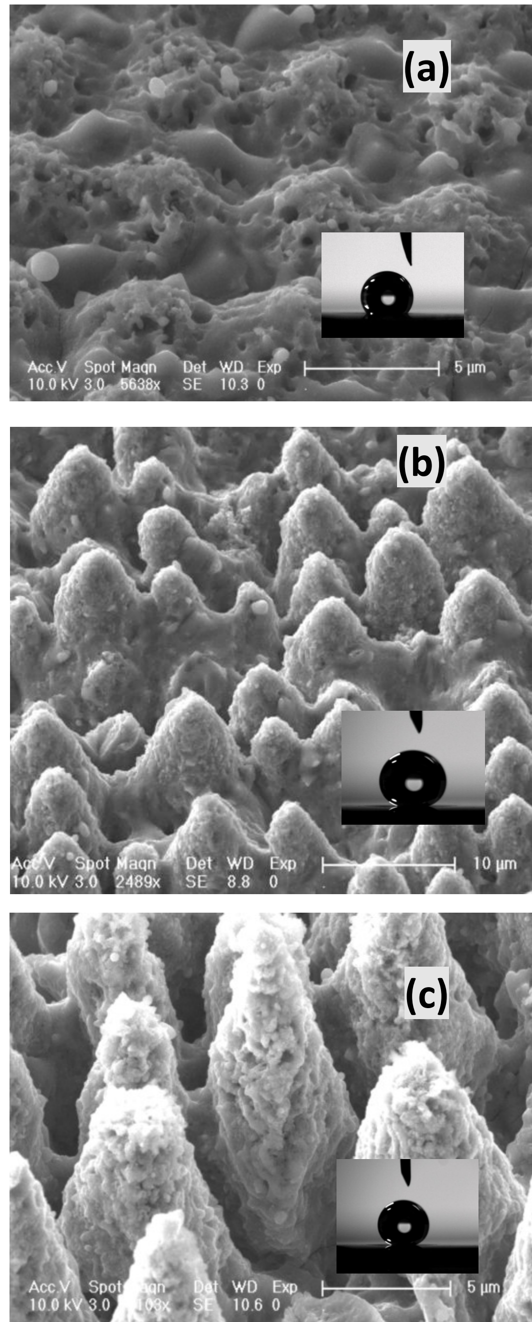

Figure 7.3 SEM microstructures and contact angle measurement of the silicon samples: (a) T_e =20s, CA=125.8°; (b) T_e =30s, CA=145°; (c) T_e =60s, CA=153.2°.

Chapter 8

Antireflection Silicon Structures with Hydrophobic Property Fabricated by Three-beam Laser Interference

This Chapter demonstrates antireflective structures on silicon wafer surfaces with hydrophobic property fabricated by three-beam laser interference. In this work, a three-beam laser interference system was set up to generate periodic micro-nano hole structures with hexagonal distributions. Compared with the existing technologies, the array of hexagonally-distributed hole structures fabricated by three-beam laser interference reveals a design guideline to achieve considerably low solar-weighted reflectance (SWR) in the wavelength range of 300 nm to 780 nm. The resulting periodic hexagonally-distributed hole structures have shown extremely low SWR (1.86%) and relatively large contact angle (140°) providing with a self-cleaning capability on the solar cell surface.

8.1. Introduction

To fabricate solar cells with high conversion efficiency, reduction of the surface reflection is very important. Antireflection coating (ARC) technology is one of the effective methods to achieve high conversion efficiency for crystalline silicon (c-Si) solar cells. There are currently various chemical and physical technologies used to modify or pattern silicon wafers for the fabrication of antireflection (AR) surfaces. Alkaline solutions were used to produce a random pyramid texture on crystalline silicon, and silicon nitride (SiNx) thin films were fabricated by plasma enhanced chemical vapour deposition (PECVD) [11, 91]. However, these methods have the disadvantages of complexity, high cost and more pollution. Recently, periodic subwavelength scale structures have attracted considerable attention, due to their promising antireflection properties to minimize reflection losses. However, they are expensive, only suitable for small area or flat surface applications. Laser interference lithography (LIL) is a potential

technology that can produce regular micro-nano structured patterns on silicon wafers for solar cells. This is a simple maskless low-cost and high throughput technology for producing periodic and quasi-periodic silicon structures. Up to now, many efforts have been devoted to study or fabricate micro-nano structures for different applications using LIL. Senthuran et al. reported “a maskless and scalable technique for fabricating nano-scale inverted pyramid structures suitable for light management in crystalline silicon solar cells” [92]. Zhang et al. fabricated “periodic antireflection structures with the average reflectance of 3.5% on silicon using four-beam laser interference lithography” [41]. Wang et al. proposed both antireflection and superhydrophobic structures fabricated by direct laser interference nanomanufacturing and the contact angle and reflectance were 156.3° and 5.9-15.4% [42]. Li et al. presented a method for the fabrication of highly-ordered superhydrophobic micro-nano dual structures on silicon by direct laser interference lithography [93]. The antireflection and self-cleaning functions were due to the formation of an array of micro cone and hole structures on silicon wafer surfaces. Theoretically, using four-beam laser interference method could evenly generate squarely-distributed periodic structure patterns with the antireflection and self-cleaning functions on silicon wafer surfaces, “but in practice, noticeable modulations were almost unavoidably introduced in interference patterns due to the misalignment of incident angles or unequal incident angles” [94], which is not desired. In contrast to four-beam laser interference, the modulation phenomenon of three-beam laser interference method is not evident, which can avoid the generation of uneven interference patterns and produce the accurate regular interference patterns to ensure the pattern consistency. In addition, the antireflection characteristics of silicon micro-nano structures, fabricated by three-beam laser interference with a hexagonally-distributed array of structures, have not been investigated. Thus, it is worthwhile to study the silicon micro-nano structures to achieve the desirable antireflection silicon structures with hydrophobic property for solar cell applications.

In this work, a three-beam laser interference system was set up to generate periodic micro-nano hole structures with hexagonal distributions. The resulting periodic

hexagonally-distributed hole structures have shown extremely low SWR (1.86%) in the wavelength range from 300 nm to 780 nm and relatively large contact angle (140°) providing with a self-cleaning capability on the solar cell surface.

8.2. Highlights

- A three-beam laser interference system was built to generate periodic micro-nano hole structures with hexagonal distributions.
- Silicon surfaces were directly modified by laser interference.
- The array of hexagonally-distributed hole structures can achieve considerably low solar-weighted reflectance.
- The resulting periodic hexagonally-distributed hole structures have shown relatively large contact angle providing with a self-cleaning capability.
- In contrast to four-beam laser interference, the modulation phenomenon of three-beam laser interference is not evident, which can avoid the generation of uneven interference patterns.

8.3. Experiment

The laser interference system used a seeded Q-switched Nd:YAG laser source with the wavelength of 1064 nm, pulse duration of 7-9 ns, Gaussian beam of 6 mm in diameter and the laser fluence of 637 $mJcm^{-2}$. The combination of 1/4 wave plates and polarizers were used to control the pulse energy level of single beams and the polarization direction of each beam. The substrates used in the experiments were single side polished monocrystalline silicon wafers with (100) orientation. For the four-beam interference system, The laser source was divided into four beams with the same incident angles of 5.5°, the azimuthal angles of 0°, 90°, 180° and 270°, and the polarizers of 0°, 90°, 0° and 90°. For the three-beam interference system, the laser beam was divided into three beams with the same incident angles of 5.5°, the azimuthal angles of 0°, 120° and 240°, and the polarizers of 0°, 90°and 90°. After the structures fabricated on the samples, a scanning electron microscope (SEM) was used to perform the measurements of the surface morphology structures. A contact angle measurement system was used to obtain

the contact angles of the silicon micro and nano structures. In order to measure the reflectance, a Xenon-lamp, a spectrograph and an integrating sphere with a detector were used.

8.4. Results and Discussions

The results of the direct modification of silicon surface by nanosecond laser interference lithography were discussed in this section.

Laser interference fluence can produce different patterns on the silicon wafer surface with different laser parameters. The intensity distribution patterns of laser interference are dependent on the number of laser beams, the incident angles, the azimuth angles and the polarization directions. Figure 8.1 shows Matlab simulation results of the two patterns obtained by three-beam and four-beam laser interference with the same incidence angles of 5.5°. For the three-beam laser interference, a hexagonally-distributed dot-like pattern is obtained and the side length of hexagonal period of intensity distributions is about 7.5 μm, as shown in Figure 8.1(a). For the four-beam laser interference, a squarely-distributed dot-like pattern is produced and the side length of squarely-distributed period of intensity distributions is about 8 μm, as shown in Figure 8.1(b).

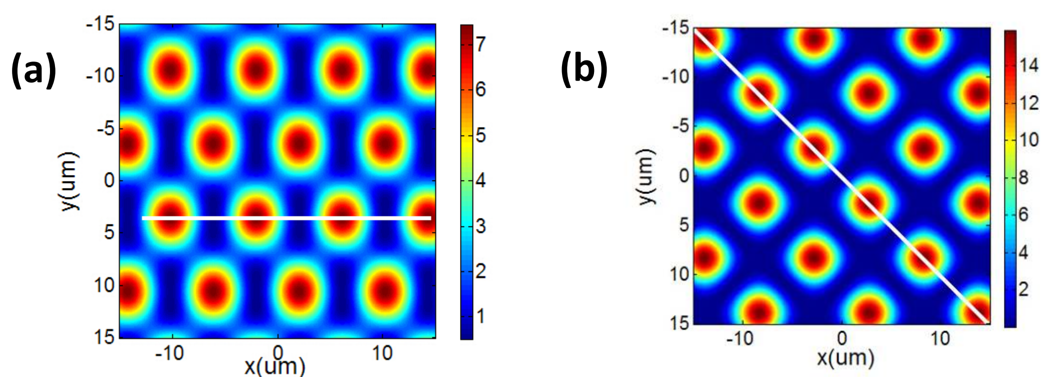

Figure 8.1 Simulation of intensity distributions of multi-beam interference with incidence angles of 5.5°, (a) three-beam laser interference and (b) four-beam laser interference.

Figure 8.2 shows scanning electron microscope (SEM) images of silicon micro and nano structures created by three-beam interference patterning (Figures 6(a)-(d)) and four-beam interference patterning (Figures 8.2(d)-(h)) on silicon wafer surfaces. It indicates that the different numbers of laser pulses affect the modifications of silicon surfaces by laser interference lithography, and illustrates the different topographies of structures produced by three-beam and four-beam laser interference with different laser exposures. The experimentally measured maximum periods of intensity distributions for three-beam and four-beam laser interference pattern are about 7.6 μm and 9.5 μm, respectively.

In previous publications of four-beam laser interference, the phenomena of secondary periodicity or modulation of the interference pattern was found in the case of slight differences between incident angles [94]. The phenomena of modulation can lead to variable sizes of features such as the shape and period of interference structures in the final pattern distribution, and the control of absolutely equal incident angles is very difficult. Comparing with four-beam laser interference, the modulation phenomenon of three-beam laser interference is not evident, which can avoid the formation of uneven interference patterns. Thus, in the case of the same incident angles, the three-beam system can produce the accurate regular interference pattern as designed.

Figure 8.3 shows the measured curves of the two different regular structures. In the experiment, the laser pulses of 10, 30, 100, 300 and 600 were chosen to analyse the AR performance of the two different structures. It is observed that the reflectance of the four-beam interference fabricated pattern is higher than that of the three-beam interference fabricated pattern over the wavelength range from 380nm to 780nm.

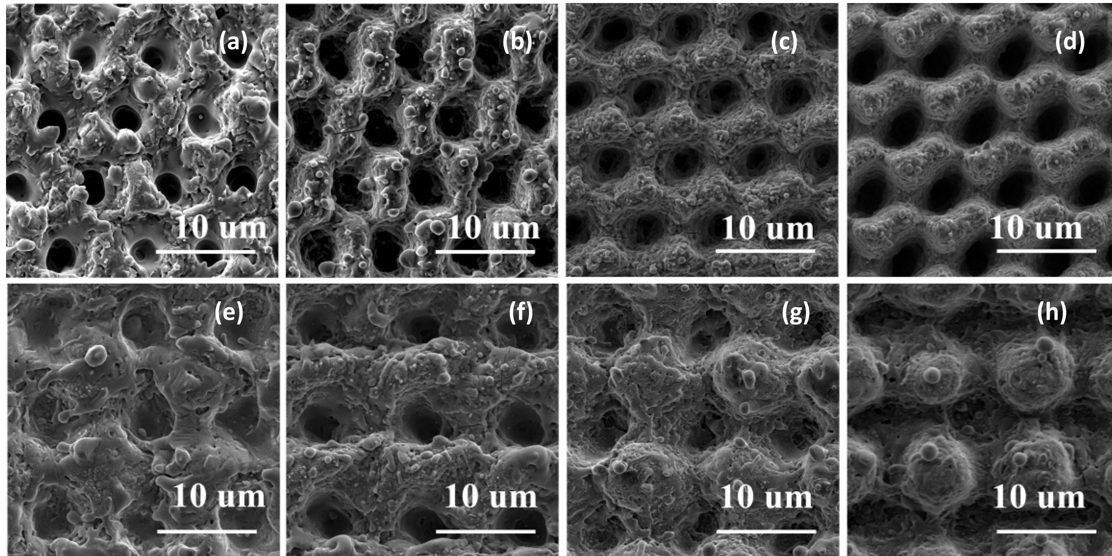

Figure 8.2 (a)-(d) are SEM images of silicon structures fabricated by three-beam laser interference with a laser influence of 637 mJcm^{-2}. (a) laser exposures of 30, (b) laser exposures of 100, (c) laser exposures of 300, and (d) laser exposures of 600. (e)-(h) are SEM images of silicon structures fabricated by four-beam laser interference with a laser influence of 637 mJcm^{-2}. (a) laser exposures of 30, (b) laser exposures of 100, (c) laser exposures of 300, and (d) laser exposures of 600.

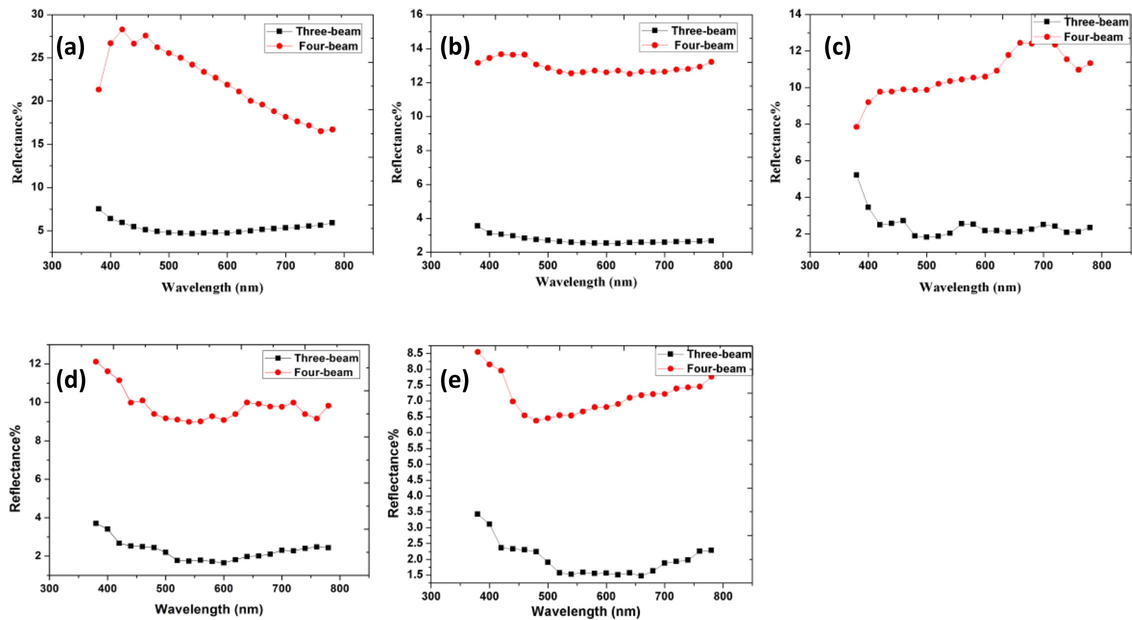

Figure 8.3 Reflectance measurements of structures fabricated by three-beam (black curves) and four-beam (red curves) laser interference with the same laser influence of 637 mJcm^{-2} and the laser exposures of 10 (a), 30 (b), 100 (c), 300 (d) and 600 (e).

The laser interference exposures of 30, 50, 300 and 600 were chosen to study the optimal AR conditions. The morphology and reflectance of the samples in the visible

spectrum were obtained as solar cells mainly absorbed the light in that range, as shown in Figure 8.4. With the number of laser pulses increased, the SWR of the silicon hexagonally-distributed patterns was decreased from 2.6% to 1.8% in the wavelength range from 380 nm to 780 nm and the lowest SWR was obtained by the laser exposures of 600.

Due to that the highest energy distribution of sunlight is at the wavelength of 500 nm to 600 nm, which is the most concentration region of solar irradiation (*AM1.5G*), the main sunlight energy can be better absorbed by the patterns of laser exposures of 300 and 600, which are more suitable for light harvesting [63]. Hence, a proper laser exposure is required to produce desirable antireflection silicon structures that have significantly low SWR by three-beam laser interference process.

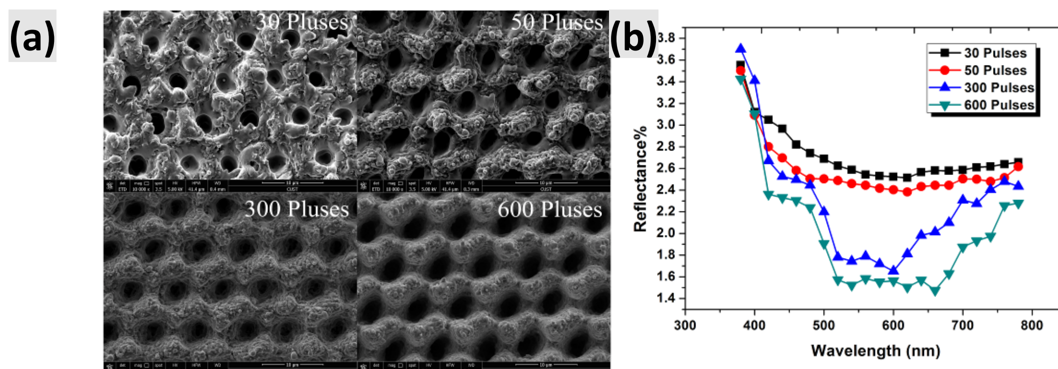

Figure 8.4 The morphology (a) and reflectance (b) of regular hexagonally-distributed patterns fabricated by three-beam laser interference with different laser exposures of 30, 50, 300 and 600.

Meanwhile, the structural depth is also an important parameter for analysing the relationship between the reflectance and the patterns. Figure 8.5 shows the laser exposures and the estimated average heights of the hexagonally-distributed silicon patterns as a function of calculated SWRs. With the accumulation of pulses, the structural depths tend to increase and form the better light-trapping structures. From this point of view, the number of laser exposures is also very important for obtaining a desirable surface morphology. Thus, the hexagonally-distributed pattern and appropriate structural depth can be considered as a potential candidate to produce silicon structures

for solar cell applications with a low SWR value of 1.8 % in the wavelength range of 380 nm to 780 nm.

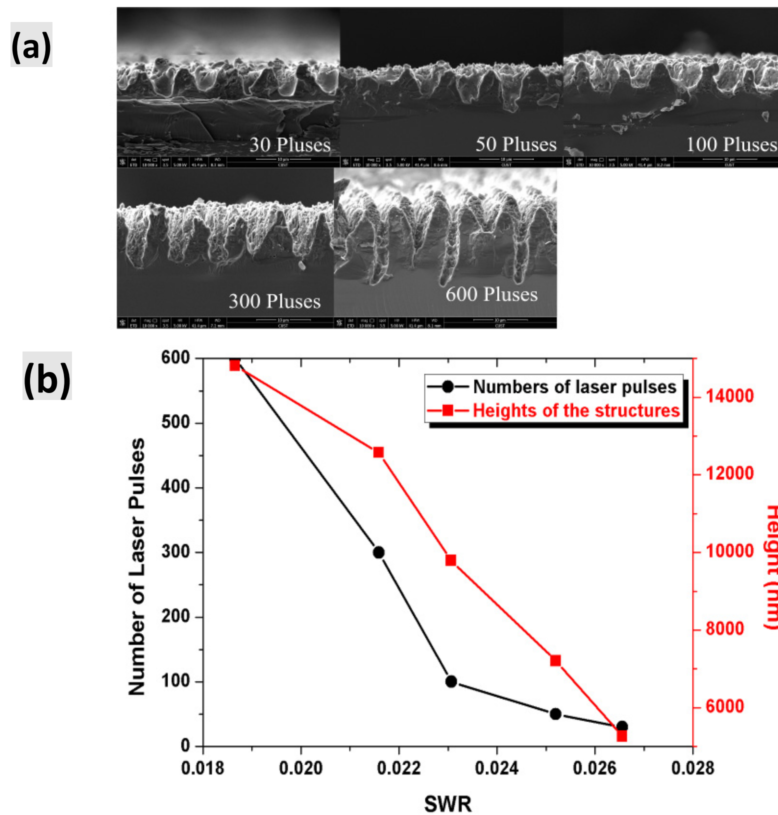

Figure 8.5 (a) is the cross section SEM images of different laser pulses and the scale bar is 10 µm. (b) is the laser pulses and the estimated average heights of the hexagonally-distributed silicon patterns as a function of calculated SWRs.

Figure 8.6 shows the contact angle of hexagonally-distributed silicon patterns as a function of the number of pulses. (a)-(e) are water droplets with a contact angle for hexagonally-distributed patterns fabricated by three-beam laser interference with laser exposures of 30, 50, 100, 300 and 600, respectively. By comparison, the sample of optimum reflectance condition also has good hydrophobic properties. For the micro and nano roughness structures, Cassie-Baxter model is used to explain the sample surface results [53]. It is known that the hydrophobic surface offers a self-cleaning function and leads to remove the accumulated dust particles from the surface of solar cells in atmospheric environments. Thus, the crystalline silicon solar cells with antireflective structures fabricated by the three-beam laser interference process can achieve improved

efficiency and realize the functions of self-cleaning and antireflection.

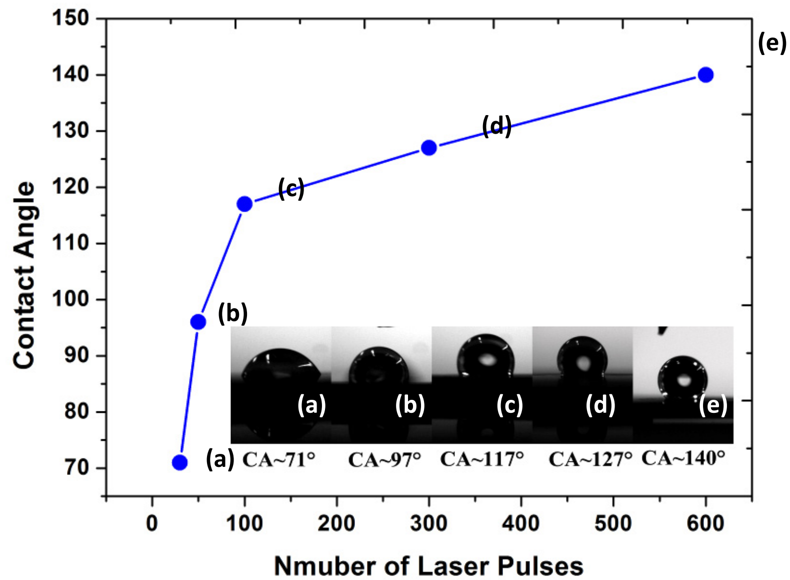

Figure 8.6 The contact angles of hexagonally-distributed silicon patterns as a function of the number of pulses. (a)-(e) are water droplets with a contact angle for hexagonally-distributed patterns fabricated by three-beam laser interference with the laser pulses of 30, 50, 100, 300 and 600, respectively.

8.5 Conclusions

In this work, a three-beam laser interference system was set up to generate periodic micro and nano hole structures with hexagonal distributions. Compared with the existing technologies, the hexagonally-distributed hole structures reveal a design guideline to achieve the low SWR in the wavelength range from 300 nm to 780 nm. The resulting periodic hexagonally-distributed hole structures have shown the low SWR (1.86%) and relatively large contact angle (140°) with a self-cleaning capability.

Chapter 9

Conclusions and Recommendations for Future Work

9.1 Conclusions

Over the last decade, interdisciplinary work has gained momentum as the paradigm for the future of academic research. The work researched in the thesis is of interdisciplinary research representing an intersection between optical science, material science, chemistry and physics. This work has demonstrated that laser interference lithography can fabricate well-defined micro and nano structures that are applied to the surface with the functions of antireflection and self-cleaning properties for solar cells.

Therefore, well-designed micro and nano surface structures fabricated by laser interference lithography can implement both functions of antireflection and self-cleaning, and the novelty of this work is highlighted in the following.

- Silicon surfaces, the main material of fabricated solar cells, can be directly and indirectly modified by laser interference.

  In this research, the sample substrate is monocrystalline silicon because silicon is the main material of solar cells production. The laser interference lithography technology is a faster laser process and the resulting patterns can obtained a function surface with antireflection and self-cleaning properties for solar cells.

- Laser interference patterns are used to create well-defined surface structures. Laser interference lithography can generate various patterns and be applied to direct writing or indirect writing technology on substrate compared to traditional fabrication methods for solar cells surface. In this thesis, Grating, square and hexagon structures and so on are made by multi-beam laser interference, as desired according to different laser parameters. The evolution of interfering

patterns has been achieved and several physical processes such as the formation of holes, dots, ripples the formation of bubbles and the ablation have been discussed.

- ☐ Effects of heat transfer and plasma structure features are obtained from different laser interference parameters.

  This work is to understand that the relationships of laser interference parameters and laser interference pattern and eventually to analyse the relationship between micro and nano structures and antireflection and self-cleaning structures. By controlling the parameters of laser irradiation, different shapes of silicon structures can be obtained. The equations of heat flow and radiation effects of laser plasma of interfering patterns in a four-beam laser interference distribution are proposed to describe their laser radiation impacts on silicon wafer surfaces. With the different laser fluences, several physical processes such as the formation of flower-like holes, dots and cones have been discussed.

- ☐ Fabrication of the laser interference patterns can lead to excellent functions of antireflection and self-cleaning properties.

  The contributions of this thesis are the resulting periodic hexagonally-distributed hole structures with an extremely low SWR (1.86%) and relatively large contact angle (140°) providing a strong self-cleaning capability on the solar cell surface; one step fabrication of the hierarchical silicon structures has a larger contact angle (147°) and relatively low SWR (3.4%) as shown in the chapters 6 and 8.

9.2 Future Work

The work presented in the thesis has attained a number of significant achievements in terms of antireflection and self-cleaning surface of solar cells. In the meantime, there are other issues and potential tasks which can benefit from this work.

- ☐ Further improvement and fabrication of the micro and nano structures to obtain

lower reflection and larger contact angle.

Although the excellent antireflection and self-cleaning surfaces have been obtained, there can be a lower reflection and larger contact angle surface fabricated by laser interference lithography. It is necessary to create structures with photon adsorption property of the incident angle of sunlight range from 0° to 180°. This can further improve the conversion efficiency of solar cells.

- ☐ Optimisation of the contact angle measurement system and reflection measurement system to measure the larger contact angle and reflection of omnidirection incident angles.

In Chapter 6, the triadic hierarchical silicon structures fabricated by three-beam laser interference with 600 pulses cannot measure the contact angle. Because the surface of excellent hydrophobic properties cannot make the water droplets drop down from the tip, its characteristics by the specific contact angles cannot be reacted. Meanwhile, because the side surfaces of the triadic hierarchical silicon structures have the hexagonally-distributed holes, it may have the good function of antireflection properties of omnidirection incident angles. Thus, an effective measurement system of omnidirection incident angles is needed.

- ☐ More specific establishment of the thermal effect relationship between the laser and silicon wafer to analyse the formation of micro and nano structures by thermal effect and plasma.

Thermal and plasma effects are important factors for laser interference interaction with silicon wafer. In this thesis, the relationship equations of the laser interference and silicon wafer are obtained. However, there is no quantitative analysis to solve this special relationship which could be achieved by combining the thermal and plasma and the laser influence of laser interference and analysis of the boundary conditions.

With further research on solar cells, surface structures will be achieved with better functions of antireflection and self-cleaning properties.

References

[1] M. Dresselhaus and I. Thomas, "Alternative energy technologies," *Nature,* vol. 414, pp. 332-337, 2001.

[2] O. Chevaleevski and L. Larina, "New trends in solar photovoltaics: From physics to chemistry," *Korean Journal of Chemical Engineering,* vol. 18, pp. 403-407, 2001.

[3] M. A. Green, K. Emery, Y. Hishikawa, W. Warta, and E. D. Dunlop, "Solar cell efficiency tables (Version 45)," *Progress in photovoltaics: research and applications,* vol. 23, pp. 1-9, 2015.

[4] K. Nakayama, K. Tanabe, and H. A. Atwater, "Plasmonic nanoparticle enhanced light absorption in GaAs solar cells," *Applied Physics Letters,* vol. 93, p. 121904, 2008.

[5] M. Tao, W. Zhou, H. Yang, and L. Chen, "Surface texturing by solution deposition for omnidirectional antireflection," *Applied Physics Letters,* vol. 91, p. 081118, 2007.

[6] V. Zorba, E. Stratakis, M. Barberoglou, E. Spanakis, P. Tzanetakis, S. H. Anastasiadis, and C. Fotakis, "Biomimetic Artificial Surfaces Quantitatively Reproduce the Water Repellency of a Lotus Leaf," *Advanced Materials,* vol. 20, pp. 4049-4054, 2008.

[7] D. M. Chapin, C. Fuller, and G. Pearson, "A new silicon p ‐ n junction photocell for converting solar radiation into electrical power," *Journal of Applied Physics,* pp. 676-677, 1954.

[8] L. M. Fraas and L. D. Partain, *Solar cells and their applications* vol. 236: John Wiley & Sons, 2010.

[9] Available: http://www.bls.gov/green/solar_power/

[10] W. Sparber, O. Schultz, D. Biro, G. Emanuel, R. Preu, A. Poddey, and D. Borchert, "Comparison of texturing methods for monocrystalline silicon solar cells using KOH and Na_2/CO_3," in *Photovoltaic Energy Conversion, 2003. Proceedings of 3rd World Conference on*, 2003, pp. 1372-1375.

[11] V. V. Iyengar, B. K. Nayak, and M. C. Gupta, "Optical properties of silicon light trapping structures for photovoltaics," *Solar Energy Materials and Solar Cells,* vol. 94, pp. 2251-2257, 2010.

[12] C.-L. Lee, K. Tsujino, Y. Kanda, S. Ikeda, and M. Matsumura, "Pore formation in silicon by wet etching using micrometre-sized metal particles as catalysts," *Journal of Materials Chemistry,* vol. 18, pp. 1015-1020, 2008.

[13] K. Tsujino and M. Matsumura, "Morphology of nanoholes formed in silicon by wet etching in solutions containing HF and H 2 O 2 at different concentrations using silver nanoparticles as catalysts," *Electrochimica Acta,* vol. 53, pp. 28-34, 2007.

[14] S. K. Srivastava, D. Kumar, P. Singh, M. Kar, V. Kumar, and M. Husain, "Excellent antireflection properties of vertical silicon nanowire arrays," *Solar Energy Materials and Solar Cells,* vol. 94, pp. 1506-1511, 2010.

[15] D. Qi, N. Lu, H. Xu, B. Yang, C. Huang, M. Xu, L. Gao, Z. Wang, and L. Chi, "Simple approach to wafer-scale self-cleaning antireflective silicon surfaces," *Langmuir,* vol. 25, pp. 7769-7772, 2009.

[16] M. Green, "Silicon solar cells: Advanced principles and practice. 1995," *Sydney, NSW: Bridge printery*.

[17] P. Papet, O. Nichiporuk, A. Kaminski, Y. Rozier, J. Kraiem, J. F. Lelievre, A. Chaumartin, A. Fave, and M. Lemiti, "Pyramidal texturing of silicon solar cell with TMAH chemical anisotropic etching," *Solar Energy Materials and Solar Cells,* vol. 90, pp. 2319-2328, 2006.

[18] L. A. Dobrzanski, A. Drygala, K. Golombek, P. Panek, E. Bielanska, and P. Zieba, "Laser surface treatment of multicrystalline silicon for enhancing optical properties," *Journal of Materials Processing Technology,* vol. 201, pp. 291-296, 2008.

[19] J. Chen and K. Sun, "Enhancement of the light conversion efficiency of silicon solar cells by using nanoimprint anti-reflection layer," *Solar Energy Materials and Solar Cells,* vol. 94, pp. 629-633, 2010.

[20] C. L. Cheung, R. Nikolić, C. Reinhardt, and T. Wang, "Fabrication of nanopillars by nanosphere lithography," *Nanotechnology,* vol. 17, p. 1339, 2006.

[21] D. Zhang, W. Ren, Z. Zhu, H. Zhang, B. Liu, W. Shi, X. Qin, and C. Cheng, "Highly-ordered silicon inverted nanocone arrays with broadband light antireflectance," *Nanoscale research letters,* vol. 10, pp. 1-6, 2015.

[22] M.-J. Sher, M. T. Winkler, and E. Mazur, "Pulsed-laser hyperdoping and surface texturing for photovoltaics," *MRS bulletin,* vol. 36, pp. 439-445, 2011.

[23] M. J. Sher, M. T. Winkler, and E. Mazur, "Pulsed-laser hyperdoping and surface texturing for photovoltaics," *MRS bulletin,* vol. 36, pp. 439-445, 2011.

[24] B. R. Tull, J. E. Carey, E. Mazur, J. P. McDonald, and S. M. Yalisove, "Silicon surface morphologies after femtosecond laser irradiation," *MRS bulletin,* vol. 31, pp. 626-633, 2006.

[25] A. Rodriguez, M. Echeverría, M. Ellman, N. Perez, Y. K. Verevkin, C. S. Peng, T. Berthou, Z. Wang, I. Ayerdi, and J. Savall, "Laser interference lithography for nanoscale structuring of materials: From laboratory to industry," *Microelectronic Engineering,* vol. 86, pp. 937-940, 2009.

[26] Z. Wang, J. Zhang, Z. Ji, M. Packianather, C. S. Peng, C. Tan, Y. K. Verevkin, S. M. Olaizola, T. Berthou, and S. Tisserand, "Laser interference nanolithography," in *Proceedings of the 3rd International Conference on Manufacturing Engineering*, 2008, pp. 929-936.

[27] V. V. Iyengar, B. K. Nayak, and M. C. Gupta, "Optical properties of silicon light trapping structures for photovoltaics," *Solar Energy Materials and Solar Cells,* vol. 94, pp. 2251-2257.

[28] A. Rodriguez, M. Ellman, I. Ayerdi, N. Perez, S. Olaizola, J. Zhang, Z. Ji, T. Berthou, C. Peng, and Y. Verevkin, "Interference lithography processes with high-power laser pulses," in *SPIE LASE: Lasers and Applications in Science and Engineering*, 2009, pp. 72010R-72010R-8.

[29] D. Richard and D. Quéré, "Viscous drops rolling on a tilted non-wettable solid," *EPL (Europhysics Letters),* vol. 48, p. 286, 1999.

[30] D. Richard and D. Quéré, "Bouncing water drops," *EPL (Europhysics Letters),* vol. 50, p. 769, 2000.

[31] H. Y. Erbil, A. L. Demirel, Y. Avc, and O. Mert, "Transformation of a simple plastic into a superhydrophobic surface," *Science,* vol. 299, p. 1377, 2003.

[32] H. Yabu, M. Takebayashi, M. Tanaka, and M. Shimomura, "Superhydrophobic and lipophobic properties of self-organized honeycomb and pincushion structures," *Langmuir,* vol. 21, pp. 3235-3237, 2005.

[33] X. Wu, L. Zheng, and D. Wu, "Fabrication of superhydrophobic surfaces from microstructured ZnO-based surfaces via a wet-chemical route," *Langmuir,* vol. 21, pp. 2665-2667, 2005.

[34] E. Hosono, S. Fujihara, I. Honma, and H. Zhou, "Superhydrophobic perpendicular nanopin film by the bottom-up process," *Journal of the American Chemical Society,* vol. 127, pp. 13458-13459, 2005.

[35] H. Liu, L. Feng, J. Zhai, L. Jiang, and D. Zhu, "Reversible wettability of a chemical vapor deposition prepared ZnO film between superhydrophobicity and superhydrophilicity," *Langmuir,* vol. 20, pp. 5659-5661, 2004.

[36] C. H. Wang, Y. Y. Song, J. W. Zhao, and X. H. Xia, "Semiconductor supported biomimetic superhydrophobic gold surfaces by the galvanic exchange reaction," *Surface science,* vol. 600, pp. 38-42, 2006.

[37] E. Martines, K. Seunarine, H. Morgan, N. Gadegaard, C. D. W. Wilkinson, and M. O. Riehle, "Superhydrophobicity and superhydrophilicity of regular nanopatterns," *Nano letters,* vol. 5, pp. 2097-2103, 2005.

[38] D. Öner and T. J. McCarthy, "Ultrahydrophobic surfaces. Effects of topography length scales on

wettability," *Langmuir,* vol. 16, pp. 7777-7782, 2000.

[39] D. H. Macdonald, A. Cuevas, M. J. Kerr, C. Samundsett, D. Ruby, S. Winderbaum, and A. Leo, "Texturing industrial multicrystalline silicon solar cells," *Solar Energy,* vol. 76, pp. 277-283, 2004.

[40] A. Vorobyev and C. Guo, "Direct creation of black silicon using femtosecond laser pulses," *Applied surface science,* vol. 257, pp. 7291-7294, 2011.

[41] Z. Zhang, Z. Wang, D. Wang, and Y. Ding, "Periodic antireflection surface structure fabricated on silicon by four-beam laser interference lithography," *Journal of Laser Applications,* vol. 26, p. 012010, 2014.

[42] D. Wang, Z. Wang, Z. Zhang, Y. Yue, D. Li, R. Qiu, and C. Maple, "Both antireflection and superhydrophobicity structures achieved by direct laser interference nanomanufacturing," *Journal of Applied Physics,* vol. 115, p. 233101, 2014.

[43] Z. Jin, F. Boru, and G. Yongkang, "Laser interference photolithography for fabricating periodic patterns in large area," *Opto-Electronic Engineering,* vol. 28, pp. 20-23, 2001.

[44] Q. Xie, M. Hong, H. Tan, G. Chen, L. Shi, and T. Chong, "Fabrication of nanostructures with laser interference lithography," *Journal of alloys and compounds,* vol. 449, pp. 261-264, 2008.

[45] K.-Q. Peng, X. Wang, L. Li, X.-L. Wu, and S.-T. Lee, "High-performance silicon nanohole solar cells," *Journal of the American Chemical Society,* vol. 132, pp. 6872-6873, 2010.

[46] S. Jeong, E. C. Garnett, S. Wang, Z. Yu, S. Fan, M. L. Brongersma, M. D. McGehee, and Y. Cui, "Hybrid silicon nanocone–polymer solar cells," *Nano letters,* vol. 12, pp. 2971-2976, 2012.

[47] H. Wolferen and L. Abelmann, "Laser interference lithography," in *Lithography: Principles, Processes and Materials*, Theodore C. Hennessy (Ed.), 2011, pp. 133-148.

[48] R. Le Harzic, H. Schuck, D. Sauer, T. Anhut, I. Riemann, and K. König, "Sub-100 nm nanostructuring of silicon by ultrashort laser pulses," *Optics Express,* vol. 13, pp. 6651-6656, 2005.

[49] Z. Wang, J. Zhang, Z. Ji, M. Packianather, C. Peng, C. Tan, Y. Verevkin, S. Olaizola, T. Berthou, and S. Tisserand, "Laser interference nanolithography," 2008, pp. 929-936.

[50] L. Wang, Z.-H. Lü, X.-F. Lin, Q.-D. Chen, B.-B. Xu, and H.-B. Sun, "Rapid fabrication of large-area periodic structures by multiple exposure of two-beam interference," *Lightwave Technology, Journal of,* vol. 31, pp. 276-281, 2013.

[51] X. Meng, G. Gomard, O. El Daif, E. Drouard, R. Orobtchouk, A. Kaminski, A. Fave, M. Lemiti, A. Abramov, and P. Roca i Cabarrocas, "Absorbing photonic crystals for silicon thin-film solar cells: Design, fabrication and experimental investigation," *Solar Energy Materials and Solar Cells,* vol. 95, pp. S32-S38, 2011.

[52] L. Dobrzański, A. Drygała, K. Gołombek, P. Panek, E. Bielańska, and P. Zięba, "Laser surface treatment of multicrystalline silicon for enhancing optical properties," *Journal of Materials Processing Technology,* vol. 201, pp. 291-296, 2008.

[53] S. Nolte, C. Momma, H. Jacobs, A. Tünnermann, B. Chichkov, B. Wellegehausen, and H. Welling, "Ablation of metals by ultrashort laser pulses," *JOSA B,* vol. 14, pp. 2716-2722, 1997.

[54] B. Bhushan, Y. C. Jung, and K. Koch, "Micro-, nano-and hierarchical structures for superhydrophobicity, self-cleaning and low adhesion," *Philosophical Transactions of the Royal Society A: Mathematical, Physical and Engineering Sciences,* vol. 367, pp. 1631-1672, 2009.

[55] L. Zhao, Z. Wang, Z. Zhang, Z. Weng, C. Maple, and Y. Yue, "Silicon wafer modification by laser interference," in *Nano/Micro Engineered and Molecular Systems (NEMS), 2013 8th IEEE International Conference on*, 2013, pp. 1236-1239.

[56] L. Zhao, Z. Wang, J. Zhang, L. Cao, L. Li, Y. Yue, and D. Li, "Antireflection silicon structures with

hydrophobic property fabricated by three-beam laser interference," *Applied surface science,* vol. 346, pp. 574-579, 2015.

[57] D. Wang, Z. Wang, Z. Zhang, Y. Yue, D. Li, and C. Maple, "Effects of polarization on four-beam laser interference lithography," *Applied Physics Letters,* vol. 102, p. 081903, 2013.

[58] L. Zhao, Z. Wang, J. Zhang, M. Yu, S. Li, D. Li, and Y. Yue, "Effects of laser fluence on silicon modification by four-beam laser interference," *Journal of Applied Physics,* vol. 118, p. 233106, 2015.

[59] L. Zhao, Z. Wang, W. Li, M. Yu, Z. Zhang, J. Xu, Y. Yu, Z. Weng, S. Li, and C. Maple, "Effect of pulse repetition rate on silicon wafer modification by four-beam laser interference," in *Manipulation, Manufacturing and Measurement on the Nanoscale (3M-NANO), 2013 International Conference on*, 2013, pp. 104-107.

[60] B. K. Nayak, M. C. Gupta, and K. W. Kolasinski, "Ultrafast-laser-assisted chemical restructuring of silicon and germanium surfaces," *Applied surface science,* vol. 253, pp. 6580-6583, 2007.

[61] M. Abbott and J. Cotter, "Optical and electrical properties of laser texturing for high‐efficiency solar cells," *Progress in Photovoltaics: Research and Applications,* vol. 14, pp. 225-235, 2006.

[62] Y. Ma, H. Shi, J. Si, T. Chen, F. Yan, F. Chen, and X. Hou, "Photoinduced microchannels and element change inside silicon by femtosecond laser pulses," *Optics Communications,* vol. 285, pp. 140-142, 2012.

[63] J. Bonse, S. Baudach, J. Krüger, W. Kautek, and M. Lenzner, "Femtosecond laser ablation of silicon–modification thresholds and morphology," *Applied Physics A,* vol. 74, pp. 19-25, 2002.

[64] J. Reif, O. Varlamova, M. Bounhalli, M. Muth, and T. Arguirov, "Nanostructure formation upon femtosecond ablation from silicon: Effect of double pulses," *Applied surface science,* vol. 258, pp. 9491-9495, 2012.

[65] X. Wang, Z. Shen, J. Lu, and X. Ni, "Laser-induced damage threshold of silicon in millisecond, nanosecond, and picosecond regimes," *Journal of Applied Physics,* vol. 108, pp. 033103-033103-7, 2010.

[66] B. Chichkov, C. Momma, S. Nolte, F. Von Alvensleben, and A. Tünnermann, "Femtosecond, picosecond and nanosecond laser ablation of solids," *Applied Physics A,* vol. 63, pp. 109-115, 1996.

[67] W. Zhao, J. Li, H. K. Kang, B. Zhou, and C. Wong, "Direct Laser Interference Writing of Silver Gratings," *Nanoscience and Nanotechnology Letters,* vol. 3, pp. 246-249, 2011.

[68] T. Tavera, N. Pérez, A. Rodríguez, P. Yurrita, S. Olaizola, and E. Castano, "Periodic patterning of silicon by direct nanosecond laser interference ablation," *Applied surface science,* vol. 258, pp. 1175-1180, 2011.

[69] L. Dobrzański and A. Drygała, "Laser processing of multicrystalline silicon for texturization of solar cells," *Journal of Materials Processing Technology,* vol. 191, pp. 228-231, 2007.

[70] T. C. Chong, M. H. Hong, and L. P. Shi, "Laser precision engineering: from microfabrication to nanoprocessing," *Laser & Photonics Reviews,* vol. 4, pp. 123-143, 2010.

[71] J. Han, W. Fan, Y. Li, L. Yang, G. Feng, X. Gao, Y. Liu, L. Bao, and Y. Huang, "Laser plasma effects on surface damage characteristics of silicon," in *Pacific Rim Laser Damage Symposium: Optical Materials for High Power Lasers*, 2011, pp. 820616-820616-7.

[72] J. Kaspar, A. Luft, S. Nolte, M. Will, and E. Beyer, "Laser helical drilling of silicon wafers with ns to fs pulses: Scanning electron microscopy and transmission electron microscopy characterization of drilled through-holes," *Journal of Laser Applications,* vol. 18, p. 85, 2006.

[73] J. Bonse, S. Baudach, J. Krüger, W. Kautek, and M. Lenzner, "Femtosecond laser ablation of silicon-modification thresholds and morphology," *Applied Physics A: Materials Science & Processing,*

vol. 74, pp. 19-25, 2002.

[74] M. Trtica, B. Gakovic, B. Radak, D. Batani, T. Desai, and M. Bussoli, "Periodic surface structures on crystalline silicon created by 532nm picosecond Nd: YAG laser pulses," *Applied surface science,* vol. 254, pp. 1377-1381, 2007.

[75] A. Hertwig, S. Martin, J. Krüger, and W. Kautek, "Interaction area dependence of the ablation threshold of ion-doped glass," *Thin Solid Films,* vol. 453, pp. 527-530, 2004.

[76] X. Chen, B. Bian, Z. Shen, J. Lu, and X. Ni, "Equations of laser - induced plasma shock wave motion in air," *Microwave and Optical Technology Letters,* vol. 38, pp. 75-79, 2003.

[77] J. Shao, "Pacific Rim Laser Damage 2011: Optical Materials for High Power Lasers," in *Society of Photo-Optical Instrumentation Engineers (SPIE) Conference Series*, 2011.

[78] Y. Lee, S. H. Park, K. B. Kim, and J. K. Lee, "Fabrication of hierarchical structures on a polymer surface to mimic natural superhydrophobic surfaces," *Advanced materials,* vol. 19, pp. 2330-2335, 2007.

[79] Z.-H. Yang, F.-C. Chien, C.-W. Kuo, D.-Y. Chueh, and P. Chen, "Hybrid contact and interfacial adhesion on well-defined periodic hierarchical pillars," *Nanoscale,* vol. 5, pp. 1018-1025, 2013.

[80] D. Wu, S.-z. Wu, Q.-D. Chen, S. Zhao, H. Zhang, J. Jiao, J. A. Piersol, J.-N. Wang, H.-B. Sun, and L. Jiang, "Facile creation of hierarchical PDMS microstructures with extreme underwater superoleophobicity for anti-oil application in microfluidic channels," *Lab on a Chip,* vol. 11, pp. 3873-3879, 2011.

[81] B. K. Nayak and M. C. Gupta, "Ultrafast laser-induced self-organized conical micro/nano surface structures and their origin," *Optics and Lasers in Engineering,* vol. 48, pp. 966-973, 2010.

[82] T.-H. Her, R. J. Finlay, C. Wu, S. Deliwala, and E. Mazur, "Microstructuring of silicon with femtosecond laser pulses," *Applied Physics Letters,* vol. 73, pp. 1673-1675, 1998.

[83] F. Sanchez, J. Morenza, R. Aguiar, J. Delgado, and M. Varela, "Whiskerlike structure growth on silicon exposed to ArF excimer laser irradiation," *Applied Physics Letters,* vol. 69, pp. 620-622, 1996.

[84] F. Sanchez, J. Morenza, R. Aguiar, J. Delgado, and M. Varela, "Dynamics of the hydrodynamical growth of columns on silicon exposed to ArF excimer-laser irradiation," *Applied Physics A: Materials Science & Processing,* vol. 66, pp. 83-86, 1998.

[85] T.-H. Her, R. J. Finlay, C. Wu, S. Deliwala, and E. Mazur, "Microstructuring of silicon with femtosecond laser pulses," *Applied Physics Letters,* vol. 73, p. 1673, 1998.

[86] A. E. Siegman and P. M. Fauchet, "Stimulated Wood's anomalies on laser-illuminated surfaces," *Quantum Electronics, IEEE Journal of,* vol. 22, pp. 1384-1403, 1986.

[87] Z. Guosheng, P. Fauchet, and A. Siegman, "Growth of spontaneous periodic surface structures on solids during laser illumination," *Physical Review B,* vol. 26, p. 5366, 1982.

[88] M. Huang, F. Zhao, Y. Cheng, N. Xu, and Z. Xu, "Origin of laser-induced near-subwavelength ripples: interference between surface plasmons and incident laser," *Acs Nano,* vol. 3, pp. 4062-4070, 2009.

[89] H. Sai, Y. Kanamori, K. Arafune, Y. Ohshita, and M. Yamaguchi, "Light trapping effect of submicron surface textures in crystalline Si solar cells," *Progress in Photovoltaics: Research and Applications,* vol. 15, pp. 415-423, 2007.

[90] M. Nosonovsky and B. Bhushan, "Biologically Inspired Surfaces: Broadening the Scope of Roughness**," *Advanced Functional Materials,* vol. 18, pp. 843-855, 2008.

[91] W. Sparber, O. Schultz, D. Biro, G. Emanuel, R. Preu, A. Poddey, and D. Borchert, "Comparison of texturing methods for monocrystalline silicon solar cells using KOH and Na_2CO_3," pp. 1372-1375 Vol. 2.

[92] S. Sivasubramaniam and M. M. Alkaisi, "Inverted nanopyramid texturing for silicon solar cells using interference lithography," *Microelectronic Engineering,* vol. 119, pp. 146-150, 2014.

[93] W. Li, Z. Wang, D. Wang, Z. Zhang, L. Zhao, D. Li, R. Qiu, and C. Maple, "Superhydrophobic dual micro-and nanostructures fabricated by direct laser interference lithography," *Optical Engineering,* vol. 53, pp. 034109-034109, 2014.

[94] D. Wang, Z. Wang, Z. Zhang, Y. Yue, D. Li, and C. Maple, "Effects of polarization on four-beam laser interference lithography," *Applied physics letters,* vol. 102, Feb 25 2013.

Appendix A

Publications Originated from This Work

[1] **L. Zhao**, Z. Wang, J. Zhang, L. Cao, L. Li, Y. Yue, and D. Li, Antireflection silicon structures with hydrophobic property fabricated by three-beam laser interference, Applied Surface Science, Vol.346, pp.574-579, 2015. (Sci, IF: 2.9)

[2] **L. Zhao**, Z. Wang, D. Wang, Z. Zhang, Y. Yu, Z. Weng, C. Maple, D. Li, and Y. Yue, Silicon wafer modification by laser interference, IEEE NEMS 2013. (EI indexed)

[3] **L. Zhao**, C. Maple, Z. Wang, W. Li, M. Yu, Z. Zhang, J. Xu, Y. Yu, Z. Weng, D. Li, Y. Yue, and S. Li, Effect of pulse repetition rate on silicon wafer modification by four-beam laser interference, IEEE 3M-NANO 2013. (EI indexed)

[4] J. Zhang, Z. Wang, X. Di, **L. Zhao**, and D. Wang, Effects of azimuthal angles on laser interference lithography, Applied Optics, Vol.53, pp.6294-6301, 2014. (Sci, IF: 1.6)

[5] L. Li, Z. Wang, W. Li, K. Peng, Z. Zhang, M. Yu, Z. Song, Z. Weng, D. Wang, and **L. Zhao,** Fabrication of PT nanowires with diffraction-unlimited feature size by high threshold lithography, Applied Physics Letters, Accepted. (SCI, IF: 3.5)

[6] J. Xu, Z. Wang, Z. Weng, Z. Li, X. Sun, L. Liu, **L. Zhao**, Y. Yue, and J. Zhang, Laser interference nanolithography with a 405nm fiber semiconductor laser, Key Engineering Materials, Vol.552, pp.262-267, 2012.

[7] M. Yu, C. Tan, Z. Wang, **L. Zhao**, and W. Li, Effect of parameters on three-beam laser interference, IEEE 3M-NANO 2013. (EI indexed)

[8] **L. Zhao,** Z. Wang, J. Zhang, M. Yu, S. Li, D. Li, and Y. Yue, Effects of laser fluence on silicon modification by Four-beam Laser Interference, Journal of Applied Physics, Vol.118, pp.233106, 2015. (Sci, IF: 2.4)

[9] **L. Zhao**, Z. Wang, L. Li, L. Sao, J. Zhang, M. Yu, Y. Yue and D. Li, One step fabrication of triadic hierarchical silicon architectures with excellent antireflection and self-cleaning properties, Applied Physics Letters, in process. (SCI, IF: 3.5)

[10] W. Li, Z. Wang, D. Wang, Z. Zhang, **L. Zhao**, D. Li, R. Qiu, C. Maple, Superhydrophobic micro and nano dual structures fabricated by direct laser interference lithography Opt. Eng. Vol.53, 034109, 2014. (Sci, IF: 0.9)

Appendix B

The Data of Figure 5.25

Wavelength (nm)	Moncrystalline Silicon Solar Cell Surface Reflectance (%)	Polished Silicon Surface Reflectance (%)	Four-beam Interference Pattern Silicon Surface Reflectance (%)
380	30.81914	49.28569	12.11192
400	32.12541	50.56798	11.60793
420	29.40438	50.91197	11.14359
440	25.58128	50.2539	9.98091
460	20.57045	48.491	10.09218
480	16.29446	45.41061	9.38989
500	12.75838	43.79392	9.16538
520	10.01649	43.17151	9.0961
540	7.31783	42.42367	7.58759
560	5.53802	41.81303	6.00689
580	4.40865	41.53688	5.27358
600	3.66848	41.20256	4.07692
620	3.08813	41.17547	4.08208
640	3.01534	40.82928	3.98885
660	2.87699	40.90122	3.9161
680	3.21246	40.85931	4.07468
700	3.40873	40.05736	3.76703
720	3.75139	40.55059	3.98113
740	4.78365	44.60086	4.38255
760	6.15148	49.4324	4.15448
780	8.09842	52.41022	2.81786

The Data of Figure 5.25

Wavelength (nm)	30 Pulses Reflectance (%)	50 Pulses Reflectance (%)	200 Pulses Reflectance (%)	300 Pulses Reflectance (%)	600 Pulses Reflectance (%)
380	10.90573	5.09987	4.38279	4.30353	3.29339
400	11.08373	5.39989	3.8654	3.81552	3.29984
420	10.51297	5.58972	3.97894	3.96609	3.23264
440	10.61213	5.82257	3.99637	3.96665	3.30483
460	9.34692	5.31098	3.76966	3.76513	3.27663
480	9.0851	5.49704	3.94776	3.8832	3.38954
500	9.31455	5.57615	4.1402	3.49271	3.27318
520	9.00563	5.38637	4.11419	3.50078	3.24756
540	8.85005	5.36746	4.17555	3.50931	3.24377
560	8.76101	5.37253	4.26207	3.517	3.25402
580	8.72155	5.35915	4.34144	3.5371	3.2552
600	8.95036	5.42843	4.41315	3.65494	3.3999
620	8.87173	5.40725	4.46458	3.66056	3.40275
640	9.09046	5.56904	4.56825	3.79358	3.54436
660	9.10964	5.60796	4.67474	3.85632	3.58748
680	8.93986	5.58819	4.66771	3.82716	3.57343
700	9.11326	5.66329	4.92426	3.90222	3.75432
720	9.24885	5.72133	4.94191	3.97667	3.85216
740	8.71117	5.58744	4.80007	3.96123	3.75184
760	8.79561	5.68831	4.95104	4.04448	3.85334
780	9.12315	6.15532	5.52923	4.32296	4.13808

The Data of Figure 8.4 (b)

Wavelength (nm)	30 Pulses Reflectance (%)	50 Pulses Reflectance (%)	300 Pulses Reflectance (%)	600 Pulses Reflectance (%)
380	3.55346	3.50274	3.70016	3.42419
400	3.11905	3.09115	3.40967	3.10397
420	3.04785	2.8003	2.67132	2.36144
440	2.96593	2.69683	2.52599	2.33054
460	2.82024	2.58146	2.49709	2.30278
480	2.74107	2.50593	2.44529	2.23816
500	2.68872	2.50446	2.19751	1.90659
520	2.62479	2.48931	1.7799	1.57209
540	2.58646	2.46022	1.7433	1.52263
560	2.54297	2.44434	1.78911	1.58416
580	2.5312	2.41703	1.71846	1.55284
600	2.52322	2.40326	1.65259	1.563
620	2.51348	2.38284	1.81066	1.50475
640	2.56625	2.43285	1.98261	1.5696
660	2.5807	2.44526	2.01229	1.47541
680	2.5792	2.4447	2.09961	1.62968
700	2.58586	2.50432	2.30667	1.87468
720	2.61021	2.50136	2.27491	1.93204
740	2.61761	2.47986	2.4031	1.97433
760	2.63936	2.51429	2.47937	2.25682
780	2.6572	2.61706	2.43483	2.27947

Appendix C

Matlab Scripts

```
% Matlab simulation of the heat flow expression of the four-beam laser interference distribution
function T=ex20_1(z,t)
m=0;
z=linspace(0,1,20); %xmesh
t=linspace(0,2,20); %tspan
%************
%************
sol=pdepe(m,@ex20_1pdefun,@ex20_1ic,@ex20_1bc,z,t);
T=sol(:,:,1);
%************
%************
%figure;
%surf(z,t,T);
% title('pde Numerical solution ')
% xlabel(' Depth z')
% ylabel('Time t')
% zlabel('Numerical solution of temperature T')
%*************
%
%*************
% figure(2)
% surf(z,t,exp(-t)'*sin(pi*z));
% title(' Analytical solution ')
% xlabel(' Depth z')
% ylabel('Time t' )
% zlabel('Numerical solution u')
%*****************
%t=tf=2
%*****************
% figure;
% M=length(t);
% zout=linspace(0,1,100);
% [Tout,dudz] =pdeval(m,z,T(M,:),zout);
% plot(zout,Tout);
% title('when time is 2, the solution has been shown as following')
% xlabel('Depth z')
% ylabel('Temputer T')
%******************
%pde
%******************
```

```
function [c,f,s]=ex20_1pdefun(z,t,u,dudz)
global I0;
% I=1;
rho=2.33;
cLittle=0.72;
k=0.23;
% I0=1;
% R=0.33;
% a=50;
% fr=1;
% gt=1;
c=cLittle*rho;
f=k*dudz;
% s=I0*(1-R)*a*fr*gt*exp(-1*a*z);
taoL=8e-9;
R=0.33;
A=1-R;
a=50;
% It=I*exp(t/taoL);
It=1;
% s=It*A*a*exp(-1*a*z);
s=I0*exp(-1*a*z);
%******************

%******************
function u0=ex20_1ic(z)
T0=300;
u0=T0;
% u0=sin(pi*z);
%******************
%******************
function [pl,ql,pr,qr]=ex20_1bc(zl,ul,zr,ur,t)
lanbdaz=299/(300-99);
Tz0=300;
T0=300;
Tzc=310;
h=1.38;
pl=h*(T0-Tz0);
ql=lanbdaz;
pr=h*(T0-Tzc);
qr=-1*lanbdaz;

% pl=0;
% ql=1;
```

```
% pr=0;
% qr=1;

% pl=ul;
% ql=0;
% pr=pi*exp(-t);
% qr=1;
```